Large Scale Single Layer Hexagonal Boron Nitride Growth, Process Control and Application

Dissertation

zur

Erlangung der naturwissenschaftlichen Doktorwürde
(Dr. sc. nat.)

vorgelegt der

Mathematisch-naturwissenschaftlichen Fakultät

der

Universität Zürich

von

Adrian Hemmi
von Churwalden (GR)

Promotionskomitee

Prof. Dr. Thomas Greber (Vorsitz und Leitung der Dissertation)
Prof. Dr. Jürg Osterwalder
Prof. Dr. Frank Nuesch

Zürich 2014

Die vorliegende Arbeit wurde von der Mathematisch-Naturwissenschaftlichen Fakultät der Universität Zürich im .....semester .... als Dissertation angenommen.

Promotionskomitee: Prof. Dr. Thomas Greber (Vorsitzender und Leiter der Dissertation),
Prof. Dr. Jürg Osterwalder und
Prof. Dr. Frank Nüesch (Gutachter)

Abstract

In this work, facilities and instrumentation were developed and set up in order to establish the large scale production of ultra high vacuum (UHV) processed surfaces. These surfaces are intended to be used as basis for the fabrication of atomically-defined devices. The device oriented application requires an efficient large scale synthesis of the desired surface. Here, the chemical vapor deposition (CVD) of the atomic single layer hexagonal boron nitride (h-BN) on rhodium(111) has been upscaled to four-inch wafer substrates. Such four-inch wafers are meant to close the gap between the surface science knowledge of producing atomically well-defined surfaces and their implementation in macroscopic devices.

The main part of this thesis consists of the setup and commissioning of a UHV system, which is capable of handling and processing four-inch wafer substrates. This task corresponds to an adaptation of known procedures and processes to large area samples. In order to facilitate this process adaptation, several approaches of monitoring the atomic single layer growth during a CVD process have been investigated. Among these, the reaction gas analysis in combination with in-situ photoelectron yield measurements are shown to provide detailed information about the status of a surface reaction.

The thesis is complemented with investigations of further processing steps of the produced h-BN/Rh(111) samples. The first approach is the growth of macroscopically thick boron nitride layers, which may directly provide a substrate for, e.g., graphene based electronic devices. The second approach involves the separation and transfer of the single h-BN layer from its metal substrate. Such a transferred h-BN single layer could be used as protection layer against water or oxidation or might be implemented as thin isolation layer in an electronic device.

This thesis focuses on the adjustment and setup of new instrumentation and installations and is meant to provide a manual for a future experimentalists. Hence, it includes extended technical details.

Zusammenfassung

In der vorliegenden Doktorarbeit sind Anlagen und Geräte entwickelt und installiert worden, um die grossflächige Herstellung von Ultrahochvakuum (UHV) prozessierten Oberflächen zu ermöglichen. Diese Oberflächen sollen als Basis für die Anfertigung von Funktionseinheiten auf atomarer Stufe dienen. Eine solche Anwendungsorientierung benötigt die Herstellung der gewünschten Oberfläche in grossem Umfang. Hier wurde die chemische Gasphasenabscheidung ("chemical vapor deposition", CVD) von atomar einlagigem hexagonalem Bornitride (h-BN) auf Rhodium(111) auf vier Inch Wafersubstrate übertragen. Diese vier Inch Wafer sollen helfen die Transferlücke zwischen der oberflächenwissenschaftlichen Herstellung von atomar wohl-definierten Oberflächen und deren Anwendung in einer makroskopischen Funktionseinheit zu schliessen.
Der Hauptteil dieser Dissertation besteht aus dem Aufbau und der Inbetriebnahme von einem UHV System, welches fähig ist, vier Inch Wafers zu handhaben und zu prozessieren. Diese Aufgabe entspricht einer Adaption von bekannten Verfahren und Prozessen auf grossflächige Proben. Um diese Prozessadaption zu erleichtern, sind mehrere Ansätze zur Überwachung eines einatomaren Schichtwachstums während eines CVD Prozesses untersucht worden. Unter diesen Ansätzen ist gezeigt, dass eine Kombination aus Reaktionsgasanalyse und in-situ Photoelectronenmengenmessung detaillierte Informationen zum Zustand einer Oberflächenreaktion liefern.
Die Arbeit wird mit Untersuchungen von weiteren Prozessschritten an den hergestellten h-BN/Rh(111) Proben abgeschlossen. Der erste Ansatz ist das Wachstum von makroskopisch dicken Bornitridschichten, welche z. B. direkt ein Substrat für Graphene basierte elektronische Bauteile bieten würde. Der zweite Ansatz beinhaltet das Abtrennen und den Transfer der h-BN Schicht vom Metallsubstrat. Eine solche transferierte einlagige h-BN Schicht könnte als Schutzschicht gegen Wasser oder Oxidation angewendet werden oder Verwendung als dünne Isolatorschicht in einem Elektronischenbauteil finden.
Diese Dissertation konzentriert sich auf Anpassungen und dem Aufbau von neuen Instrumenten und Installationen und soll als Handbuch für einen zukünftigen Experimentalisten dienen. Daher beinhaltet es eingehende technische Beschreibungen.

List of Acronyms

Alq_3	tris(8-hydroxyquinolinato)aluminium
BN	boron nitride
CET	coefficient of thermal expansion
CVD	chemical vapor deposition
DOS	density of states
EDX	energy-dispersive x-ray spectroscopy
EIS	electrochemical impedance spectroscopy
ESCA	electron spectroscopy for chemical analysis
fcc	face centered cubic (lattice)
FWHM	full width at half maximum
h-BN	hexagonal boron nitride
HDD	hot dosing device
HEPA	high efficiency particulate air filter
LEED	low energy electron diffraction
LEEM	low energy electron microscope
mz	mass/charge
OLED	organic light emitting diode
RHEED	reflection high energy electron diffraction
PEEM	photoemission electron microscope
PES	photoemission spectroscopy
PET	polyethylenterephthalate
PID	proportional-integral-derivative (controller)
PMMA	polymethylmethacrylate
SEM	scanning electron microscope
STM	scanning tunneling microscope
t-BN	turbostratic boron nitride
TCS	target current spectroscopy
TDS	thermal desorption spectroscopy
UHV	ultra high vacuum
UPS	ultraviolet photoelectron spectroscopy
UV	ultraviolet (radiation)
XPD	x–ray photoelectron diffraction
XPS	x–ray photoelectron spectroscopy
YSZ	yttria-stabilized zirconia

Contents

1 Introduction

The goal of this thesis was the commissioning and setting up of a new ultra high vacuum (UHV) chamber, which could process four-inch substrates and which was meant to supply collaborating groups with samples. This technical task included the adaptation of the known chemical vapor deposition (CVD) of boron nitride (BN) on rhodium(111) [1] to four inch single crystalline rhodium(111) thin film wafers [2]. For an efficient upscaling of this process, several growth monitoring options with sub-atomic monolayer sensitivity had been evaluated and set up in parallel. One approach, the in-situ photoelectron yield measurement is published in reference [3]. In order to further functionalize the produced four-inch boron nitride coatings two options had been investigated, which were the growth of thick boron nitride layers and the separation and transfer of the single boron nitride layer to an arbitrary substrate.

From a collaboration point of view, a new laboratory was set up within a Sinergia framework, which is an international collaboration of research groups with financial support from the Swiss National Science Foundation. Four groups joined the collaborative work under the project "Boron nitride nanomesh as a template for guided self-assembly of molecular arrays". They are: the surface science group of Prof. T. Greber and Prof. J. Osterwalder at the University of Zurich, the theory group of Prof. J. Hutter at University of Zurich, the nanotech@surfaces group of Dr. O. Gröning at EMPA Dübendorf and the Laboratory for Photochemistry and Spectroscopy of Prof. S. De Feyter at Katholieke Universiteit Leuven.

The goal of joining forces was the exploration of a remarkable UHV processed surface, the hexagonal boron nitride (*h*-BN) on Rh(111). The characteristics of this surface will be discussed in detail in section 1.1. The variety of its properties makes it a valuable candidate for various applications: i) it serves as a template for molecules and atoms [4,5] and ii) is stable in air and various solutions [4,6]. These characteristics were thought to be the key to pave the way towards devices, which were controlled at the molecular or even at the atomic level.

The tasks of the surface science group at University of Zurich was to advance with the exploration of the template capability of the *h*-BN/Rh(111) surface and to upscale its production from 6 mm diameter samples to four-inch wafer samples. For the upscaling a completely new laboratory and UHV system had been set up. An introductory overview of this laboratory can be found in section 1.2 and the new UHV system is introduced in chapter 2. They are commonly referred to as "Sinergia laboratory" and "Sinergia chamber". The large area CVD of *h*-BN is, e.g., achieved in ambient or millibar pressure furnaces on poly-crystalline copper foils [7]. The procedure is in analogy to the one reported for the large scale graphene synthesis [8]. The Sinergia chamber is unique in the application of single crystalline four-inch substrates [9] and its UHV conditions, which ensures the cleanliness of the processes and which leads to a superior deposition quality at the single atomic layer level [2].

All three parts of this thesis –the setup of the UHV chamber, the setup of a process monitoring system and the setups for the further functionalizations– mainly involved the development of solutions for technical problems, which is also reflected in the first author publication list [2,3].

Therefore, this thesis has a strong focus on the detailed description of used technical solutions and installations. From a strategic point of view, this helps optimizing know-how transfer to a future user.

1.1 Single Layer of Hexagonal Boron Nitride on Rhodium(111)

The single layer *h*-BN on Rh(111) forms a corrugated honeycomb superstructure, which is called "*h*-BN nanomesh" [1]. The lattice constant of this superstructure is 3.2 nm [4] and it consists of 13 x 13 BN on 12 x 12 Rh units [10]. Normal emission UPS spectra reveal a splitting of the *h*-BN σ-bands, which can be assigned to two different BN binding regions to the substrate. In the STM images, we distinguish these two regions as the "pores", where the *h*-BN is tightly bound to the substrate, and as the "wires", which only have a pure van der Waals interaction to the substrate [11].
The honeycomb superstructure is an ideal substrate for trapping individual molecules. For instance, trapping of single molecules such as naphthalocyanine is demonstrated in reference [4]. In the case of atoms, the trapping of xenon revealed a peculiar circular potential well in the nanomesh pores [5]. Such a trapping does not only allow to individually explore molecules, but could also be used as substrate for a bottom-up single molecular or atomic device. These findings motivated us to set up a laboratory, which was capable of delivering the single layer of hexagonal boron nitride on Rh(111) at four inch scales.
The Sinergia collaboration demonstrated that a variety of molecules are also trapped in the *h*-BN nanomesh at liquid nitrogen or liquid helium temperatures [12,13]. Additional functionalization of the *h*-BN nanomesh may be realized by Ar^+ ion irradiation, which leads to an atomically controlled structuring of the surface [14]. Ar atoms could be accumulated underneath the BN layer, forming so-called "nanotents" [15] and annealing of these structures leads to 2 nm "voids" within the BN layer [16]. Another potential application as a solution based surface texture switching device still needs to be further explored [17].

1.2 The Sinergia Laboratory

The Sinergia Laboratory is a clean room, which complies with ISO class 7 clean room requirements. It can only be accessed through a two door lock; The windows are sealed; The heat radiators are turned off permanently and the temperature is controlled with the air supply. Air humidity is neither recorded nor maintained, but a particle counter permanently collects data about the airborne particle contamination in the clean room.
Figure 1 shows a schematic overview of the laboratory installations. The core element of the Sinergia laboratory is a UHV system, which is used for the four-inch scale CVD and which is described in detail in section 2. It consists of three chambers: An entry lock, a preparation chamber and an analysis chamber. Each chamber has its own ion or turbo molecular pump and they are isolated with UHV valves. Sample transfer from and into the chamber is only possible through an additional laminar flow box, which secures highest wafer cleanliness for wafer

handling in air before and after preparation. The laminar flow has two high-efficiency particulate air (HEPA) filters (Silence EC 10/10 from LogicAir, Switzerland). The constant air flow and the filters provide an atmosphere, which is cleaner than the detection limit of the particle counter (ParticleScan CR from IQAir, Switzerland), that is a 0.3 μm particle per liter air.

The particle scan unit is able to detect particles with sizes between 0.3 μm - 5 μm. The most delicate particle size for any clean room stress is always the smallest and for the clean room class ISO 7 (definitions ISO 14644-1) these are 0.5 μm particles. Two single week particle histories for particles of that size are displayed in Figure 2(a). The sampling dwell time is two minutes, which allows saving data points for 19.4 days to the internal particle scan memory. Figure 2(b) shows the relative time, within which the 0.5 μm particle contamination was in the limits of ISO 7, 8, 9 or above. The data summarize all recording intervals from March 2013 to March 2014, whereas one interval is between two and three weeks and includes a single floor and particle counter cleaning procedure.

The particle pollution in the Sinergia laboratory depends on its usage. As depicted in Figure 2(a) a labor week influences the cleanliness and at 4.7 % of all time, the 0.5 μm particle contamination exceeds the ISO 7 limit (352 particles per liter air). This is 10 times longer than measured during a non-labor week. Astonishingly, the non-working week also shows increased particle contamination

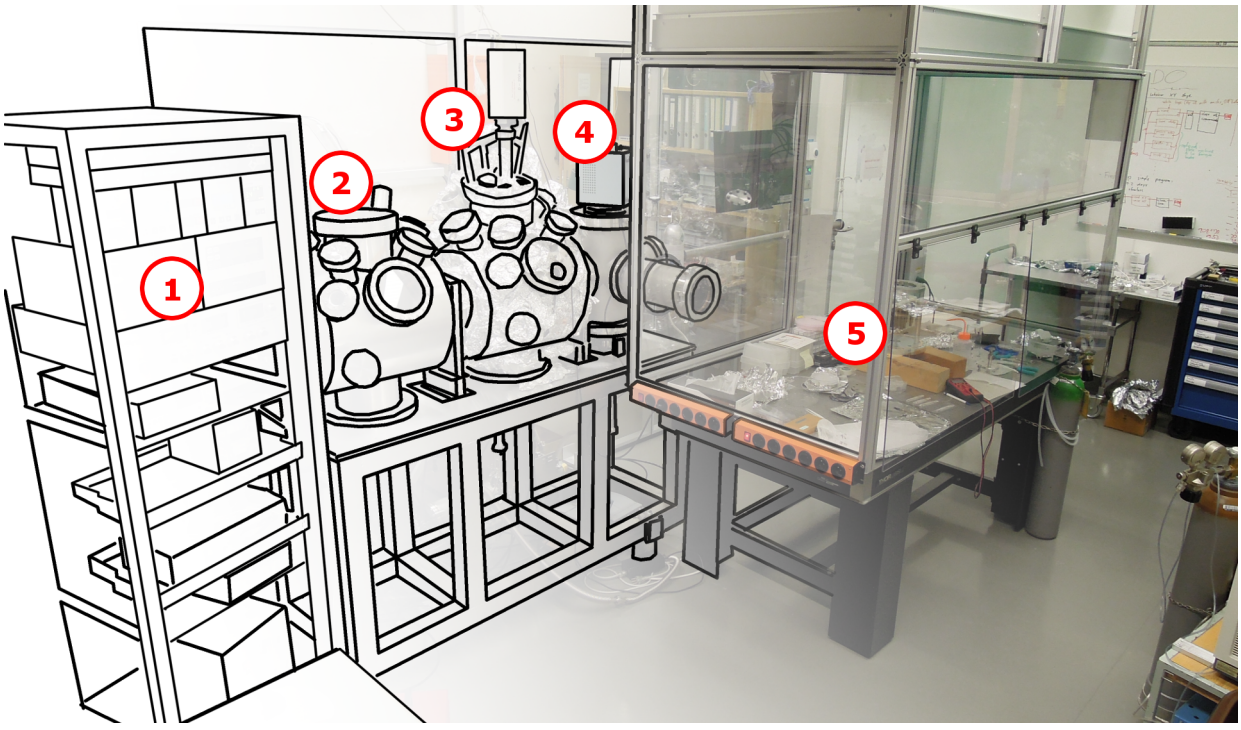

Figure 1: Schematic view of the Sinergia laboratory equipment. (1) Infrastructure rack; (2) Analysis chamber; (3) Preparation chamber with mass spectrometer; (4) Fast entry lock with O_2 plasma cleaner and Ar^+ ion sputtering; (5) Laminar flow unit with access to entry lock and optical table with in air experimental set up. The complete apparatus is located in a clean room which complies with ISO 7 clean room class requirements. From Ref. [2].

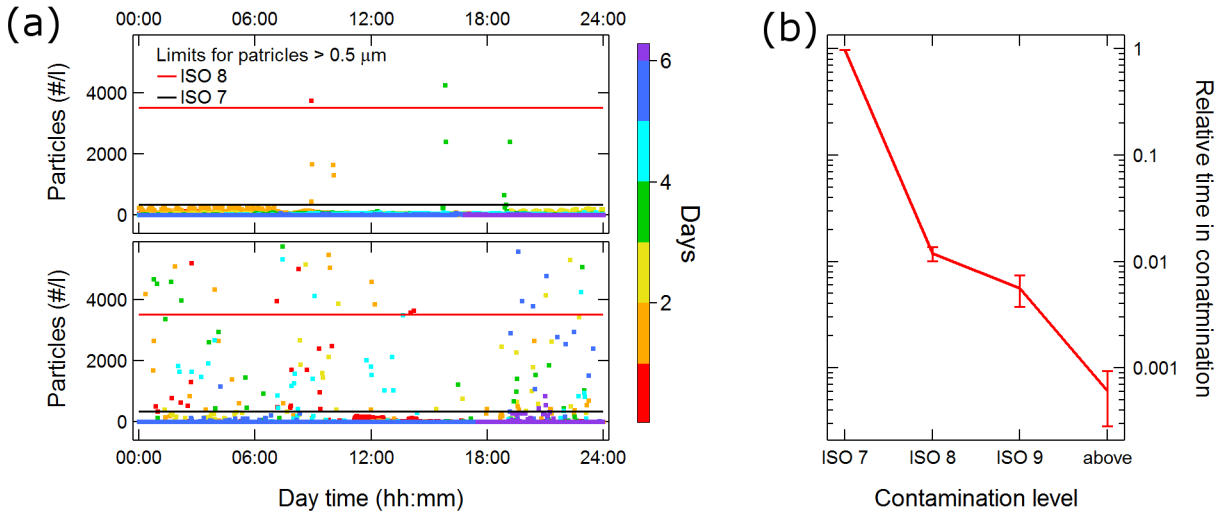

Figure 2: The 0.5 μm particle contamination in the Sinergia clean room. (a) particle counts from a week without clean room work (upper part in (a)) and from a labor week (lower part in (a)). The ISO class requirements are indicated by the red (ISO 8) and black (ISO 7) horizontal lines. The sampling dwell time is 2 min and the particle scan unit had been cleaned prior to both measurements. The data for the working week shows 95.3 % data in ISO 7, 2.2 % in ISO 8 and 2.5 % above. For the non-labor week, 99.6 % of the data are within ISO 7 and 0.2 % in ISO 8 requirements. A complete year of 0.5 μm particle recordings are summarized in (b). They show that 98 % of the time, the contamination is within the ISO 7 clean room limits.

irregularities, especially during the night. Such nightly events seem to be almost absent during the labor week. This behavior can be well understood by knowing that the particle contamination in a closed clean room is mainly caused by dirt rearrangement within the clean room and that during the night the University fresh air supply is switching on and off. Such on and off characteristics could act as driving force for particle rearrangement and explain the nightly increased particle contamination. This effect is highly reduced, if people are working in the laboratory. Working people introduce new particles and allow a particle rearrangement during the day, which increases the overall particle concentration in such a way that they do not relax overnight and cover the air supply switching effects.

2 The Sinergia Ultra High Vacuum Chamber

This chapter is complementary to the information given in reference [2]. It contains a large collection of technical details and is meant to optimize knowledge transfer and to help the future users of the Sinergia chamber to adjust existing installations to their needs and to help identifying possible problems or flaws. For a scientific application of the installations introduced here, the reader is referred to section 2.4.

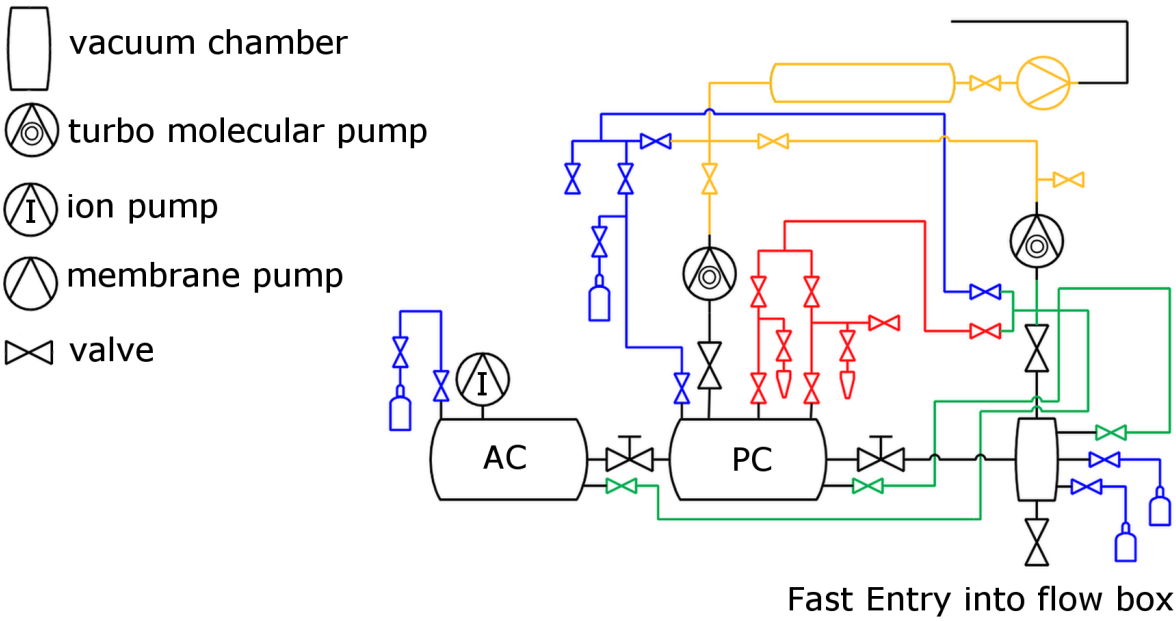

Figure 3: Schematic of the Sinergia vacuum chamber system. **Yellow** is the prevacuum system with membrane pump and prevacuum tank. **Black** is the backbone of the system with entry load lock (**Fast Entry into flow box**), preparation chamber (**PC**) and analysis chamber (**AC**). **Blue** are the gas lines for Ar and O_2. **Red** are the precursor gas lines with glass vials for the precursor storage. For enhanced functionality, each chamber may be differentially pumped by the entry lock turbo pump through the connections in **green**.

The goal of the Sinergia UHV system is the efficient production of UHV processed surfaces at the four inch wafer scale. The substrates are single crystalline thin film wafers with four inch size. They are produced by the Schreck group in Augsburg [9] and a detailed description of the samples is given in the appendix in section 7.1. The system allows sample preparation with ion sputtering, annealing, controlled reactive gas exposure and options for analysis at the four inch scale. Figure 3 shows a schematic overview of the vacuum system. It is divided into three chambers: A fast entry lock, a preparation chamber and an analysis chamber. They all have their own turbo molecular or ion pump and are separated by UHV valves. A 1.44 m long linear feed through enables wafer transport between the three chambers without breaking the vacuum. The base pressure in the analysis and preparation chamber is 1×10^{-10} mbar.
The entry lock can only be accessed via a 2 m^2 laminar flow box, which ensures a clean sample

entry and provides an environment for clean wafer shipment or in air experiments directly after preparation. An inductively coupled 13.57 MHz plasma generator is mounted on top of the entry lock (PDC-3XG, Harrick, USA). Currently, O_2 and Ar plasmas may be generated, but the chamber connections are versatile enough for additional or different gases.
The preparation chamber is equipped with a 100 mm diameter boralectric heater (HTR 1005, Momentive Performance Materials, USA). The wafer annealing position is 16 mm above the heater and heating is mainly radiative. Molybdenum foils shield the radiation at the side and below the heater and a water cooled copper heat sink reduces chamber heating. For the surface preparation, reactive gases may be introduced at specific low pressures through the UHV leak valves. Currently, O_2 and borazine gas lines are available for the single layer boron nitride preparation. A thorough preparation control is possible with three independent systems. A quadrupole mass spectrometer at the top of the chamber allows to monitor gas composition during preparation. Two fused silica windows (Bomco, USA) in mirror geometry can be used for in-situ optical measurements. Moreover, a sapphire view port can be used for coupling of ultraviolet light into the chamber in order to perform in-situ photoelectron yield measurements [3].
In the analysis chamber, a two-axis x-y stage allows scanning of a wafer in the ranges of ± 45 mm and ± 35 mm. The stage is driven by piezo motors (SLC24150-S, SmarAct, Germany) and it is possible to control the wafer position with an accuracy of ± 1 μm and relative scanning with ± 1 nm precision. Currently, the mounting options are an electron source (ELS 100, PSP Vacuum Technology, UK) for target current spectroscopy and an IQE12/38 ion source (Specs, Germany) with a focus of 0.25 mm for sputter structuring or 2 mm for low energy ion implantation [18].

2.1 The Fast Entry Load Lock

The entry lock features several functions, such as introduction of samples without breaking the UHV condition in the analysis and preparation chamber, sample storage, plasma cleaning and reactive ion sputtering. In addition, it may also be used as a differential pumping stage for the other two chambers.
Figure 4(a) provides a cross-sectional overview of the entry lock chamber. A more detailed plan with the key dimensions can be found in the technical drawings section 7.5 in Figure 46. To maintain and measure low pressures, it is equipped with a turbo pump (HiPace 80, Pfeiffer, Germany) and a cold cathode - pirani full range pressure gauge (PKR 251, Pfeiffer, Germany). The base pressure is 2.4×10^{-8} mbar. A VAT air pressure driven valve (blue part in Figure 4(a)) protects the entry lock against unintended vacuum breaking due to electric circuit failure. The unique arrangement of this valve allows efficient gas cleaning or differential pumping of all chambers including the entry lock itself. The drawback of such an organization is that differential pumping is not electric circuit fail safe.
A 21 cm long and 6.8 cm wide glass tube is mounted on top of the chamber. It fits into the excitation coils of an inductively coupled plasma cleaner. At pressures between 0.02 mbar and 0.23 mbar, Ar and O_2 plasmas can be ignited and they are stable down to 10^{-3} mbar. The pressure data shown in Figure 4(b) are measured on the differential pumping line and therefore display a

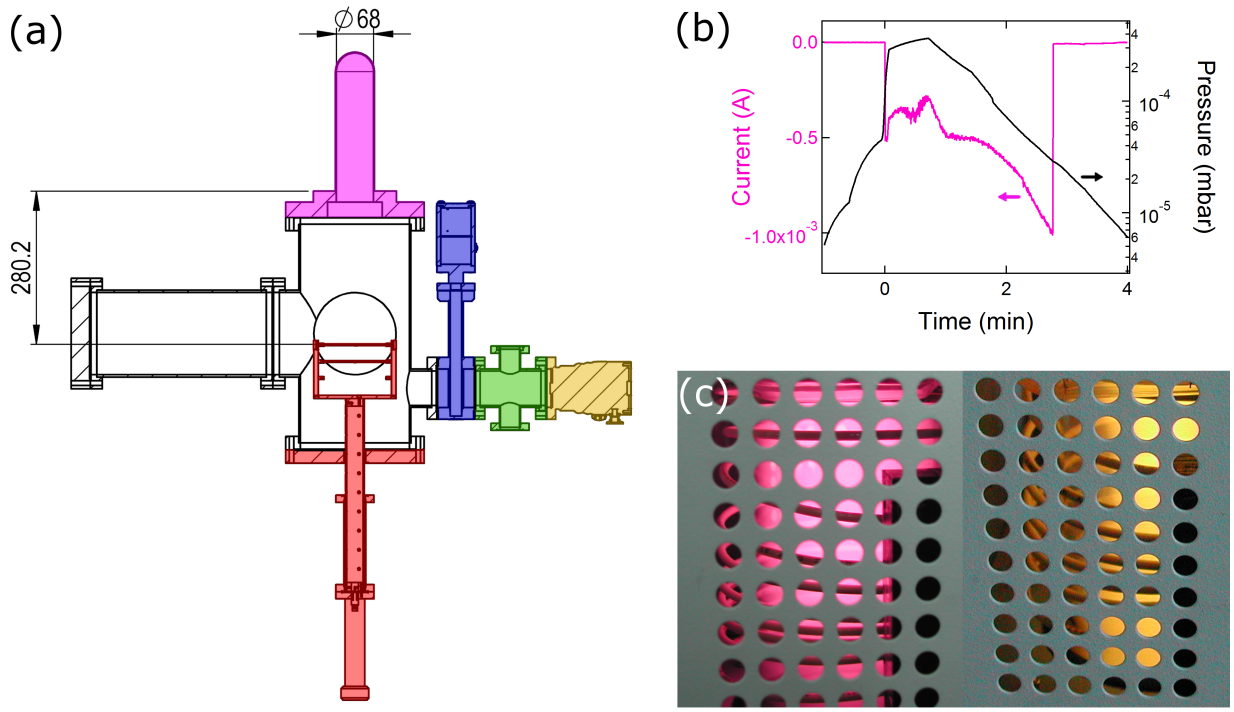

Figure 4: Fast entry load lock functionality. (a) cross section of the fast entry chamber. The turbo pump (**yellow**) can be sealed from the chamber with the VAT valve (**blue**). The CF63-CF40 cross (**green**) allows differential pumping of all three chambers and gas line cleaning. The inductively coupled plasma source (**purple**) is on top of the chamber. The samples might be stored or sputtered on a linear transfer mounted wafer tray (**red**), which is 100 mm movable in positive z-direction. (b) displays the ignition pressure range for an Ar plasma with a sample potential of -500 V. To determine a sputter current density, the measured ion current between 0.5 - 1 mA has to be normalized with the complete top surface of all parts on the sputtering potential, which is about 137 cm^2. (c) displays the color of the Ar plasma in purple and the O_2 plasma greenish-yellow. An air leak would lead to different colors.

lower ignition as well as self-sustaining plasma pressure of 10^{-4} mbar and 10^{-5} mbar, respectively. The color of a clean Ar plasma (purple) and clean oxygen plasma (greenish-yellow) are shown in Figure 4(c). An air leak visibly changes the color of the plasmas. The O_2 plasma had been observed to become white and with larger air leaks blue, while the Ar plasma appeared orange. In a standard operation procedure for plasma cleaning or reactive ion sputtering as applied in section 2.4, the entry lock is pumped differentially through a CF16 bypass and the pumping speed of the turbo pump reduced to 80 %.

The cleaning efficiency of the entry lock plasma is assessed by thermal desorption spectroscopy (TDS) experiments, which are depicted in Figure 5. The experimental protocol was as following: Cleaning of a molybdenum wafer and its holder with 99.8 % ethanol ultra sonic bath for 15 min, drying in the laminar flow of the Sinergia laboratory, re-tightening of the sample holder screws and then 60 mins entry lock treatment, followed by a TDS experiment in the Sinergia preparation

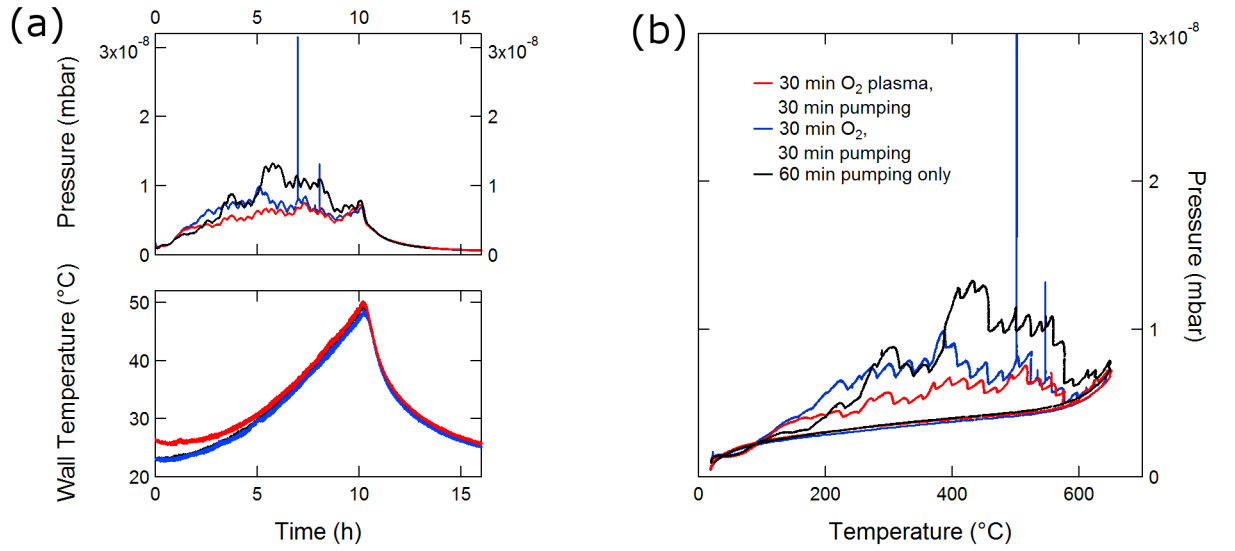

Figure 5: Thermal desorption spectroscopy (TDS) for different sample cleaning procedures. The sample was a molybdenum wafer holder with a molybdenum dummy wafer, both of which were cleaned prior to each experiment with a 15 min ethanol ultra sonic bath. The samples were kept in the entry lock for 60 min under different conditions: (**black**) 60 min entry lock pumping, (**blue**) 30 min 2×10^{-2} O_2 flushing and 30 min pumping, (**red**) 30 min 1.1×10^{-2} mbar O_2 plasma and 30 min entry lock pumping. The subsequent TDS procedures with pressure and temperature evolution are shown in (a), where the upper part visualizes the different pressure reactions upon heating and the lower part shows the chamber wall temperature, which had been used as gas temperature for the TDS evaluation. (b) displays the corresponding TDS spectra with an approximate sample temperature axis as measured by a thermocouple. The plasma cleanliness gain compared to the O_2 flushing is 17.7 % and 37.1 % for no treatment.

chamber. The entry lock treatments include: i) 60 min pumping, ii) 30 min O_2 flushing at 2×10^{-2} mbar, followed by 30 min pumping only, iii) 30 min O_2 30 W plasma at 1.1×10^{-2} mbar, followed by 30 min pumping only. The subsequent TDS data are shown in Figure 5(a). As a gas temperature estimation, a thermocouple mounted on the chamber wall had been used. The TDS spectra for the three cleaning cases are displayed in Figure 5(b) and their wavelike features are artifacts from the smallest discrete heater power step. The very sharp pressure spikes reaching 3×10^{-8} mbar are pressure bursts, which last between 30 - 60 seconds. Their origin is not known. To quantify the cleaning efficiency for the different procedures, the number of desorbing molecules is estimated with the ideal gas law and the pumping speed (V/t) according to equation (1).

$$N = \frac{PV}{k_B T} = \frac{1}{k_B} \cdot \int \frac{P(t)}{T(t)} dt \cdot \frac{V}{t} \tag{1}$$

The temperature $T(t)$ in equation (1) is the gas temperature, which is approximated by the chamber wall temperature. The time integral of the pressure is accessible from the TDS data and the pumping speed of the turbo pump (HiPace 700, Pfeiffer, Germany) is estimated by the

average pumping speed for the tabulated gases (N_2, He, H_2, Ar, CF_4). An unknown factor is the conductance reduction due to a protective grid in front of the turbo pump entrance. In a first approximation we ignore the grid, because its N_2 conductance is listed to be 1962 l/s, which is three times more than the turbo pumping speed. The absolute number of desorbing molecules for the plasma cleaned sample is 3.08×10^{18}, which is 17.7 % less than the O_2 flushed wafer or 37.1 % less than the non-treated wafer.

Three wafers can be stored on a wafer tray (red part in Figure 4(a)), which can be loaded from the air valve in the laminar flow box. A 100 mm linear motion feed through allows z-motion of the wafer tray and in vacuum access to all the three positions. The top position is electrically isolated from the chamber with PEEK plates and can be biased via MHV connections. This allows reactive ion sputtering of a wafer in this position. The functionality of sputtering and its capabilities are shown in Figure 6.

Figure 6(a) displays the electric scheme for the reactive ion sputtering in the Sinergia fast entry lock. Note that the plasma is contained in a glass tube 280 mm apart from the sample (see Figure 4(a)). At low pressures, the plasma stays contained within its tube and ion acceleration across the chamber to the sample is possible. At high pressures, the plasma ignites within the complete chamber and a sputter potential is shielded by the plasma.

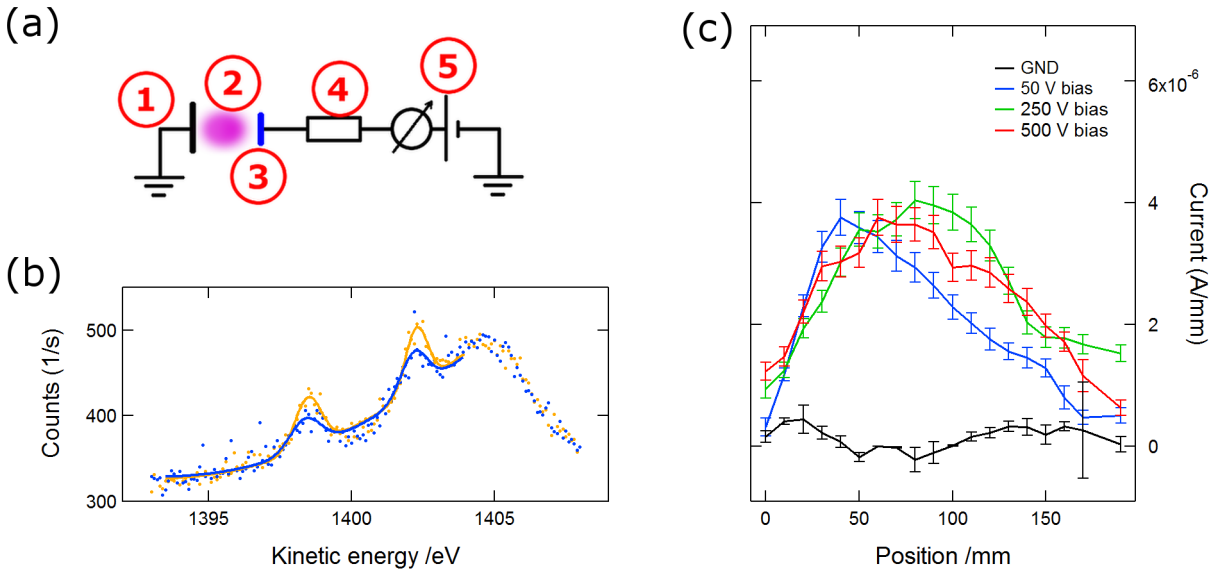

Figure 6: The plasma sputter system in the Sinergia entry lock. The electric scheme (a) consists of grounded chamber wall (1), Ar plasma (2), wafer sample and its sample holder (3), two high power resistors (2×47 kΩ) (4), current measurement and high voltage module (5). (b) displays the Al Kα Au4f peaks from a gold contamination in the surface of a Rh thin film. (**orange**) is the spectrum before and (**blue**) shows the spectrum after sputtering. The elemental ratio between the gold contamination and the rhodium substrate was reduced from 0.34 % to 0.27 %. (c) The spot size of the Ar plasma was measured with a knife edge and indicates an ion spot size larger than 100 mm at different acceleration potentials.

To confirm the sputtering capability, a Rh thin film sample with an Au contamination on the surface had been sputtered for 10 mins at -200 V bias and 5×10^{-4} mbar Ar. The x–ray photoelectron spectroscopy (XPS) Al Kα data displayed in Figure 6(b) show a 21 % decrease of the Au4f core level signals, comparing the spectra before and after sputtering.
The plasma spot size was estimated by translation of a grounded Al plate above the biased sample. Figure 6(c) displays measurements at different sample bias. Because ions are accelerated by the bias on the sample and not by an potential cage around the ionization area, the spot appears slightly tilted, especially for a low sample bias. Nonetheless, the measurements confirm a broad ion distribution across the 100 mm wide four-inch wafer, which allows a homogenous large area sputtering.

2.2 The Preparation Chamber

The UHV preparation chamber has the identical flange design as the analysis chamber and a detailed overview of the flange geometries is given in the appendix section 7.5 in Figure 47. The wafer position in the analysis chamber is in the chamber center, whereas the heating position is 90.7 mm lower. That is the reason for some flanges to point towards the center and some towards the heater position. Because the Sinergia chamber is mainly intended to serve preparation purposes 78 % of the flanges are pointing towards the heater position.
The core part of the preparation chamber is the heater. A cross section and assembly of which is given in Figure 7. A detailed plan of the heater flange and its electronic scheme can be found in the appendix in Figure 48 and 49. Operation of the heater is controlled by the analog output of a national instruments card, which also records thermocouple voltages, heater current and voltage. A LabView interface, based on Luc Pazellers heating program, allows not only experimental control, but is also easy extendable for the implementation of additional functionality, e.g. growth control features as described in chapter 3.
A temperature sensor contacting the heater was not possible and two thermocouples are mounted between heater and water cooled copper heat sink. Their indicated temperature underestimate the heater temperature, since they are cooled from one side. The wafer temperature may be directly measured by pyrometers from the chamber top.
Heater, wafer holder and shield geometry are the most crucial factor for an efficient heating. Boralectric heater suppliers like tectra (tectra, Germany) recommend a screw fixed double wall shield around the heater. The Sinergia heater originally had only three bottom molybdenum shields, which were held in place by gravitation. They were located together with a 2 mm diameter steel guide for the thermocouples between heater bottom and the copper cooler, which are 3 mm apart. This geometry led to a shifting of the Mo shields, which induced mechanical stress to the heater, and a breaking of the steel tube, which originally guided the thermocouples. The geometry in spring 2014 has the steel tube replaced by a much thinner Ta foil spot welded thermocouple guide as visible in Figure 7 and one of the Mo shields is removed. Furthermore, a cylindrical heat shield is mounted around the heater, which reduces the heating power for a Ir thin film wafer from 680 W to 530 W in order to reach 880 °C.

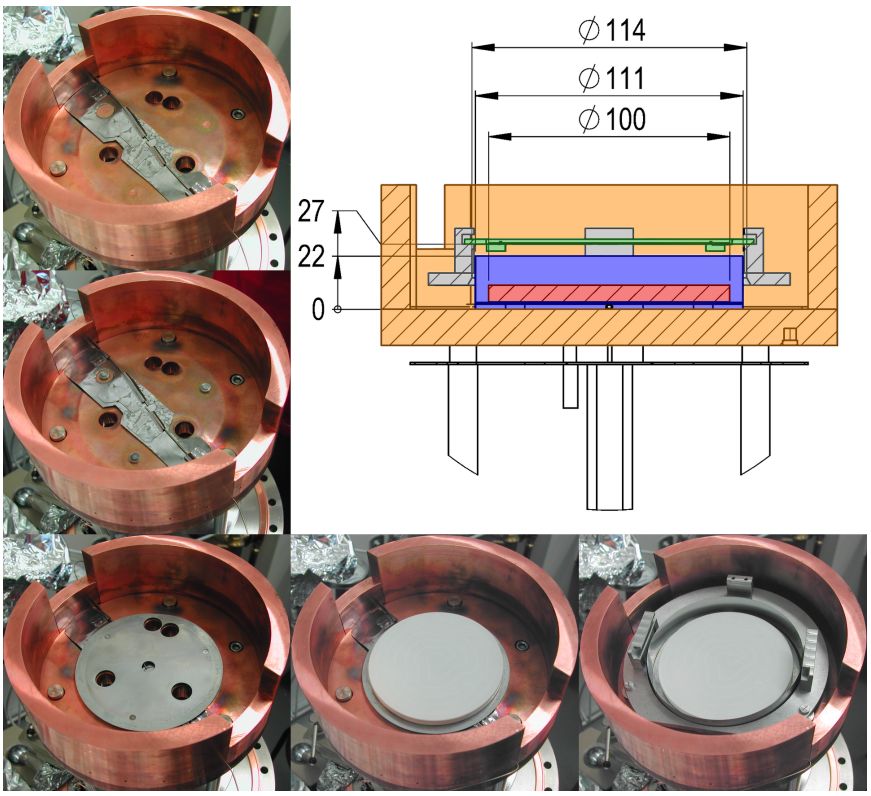

Figure 7: Heater assembly and its schematic cross section. **Orange** is the copper cooler, which is water cooled at the bottom. **Red** is the boralectric heater, which is surrounded by molybdenum shields in **blue**. Marked in **gray** is the wafer stage, which can lift the wafer holder from the heating position to the chamber center for sample transfer. The **green** colored area are the wafer holder and the wafer itself. All parts directly around the heater are made out of molybdenum, only exceptions are the tantalum wires for the shield fixations, the tantalum thermocouple fixation and the steel thermocouples themselves (TEMI306-K10/550 from Transmetra, Switzerland). The pictures around the cross section display the heater assembly, starting with the thermocouples, Mo spacers, Mo shields, heater and ending with the wafer stage.

A standard procedure for the four inch nanomesh preparation is a 5 h process, which will heat up the chamber wall to about 54 °C. Currently, the chamber wall is insulated by Al foil, which covers the heating tubes (SRT052-080-LSE, omega, USA) for baking the analysis and preparation chambers. In this configuration, the base pressure at nanomesh preparation temperature is 4.4×10^{-9} mbar with 54 °C chamber wall temperature. If this pressure is too high, several techniques might be applied, suggested here in order of complexity: i) turning the heater off for several hours before the crucial preparation step. A one hour preparation may only reach a chamber wall temperature of 30 °C. ii) cooling of the chamber wall with water cooling guides, which are already mounted, but not connected. iii) changing the heating shield configuration, such that they comply with the suppliers assembly design.

For in-situ process control, there are two growth monitoring options available, which are further described in chapter 3. In addition, a quadrupole mass analyzer (QME, Pfeiffer, Germany) is

mounted on the chamber top. An application example of the in-situ growth monitoring systems can be found in section 2.4.2.

2.3 The Analysis Chamber

The analysis chamber except its chamber wall cooling option is identical to the preparation chamber and its flange design can be found in the appendix in Figure 47. Because the Sinergia UHV system is optimized for preparation purposes, there are only two flanges pointing to the analysis position, apart from the top and side flanges.
The top CF200 flange is equipped with a pot like CF200-CF100 reduction flange, such that any CF100 analysis equipment is 159 mm closer to the sample surface. Figure 8 displays an overview of this reduction flange with the two available instrumentation options. The configuration with the electron source option is shown in Figure 8(a) and its capabilities discussed in section 2.3.1. The ion source option is displayed in Figure 8(b) and its potentials are thoroughly discussed in the Bachelor thesis of M. Graf [18]. This is the reason, why the ion source is only briefly introduced

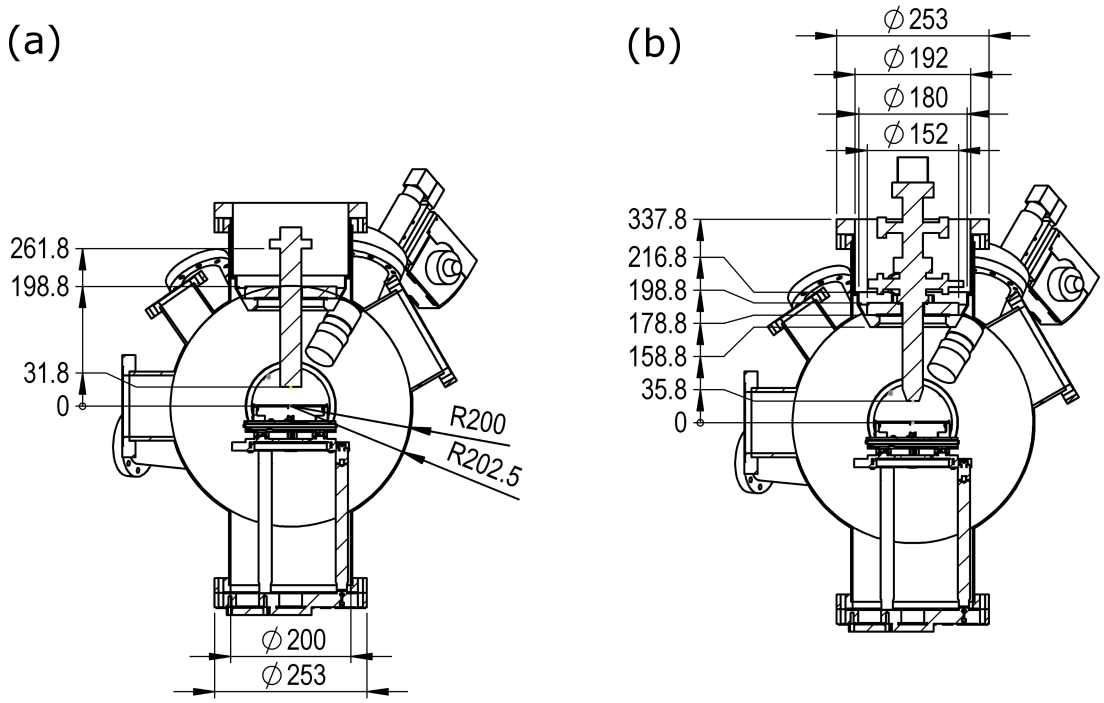

Figure 8: Cross section of the analysis chamber with the electron source ELS100 (a) and the ion source IQE12/38 in (b). The vertical zero coordinate marks the wafer surface position. The electron source has a working distance of 31.8 mm, which could be reduced by shortening the 63 mm long CF40 extension tube. The IQE12/38 ion source has a working distance of 35.8 mm and it is not possible to further reduce this distance. The CF 200 bottom flange holds the x-y stage, which has a maximum circular diameter of 198 mm, the largest possible diameter to fit into its flange tube. A microscope is permanently mounted on the right of both installations, which corresponds to flange F5 in the appendix 7.5 in Figure 47.

in section 2.3.2.

A two-axis x-y stage is located in the center of the chamber. It allows scanning of a wafer in the ranges of ±45 mm and ±35 mm. The stage is driven by piezo motors (SLC24150-S from SmarAct, Germany) and it is possible to absolutely position the wafer with ±1 μm accuracy and relative scanning with ±1 nm precision. The LabView interface for x-y scans was programmed by C. Bernard.

2.3.1 Target Current Spectroscopy

An electron source (ELS 100, PSP Vacuum Technology, UK) allows to perform normal incidence target current spectroscopy (TCS) [19]. This source provides electrons up to 100 eV with 250 meV full width at half maximum (FWHM). Figure 9(a) shows a schematic overview of the experimental setup.

To record a spectrum, the electron source potential is kept constant, which ensures a constant electron current I_0 at any energy. The kinetic energy of the incident electrons E_{kin} is scanned via the sample bias U_{bias}. Equation (2) is an expression for the electron source and sample contributions to E_{kin}, including the source work function Φ_{gun} and the sample work function Φ_s.

$$E_{kin} = eU_{gun} + \Phi_{gun} - eU_{bias} - \Phi_s \tag{2}$$

Figure 9(b) visualizes the energy level scheme as postulated by equation (2). To measure a sample current, the condition $E_{kin} \geq 0$ has to be fulfilled. In particular, the current onset marks

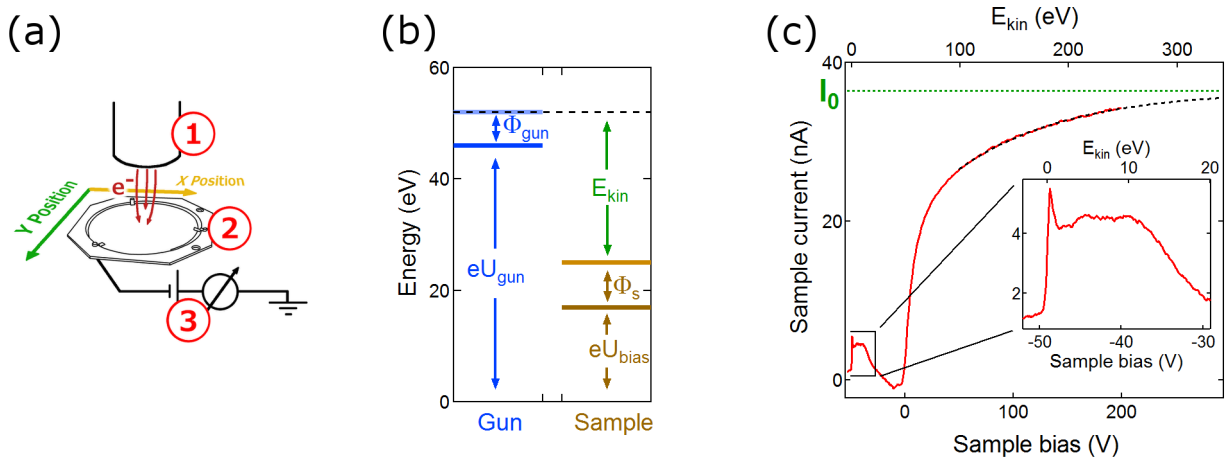

Figure 9: The target current spectroscopy (TCS) analysis option in the Sinergia chamber. (a) schematically visualizes the target current spectroscopy setup. An electron source (1) provides electrons up to 100 eV. They probe a wafer (2), which is positioned on the x-y stage. A source measure unit (3) scans the sample bias and measures the current. An energy scheme is given in (b), where the zero energy level refers to ground. The electron source potential ($\mathbf{U}_{\text{gun}}$) and the filament work function (Φ_{gun}) are kept constant, while the sample bias ($\mathbf{U}_{\text{bias}}$) is scanned. This measurement protocol leads to TCS spectra as shown in (c).

the sample bias required for $E_{kin} = 0$, which is the constraint to transform the sample bias into electron kinetic energy as depicted in the top scale in Figure 9(c). In addition, the spectrum at high positive sample bias can be fitted with an exponential function, which allows to extract the electron source current I_0 (see dotted lines in Figure 9(c)). Because the source energy and filament power is kept constant during a measurement, I_0 enables to define an electron absorption $(I(E)/I_0)$ or reflection coefficient $(1 - I(E)/I_0)$ at any of the probed electron energies E_{kin}. Note that those coefficients can be negative, which is the case, when an incoming electron causes the emission of more than one electron.

An iridium thin film wafer with a melted gold patch has been used to assess the spacial resolution of the electron source. The gold patch has been prepared by C. Bernard and an image of it is given in Figure 10(a). Figure 10(c) displays the TCS spectra at low kinetic energies from a scan through the test wafer. The current onset is marked in green, i.e. where the incident kinetic electron energy E_{kin} is zero. In addition to an onset contrast from the gold patch, the onset displays a 0.5 eV shift across the complete wafer. This onset slope appears independent of sample and is assumed to be caused by a non-ideal sample-electron beam alignment and magnetic fields.

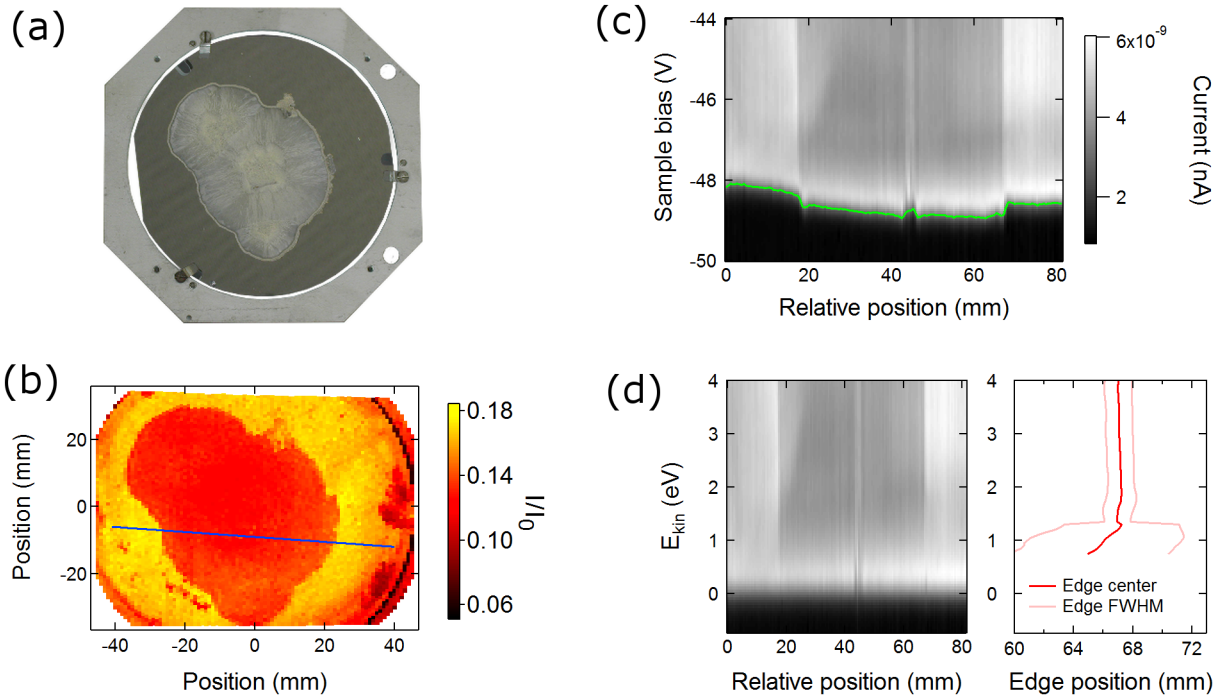

Figure 10: Low energy electron imaging and scanning target current spectroscopy (TCS). (a) image of a melted gold patch on an iridium thin film wafer. (b) electron absorption image of 5 eV electrons for the same wafer. The blue line marks the positions of the TCS measurements in (c). The green line in (c) indicates the sample bias for an incident electron energy $E_{kin} = 0$ with a constant source potential of 50 V. (d) displays the TCS spectra from (c) in terms of kinetic energies E_{kin}. This allows to determine a spot size FWHM of 2 mm at incident electron energies above 1.3 eV. (a) and (b) are adapted from Ref. [2].

To correct this apparent slope, the TCS spectra are expressed in terms of kinetic energies. Figure 10(b) is a constant kinetic energy map at 5 eV for this wafer. To determine an electron spot size, the position and width of the Ir-AuIr step is evaluated in Figure 10(d). It reveals that the spot size becomes larger, the lower the kinetic energy and only appears constant with a FWHM of 2 mm above a kinetic energy of 1.3 eV. Because the kinetic energy scale is referenced to the current onset, at energies where the electron spot size is largest, the vicinity of the Ir-AuIr step will induce a misleading kinetic energy reference. Such an incorrect kinetic zero energy, does not only depend on the vicinity of a step but also on its geometry as well as on its elemental composition. Therefore, the effects of a step edge have to be determined based on the according situation. Here, we compare the edge position of the current onset (Figure 10(c)) with the edge position at high electron energies (Figure 10(d)). The shift yields an estimate on, how far from the edge position the energy zero reference is deceptive. In the particular case of an Ir-AuIr step, the TCS spectra display an energy reference shift of ±0.8 mm.

The TCS option of the Sinergia analysis chamber is a valuable analysis option for comparison between two spectra, e.g. before and after a preparation step. It does not provide absolute measurements of physical properties such as the work function, but it is sensitive enough to detect the difference between an *h*-BN/Rh(111) or a cleaned Rh(111) thin film, which will be shown in section 2.4. The large spot size and its dependence on the sample inhomogeneity make the system suitable for scanning a complete homogenous wafer rather than detecting small defects or scanning small structures.

2.3.2 High and Low Energy Ion Exposure

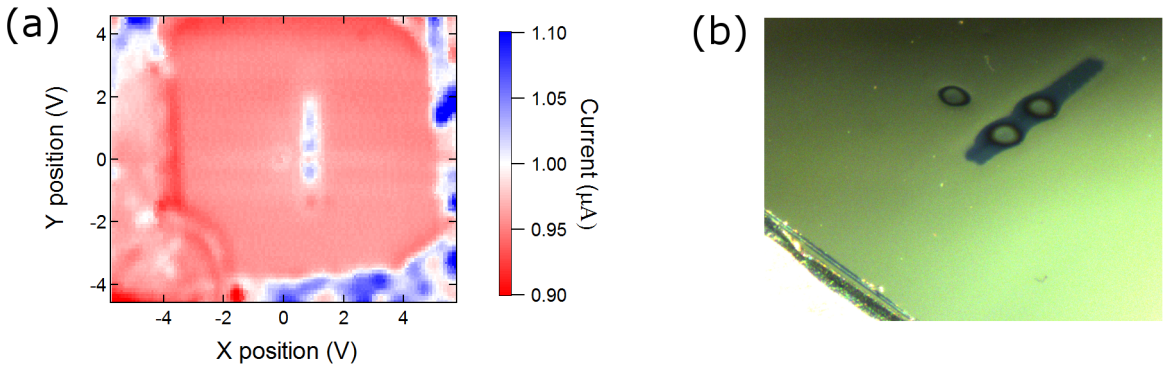

Figure 11: Scanning and sputtering with the IQE12/38 ion source in the Sinergia chamber. (a) displays a sample current image of a 9 mm x 9 mm Ni thin film sample with an Ar^+ ion irradiation of 2.5 keV. Scanning was done with the internal deflection unit of the ion source. Prior to this image, three holes and a stripe had been sputtered into the 170 nm thick Ni film. (b) shows the optical image of the same wafer from the microscope mounted on flange F5 (see appendix Figure 47).

Figure 11 displays the performance of an ion source implemented in the Sinergia analysis chamber. This second mounting option is an IQE12/38 ion source (Leybold, now distributed by Specs, Germany), which allows ion irradiation between 200 eV - 5 keV. The adaptation of the ion source to the Sinergia analysis chamber has been accomplished by Manuel Graf within his Bachelor thesis [18]. He also explored the low energy ion output for possible nanotents applications [14].

2.4 Preparation and Characterization of the *h*-BN Nanomesh

This section reviews the findings of the nanomesh preparation in the Sinergia UHV chamber. The Rh thin film wafer samples were obtained from M. Schreck, Universität Augsburg, Germany. These Rh films are grown on Si(111) wafers with an yttria-stabilized zirconia (YSZ) buffer layer [9]. Their surface morphology, temperature stability, impurity contamination and their development over the past years are summarized in the appendix in section 7.1.

2.4.1 The First Preparations

The first *h*-BN nanomesh preparations on Rh(111) were based on a non-sputtering procedure by T. Brugger [20]. He recognized that the main thin film contamination was carbon, which could be removed by a series of oxygen exposures at elevated sample temperatures.

Figure 12 displays the analysis of the BN coating from the first wafer. At that time, the Sinergia chamber had no analysis instrumentation and prior to any measurement, the wafer had to be cut in air and small parts of it were introduced into other UHV systems. The STM image in Figure 12(a) displays a partially nanomesh covered surface and a large density of small nanomesh "domains", some with different orientation. This is inline with the LEED pattern in Figure 12(b), where the nanomesh superstructure pattern is faintly visible, but an additional 30° rotated reflex appears. The elemental composition, i.e. the ratio of B:N:C was for all investigated samples in the order of 1:1:1. In addition, zirconia from the sample buffer layer could as well be detected, which indicated an incomplete Rh coverage of the YSZ/Si(111) substrate. Whether the Rh film had been incomplete before the *h*-BN preparation is not known, since our XPS instrumentation does not allow the examination of a sample with four-inch size.

The small domains of the *h*-BN nanomesh in Figure 12(a) could be related to a large number of nucleation sites, which had been shown to be dependent on the number of preadsorbed molecules [21]. In particular, it is assumed that an incomplete carbon removal did not only increase the nucleation sites, but made it also impossible to efficiently substitute the carbon contamination by boron nitride [22, 23]. In the following, the oxygen treatment had been extended from 125 Langmuir (1 Langmuir = 1s $\times 10^{-6}$ Torr) of T. Brugger to a multiple of it. To find the proper amount of oxygen, a sample-carbon-response procedure has been established and is described in the following section 2.4.2.

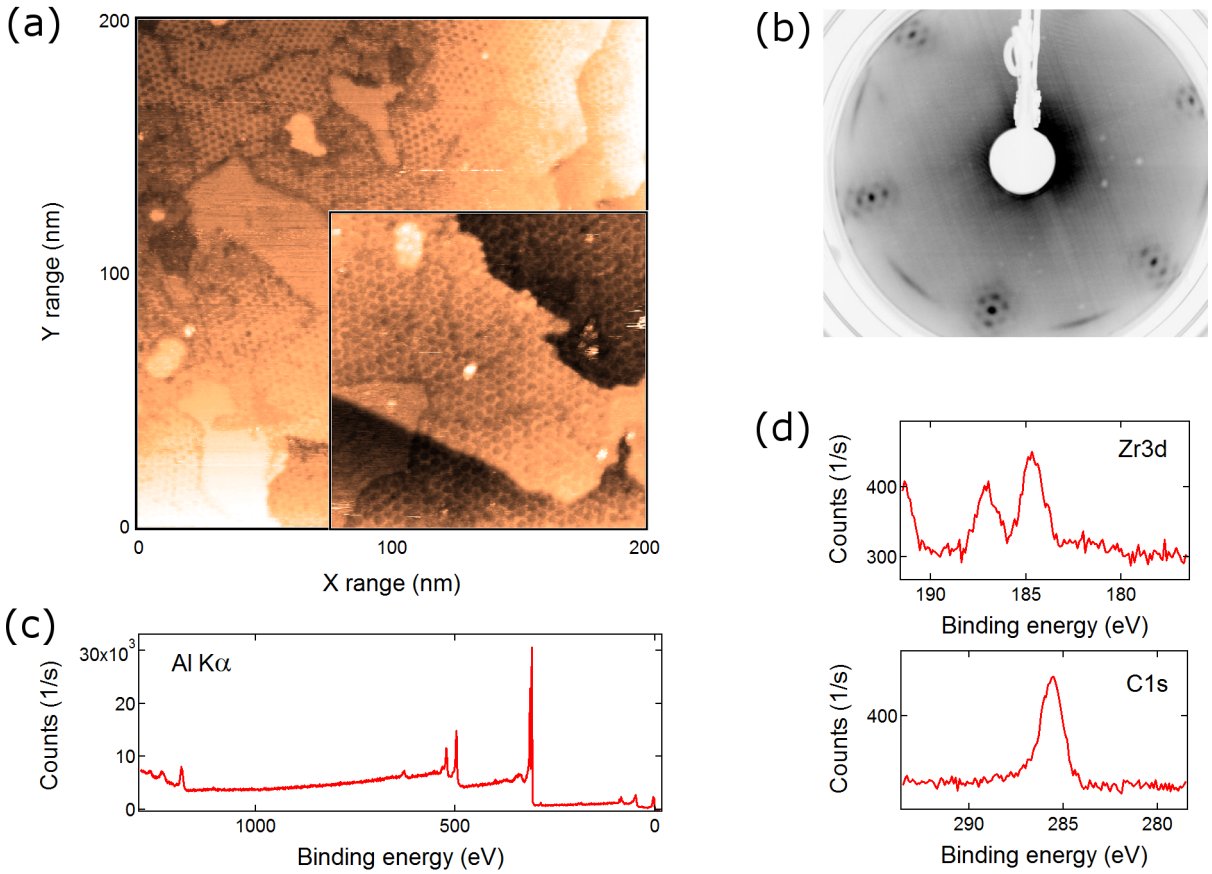

Figure 12: Resulting boron nitride layer of the first wafer preparation. (a) STM images. The inset is a 100 nm × 100 nm detail. The nanomesh partially covers the surface and forms small domains. (b) 60 eV LEED pattern, with faint nanomesh fingerprint and misaligned 30 ° rotated domains. (c) and (d) are XPS spectra with the monochromatic Al Kα x-ray source, which reveal a carbon and zirconia contamination. The emerging peak at the lowest electron kinetic energy in the Zr3d spectrum in (d) belongs to the B1s core level.

2.4.2 Wafer Preparation and in-situ Process Monitoring

Because of the carbon contamination of the boron nitride layers described in the previous section 2.4.1, the wafer cleaning procedure was adjusted and the Sinergia cleaning capabilities were extended. The adjustment of the cleaning procedure is described in this section, while the extension of the cleaning capabilities with oxygen plasma and reactive ion sputtering are introduced in section 2.1.

To minimize sample surface contamination due to shipment or from the Rh deposition process itself, a wafers is cleaned in and out of vacuum prior to any CVD preparation step. The standard procedure starts with an isopropanol ultrasonic bath of 15 mins. The wafer is then dried with the metal on top in an oblique position in the Sinergia laminar flow box. This procedure removes a large amount of surface contamination, which is originated by airborne particles. A drawback of this liquid treatment is that the isopropanol will not completely evaporate from the surface.

Nevertheless, this first treatment step provides a well-defined initial sample condition before any treatment in UHV. The second step is mounting of the wafer and application of an oxygen plasma. The effects of 30 min oxygen plasma are discussed in section 2.1. For this step, the sample is grounded in order to avoid wafer charging, which might influence the plasma cleaning efficiency. The third and fourth step involve Ar^+ ion sputtering followed by a 13 h degassing routine up to about 600 °C. After degassing, the wafer is Ar sputtered once more. This should remove segregated contaminations, which are not only carbon, but also gold impurities from the Rh thin film deposition. This last sputtering step involves at least 0.5 hours Ar^+ bombardment at potentials of 0.5 kV and at lowest possible pressures (see Figure 4(b)). The low pressure regime is important, such that the plasma visibly stays contained in its glass vial and ions do not get neutralized or decelerated on their way to the wafer.

The final CVD preparation step involves a procedure, which is adapted from the non-sputtering preparation scheme of T. Brugger [20]. Figure 13 displays data from a wafer preparation in the Sinergia chamber. The entire preparation cycle may be found in the growth control chapter 3 in Figure 22(b). It consists of four oxygen dosings at increasingly higher temperatures with

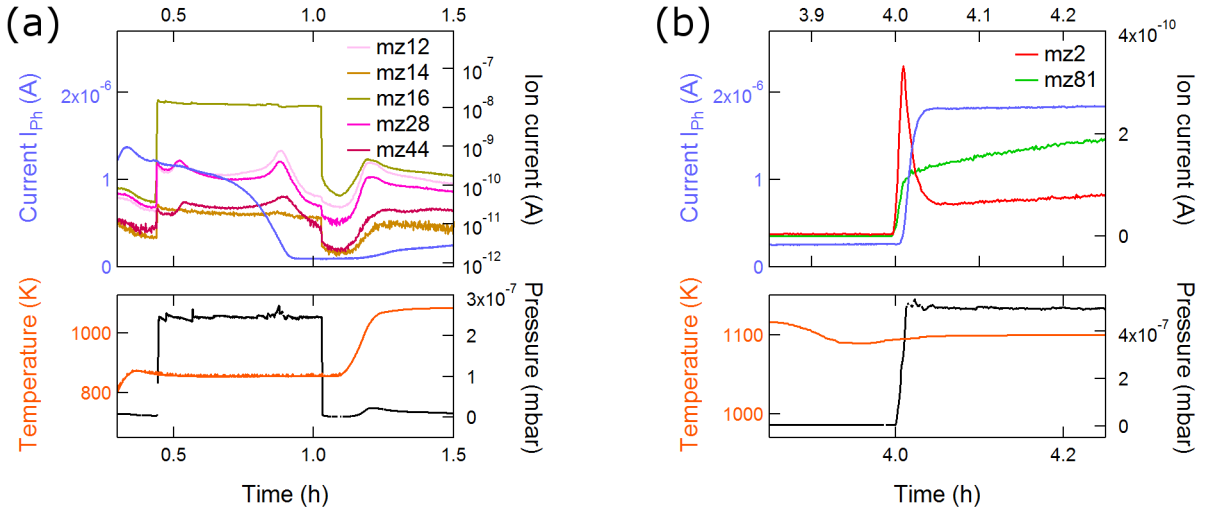

Figure 13: Data from the Sinergia wafer preparation, the complete preparation cycle can be found in Figure 22(b). The graph in (a) displays the first oxygen dosing event. The lower part indicates the preparation conditions, which are 2.5×10^{-7} mbar O_2 at a sample temperature of about 860 K for 0.58 h. The upper part displays the sample photocurrent yield and the evolution of selected masses (mz corresponds here to mass/charge). (b) shows the borazine dosing event for the same preparation. The lower part indicates the preparation conditions with a borazine pressure of 5×10^{-7} mbar for 0.5 h at a sample temperature of 1100 K. The first 15 mins of the reaction are displayed here. The upper part displays the borazine ion current (mz 81), the H_2 evolution (mz 2) as well as the sample photocurrent yield. The hydrogen spike indirectly measures the surface reaction, where borazine forms boron nitride through hydrogen loss, whereas the photocurrent I_{Ph} is directly related to a work function shift of the surface.

subsequent high temperature flashing and terminates with the application of borazine. The setup and the exact meaning of the sample photocurrent yield, which is also displayed in Figure 13, are introduced in detail in section 3.3. Here, it is sufficient to know that the larger the photocurrent, the lower the sample work function and vice versa.

The data in Figure 13(a) show the wafer preparation conditions for the first oxygen dosing event. The wafer is at a moderate temperature of about 580 °C. This temperature is chosen at the Rh film deposition temperature [9], which is at least 250 °C below the following CVD procedure. The purpose of this low temperature is to minimize the high temperature exposures, during which the sample may be destroyed as described in the appendix in section 7.1. The selected masses/charges (mz) in the upper part correspond to carbon related fragments, i.e. mz 12 for C^+, mz 28 for CO^+, mz 44 for CO_2^+. Mass/charge 14 for N^+ excludes N_2^+ contributions in mz 28 and mz 16 for O^+ ensures the supply of enough reactive oxygen. Mz 12, mz 28 and mz 44 display a synchronized evolution, which is independent of mz 14 and mz 16. This indicates the removal of a carbon contamination. The carbon removal maximum at the absolute preparation time of about 0.75 h is accompanied by a photocurrent yield reduction from the sample surface. Such a decrease is expected for an oxidation of the Rh surface. Combining this surface response with the carbon removal information from the mass analysis of the reaction gas, this event can be interpreted as the successful substitution of a carbon contamination with oxygen on the rhodium substrate. In this sense, the mass spectrometer and the surface photocurrent yield provide complementary information about the sample cleanliness and allow in-situ adjustment of the oxygen amount for cleaning a sample surface. For this particular wafer, an amount of 400 L O_2 had been necessary, whereas for other wafers less or even quantities of more than 800 L appeared to be appropriate. After high temperature flashing, this flexible O_2 dosing procedure is repeated at an increased temperature of about 680 °C. The last two O_2 dosing events correspond to the procedure as proposed in appendix B in reference [20].

Figure 13(b) displays the beginning of the borazine dosing event. Here, we use a temperature of 830 °C and a borazine pressure of 5×10^{-7} mbar. The selected masses/charge in the upper part are mz 2 for H_2^+ and mz 81 for borazine$^+$. The formation of h-BN from borazine is only possible through the loss of 6 hydrogen atoms per borazine molecule. This loss can be in-situ monitored by mz 2 in a mass spectrometer and is found for the h-BN formation on Ni(111) in reference [24]. Here, the mz 2 signal behaves accordingly and the exponential decay of the H_2^+ signal corresponds to the reaction attenuation by the BN covered Rh surface. An independent experiment, which indicates that the BN covered Rh does not contribute to the surface reaction anymore, can be found in reference [25]. In parallel to the H_2^+ signal decay, the photocurrent yield is increased, which corresponds to a decrease of the work function and can be well interpreted as the formation of a BN layer on the Rh substrate. Again, a combination of gas analysis and surface photocurrent yield allows to draw conclusions about the sample surface status.

One of the first successful h-BN preparation procedures included a borazine dosing interval of 0.5 h at 5×10^{-7} mbar borazine. As the cleaning of the wafers evolved and became i) more sophisticated and ii) could be monitored in- situ, this last preparation step has not been updated

so far. Currently, the photocurrent yield or H_2^+ ion current in Figure 13(b) indicate a *h*-BN formation time of about 10 min (225 L), which is much shorter than the dosing event itself. It is therefore suggested here, to reduce the borazine partial pressure, which might reduce the domain and defect density of the *h*-BN nanomesh in future preparations.

2.4.3 Sinergia *h*-BN Nanomesh Characterization

This section does only deal with measurements in the Sinergia UHV chamber itself, a more detailed wafer analysis after cutting can be found in reference [2].
To characterize a rhodium thin film wafer in the Sinergia UHV chamber, target current spectroscopy (TCS) measurements were performed as introduced in section 2.3.1. Because the system does not allow the absolute measurement of a thin film property, the wafer was measured twice –once before and once after borazine application. The comparison of these two measurements is shown in Figure 14.
Instead of mapping the complete wafer at a certain incident kinetic energy as in Figure 10(b), only a cross section along the wafer diagonal Y = 0 is given in Figure 14(b). This allows to directly compare the electron absorption before ($I/I_{0,Rh(111)}$) and after borazine dosing ($I/I_{0,h\text{-BN}}$) on the same sample bias axis.
The electron absorption before borazine ($I/I_{0,Rh(111)}$) has been measured after a cleaning procedure as introduced in the previous section 2.4.2. The comparison of the sample bias at the current onset before and after preparation reveals a 1.4 V shift. This shift is indicated by the blue area in the spectra of Figure 14(a) or appears as blue stripe across the wafer in the subtracted spectra in Figure 14(b). Normal emission UPS measurements with a single crystalline Rh(111) surface and for the same preparation, indicated a work function decrease from 5.66 eV to 4.23 eV [3], which is in line with the 1.4 V shift.
Besides the apparent work function shift of 1.4 eV across the complete wafer, the TCS spectra also reveal a reduced electron absorption for *h*-BN/Rh(111), which is marked by the red areas in Figure 14. This corresponds to an enlarged electron reflectivity, which might inspire future experiments, where electron reflection is assessed by transport measurements above or below the *h*-BN nanomesh on Rh(111).

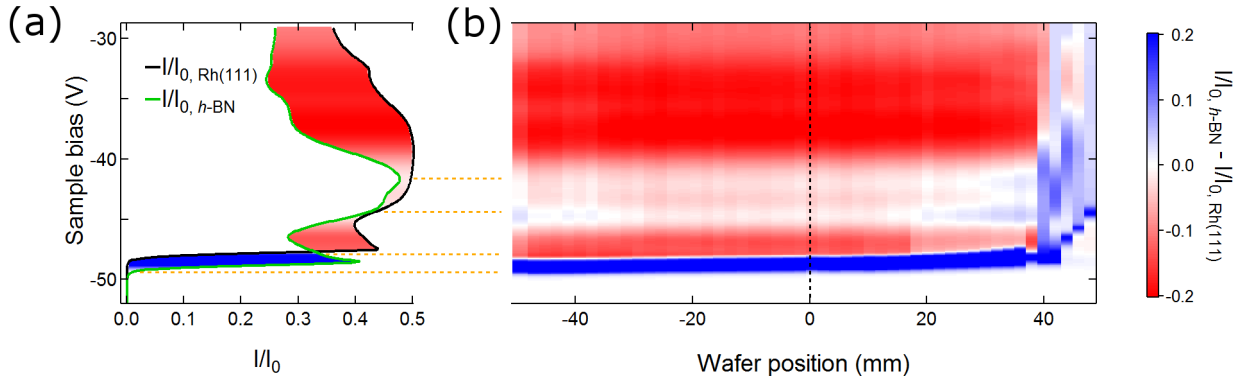

Figure 14: Target current measurements on the Y = 0, X = ±45 mm wafer cross section before and after h-BN preparation. The incident electron energy is 50 eV. (a) displays the measured data at the position (X,Y) = (0,0). The electron absorption for the pristine Rh(111) is given by $I/I_{0,Rh(111)}$, and the electron absorption for the system h-BN/Rh(111) is named as $I/I_{0,h\text{-BN}}$. The dotted lines are guides to the eye. The data in (b) show the difference between the pristine Rh(111) and the h-BN/Rh(111) across the complete Y = 0 wafer cross section. The red-blue color coding is the same as in the spectra in (a). A larger electron absorption before the BN coating is coded in red and a smaller electron absorption in blue. The red part indicates a reduction of sample current caused by the single layer of h-BN. The blue, 1.4 eV broad stripe reveals a work function lowering across the wafer. The uniformity of the measurement indicates a complete and homogeneous boron nitride growth on the four-inch wafer, except for spectra with X $\geq$ 40 mm, where the edge of the wafer and a molybdenum clip induce a retarding field distortion (see Figure 10(a)). These measurements were performed without intermittent air exposure or cutting. From Ref. [2].

3 Atomic Single Layer Growth Control

3.1 Motivation for Establishing CVD Growth Monitoring

The Sinergia chamber was set up as a preparation chamber for the application of well-established processes and procedures from the electron spectroscopy for chemical analysis (ESCA) UHV chamber [26]. For the first boron nitride preparations, the Sinergia UHV chamber was not yet equipped with an analysis chamber and the analysis instrumentation was limited to a mass spectrometer. Due to the early preparation failures, it was decided to focus on and develop an inexpensive in-situ growth monitoring system, rather than setup an analysis chamber.
In-situ atomic submonolayer sensitivity can be achieved with many commercially available instrumentation such as a low energy electron microscope (LEEM) [27], a reflection high energy electron diffraction unit (RHEED) [28], or a photoemission electron microscope (PEEM) [29]. Those instrumentation are costly and maintenance intensive and therefore beyond the request for a simple system.
Mass spectrometer monitoring during CVD growth was the only method of process control and it is described for the single layer of boron nitride on Ni(111) by W. Auwärter [24]. An example of an indirect reaction monitoring by gas analysis can also be found in section 2.4.2. Several growth control possibilities, where the measured signal directly probes the surface, had been evaluated, two of them are described in detail in the sections 3.2 and 3.3. The optical approach with ellipsometry in section 3.2 did profit from an earlier Kerr effect setup of G. Landolt [30]. The optical cage could be adopted to the Sinergia UHV chamber, but most optical elements including the light source as well as the measurement system were exchanged. The xenon flash lamp project in section 3.3 was designed and setup for room temperature experiments by H. Cun. Here, the setup had been enhanced by an efficient data acquisition and by an adaptation to UHV CVD experiments and it is published in [3].

3.2 Optical Approach, Ellipsometry

Visible light had been used for a long time for matter inspection and e.g. thin film thickness determination. The main advantage of a light in – light out method for monitoring a CVD process is its gas pressure independence, while light coupling in and out of the chamber is rather challenging, especially for non-constant window temperatures. The principle of modern ellipsometry goes back to P. Drude, which describes a setup equivalent to the one presented here [31]. In the following, the physics of light reflection at absorbing surfaces is summarized according to an optics textbook [32], the Sinergia setup is introduced and its capabilities are presented.

3.2.1 Introduction to Ellipsometry

Light reflection at surfaces is always associated with light polarization changes. Figure 15(a) displays an overview of the situation for linearly polarized light with a polarization angle $\Psi_{in} = 45°$ being reflected at an absorbing surface. The reflected light is attenuated, has a tilted polarization

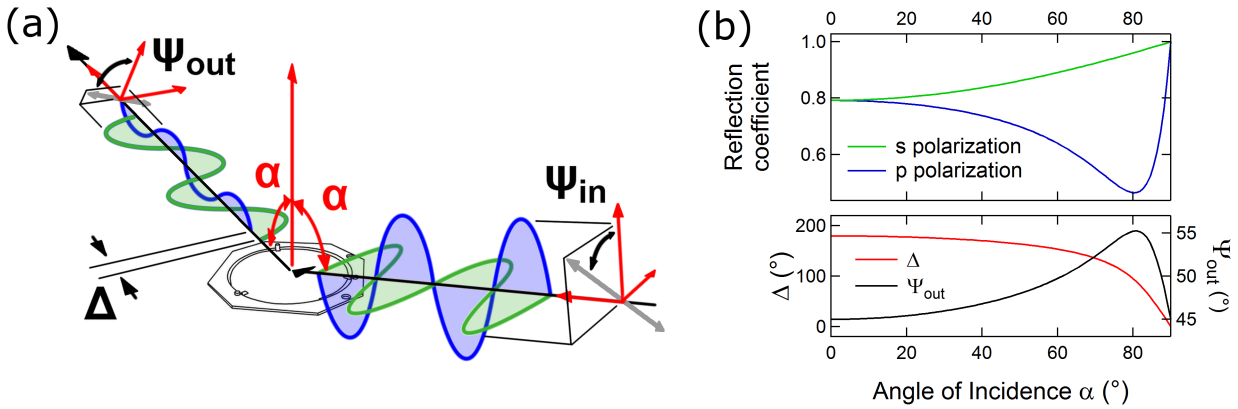

Figure 15: The reflection of light at an absorbing surface. A schematic overview of light reflection is shown in (a). Linearly polarized light with an azimuth $\Psi_{in} = 45°$ is reflected at an absorbing surface. **Blue** is the E-field component parallel to the incoming and outgoing light beam plane, which is generally referred as the p-orientation plane (p for parallel, $\parallel$). **Green** is the E-field component perpendicular to the p-polarization direction, which is the s-plane direction (s for the German "senkrecht", i.e., perpendicular, $\perp$). The reflected light beam has an overall reduced intensity, the polarization is tilted towards the s-direction and it is elliptically polarized with a phase shift Δ. (b) displays light reflection calculations with a rhodium reflector, an ingoing polarization azimuth $\Psi_{in} = 45°$ and a He Ne laser with a wavelength of 632.8 nm. The upper part shows the light attenuation, while the lower part accounts for the phase shift Δ and the outgoing polarization Ψ_{out}.

and is elliptical. Figure 15(b) displays calculations for light reflection on rhodium. Such calculations reveal the expected effects on the reflected light, are substantial for the data interpretation and shall be introduced according to the formalism used in [32].
The Fresnel equations describe the evolution of the parallel ($E_\parallel$) and perpendicular ($E_\perp$) E-field components of light upon reflection or transmission at an isotropic medium. Following the formalism used in the textbook [32], the Fresnel equation for reflection are given in equations (3) and (4). We distinguish a parallel orientation ("$\parallel$") to the plane described by the incident and reflected beam and a perpendicular orientation ("$\perp$"). They are commonly known as the p-polarization and s-polarization orientation, respectively.

$$q_{r\perp} = \frac{E_{r\perp}}{E_{i\perp}} = -\frac{(\sqrt{n_{rel}^2 - \sin^2\alpha} - \cos\alpha)^2}{n_{rel}^2 - 1} \tag{3}$$

$$q_{r\parallel} = \frac{E_{r\parallel}}{E_{i\parallel}} = \frac{n_{rel}^2 \cos\alpha - \sqrt{n_{rel}^2 - \sin^2\alpha}}{n_{rel}^2 \cos\alpha + \sqrt{n_{rel}^2 - \sin^2\alpha}} \tag{4}$$

Here, the index "i" stands for incident and "r" for reflected light and the abbreviation n_{rel} is the relative refractive index $n_{rel} = n_{sample}/n_{vacuum}$. The angle α is the angle between surface normal and light beam, as depicted in the scheme in Figure 15(a). In this form, these expressions

are only valid for transparent samples. If a sample absorbs light, such as a metallic surface, the Fresnel equations (3) and (4) are still valid but they become complex along with the refractive index. Equation (5) introduces the complex refractive index n'_{rel} with the absorption index κ. Depending on the literature, the absorption index might be defined as the full imaginary part of the complex refractive index, which corresponds to $n_{sample}\kappa$ within the formalism used here. The physical meaning of the absorption index is light absorption of the sample material. For normal incidence light, the intensity is reduced by a factor of e^{-1} at a penetration depth of $\lambda/(4\pi n_{sample}\kappa)$.

$$n'_{rel} = \frac{n_{sample}}{n_{vacuum}}(1 - i\kappa) \tag{5}$$

To emphasize the importance of the incident light polarization, the effects of a complex refractive index are discussed in detail. The incident E-field can be decomposed into its parallel (blue in Figure 15(a)) and perpendicular (green in Figure 15(a)) components, for which only the incident polarization azimuth Ψ_{in} needs to be known. Additionally, since the Fresnel equations yield a complex number, they can be rewritten in Euler notation.

$$E_{r\parallel} = E_{i\parallel} q_{r\parallel} = E_i \cos(\Psi_{in}) |q_{r\parallel}| \exp i\delta_{\parallel} \tag{6}$$

$$E_{r\perp} = E_{i\perp} q_{r\perp} = E_i \sin(\Psi_{in}) |q_{r\perp}| \exp i\delta_{\perp} \tag{7}$$

In case of $\Psi_{in} = 45°$, the incident light contribution can be eliminated by simple division of equation (6) with equation (7). Thus, it is possible to derive an expression for the relative contributions of $E_{r\parallel}$ and $E_{r\perp}$, which is the outgoing polarization azimuth Ψ_{out}.

$$\frac{q_{r\parallel}}{q_{r\perp}} = \frac{|q_{r\parallel}|}{|q_{r\perp}|} \exp i(\delta_{\parallel} - \delta_{\perp}) = \frac{|q_{r\parallel}|}{|q_{r\perp}|} \exp i\Delta \tag{8}$$

$$\frac{|q_{r\parallel}|}{|q_{r\perp}|} = \frac{|E_{r\parallel}|}{|E_{r\perp}|} = \tan(\pi/2 - \Psi_{out}) \tag{9}$$

The complex angle Δ between the parallel and perpendicular reflected light component is the phase shift, which only occurs for reflection at an absorbing medium and is absent for a transparent sample. Apart from this physical meaning, equations (8) and (9) connect the measurable quantities Δ and Ψ_{out} with the Fresnel equations (3) and (4) and with the material quantities n_{sample} and κ. Knowing the medium constants, which are for rhodium at 632.8 nm $n_{Rh} = 2.15$ and $\kappa = 5.61/n_{Rh}$ [33], it is possible to calculate the expected Δ and Ψ_{out} for any angle of incidence α. Figure 15(b) displays such a calculation for Rhodium. In addition of Ψ_{out} and Δ, the reflection coefficients for both p- and s-polarization are evaluated according to equation (10). These reflection coefficients yield the expected reflected light intensity and they indicate that rhodium reflects about 80 % of the incident light.

$$R_{\parallel \text{ or } \perp} = |q_{\parallel \text{ or } \perp}|^2 = q_{\parallel \text{ or } \perp} \bar{q}_{\parallel \text{ or } \perp} \tag{10}$$

So far, the Fresnel equations are used to determine an expected light phase Δ and polarization rotation Ψ from a known complex refractive index. It also works the other way around. That is, the materials refractive index may be determined from a measured Δ and Ψ. The mathematical expressions can be derived from equations (3) - (9) and are displayed here in equations (11), (12), (13) and (14).

$$A = n_{rel}^2(1-\kappa^2) = \tan^2\alpha \sin^2\alpha \frac{\cos^2 2\Psi_{out} - \sin^2 2\Psi_{out} \sin^2\Delta}{(1+\sin 2\Psi_{out}\cos\Delta)^2} + \sin^2\alpha \tag{11}$$

$$B = 2n_{rel}^2\kappa = \tan^2\alpha \sin^2\alpha \sin 4\Psi_{out} \sin\Delta/(1+\sin 2\Psi_{out}\cos\Delta)^2 \tag{12}$$

$$\kappa = -\frac{A}{B} + \sqrt{1+(A/B)^2} \tag{13}$$

$$n_{rel} = \sqrt{A/(1-\kappa^2)} \tag{14}$$

The angle α is again the angle of the incident light as depicted in Figure 15(a) and the variables A, B are used to abbreviate the expressions.

3.2.2 Setup and Performance

In-situ reflectivity measurements were first realized in the Osterwalder group with an optical setup, which was designed and constructed by G. Landolt [30]. Due to its low long term stability the setup was revised and is introduced here. Additional information about the developments of the setup are given in the appendix in the ellipsometry section 7.2.

Figure 16(a) shows a schematic overview of the latest setup. It includes all optical components for determination of the light polarization orientation Ψ_{out} and phase shift Δ. The light source is a 4 mW He Ne laser emitting at a wavelength of 632.8 nm. The light beam is split immediately after the laser, one part of which is probing the sample and the other part is recorded as reference signal to correct for laser intensity instabilities. The probing linearly polarized light part passes through a $\lambda/4$-plate and is reflected at the sample. Then it passes a thin film polarizer and is detected by a photodiode. The two photodiodes are mounted in a light tight housing and the laser beam can only enter through a narrow band pass filter. The diodes are slightly tilted with respect to the laser beam axis, such that back reflected light does not interfere with the other photodiode or the laser itself.

Figure 16(b) shows a schematic overview of the electronic circuit. The two photodiodes are detecting light in short-circuit operation and each diode has its own measurement unit (digital multimeter, Keithley 2100, USA). The measurements are synchronized with a LabView software trigger from a computer. The power line for the two multimeters used did show a considerable influence on the measurement in the instruments lowest current range (see appendix section 7.2). The effects were small, appeared as sudden current shifts and were in the order of the expected surface signal changes. Therefore, two passive line filters were employed in series between power lines and the two Keithley 2100 units. These filters did decreased the sudden shift behavior, but could not completely remove them.

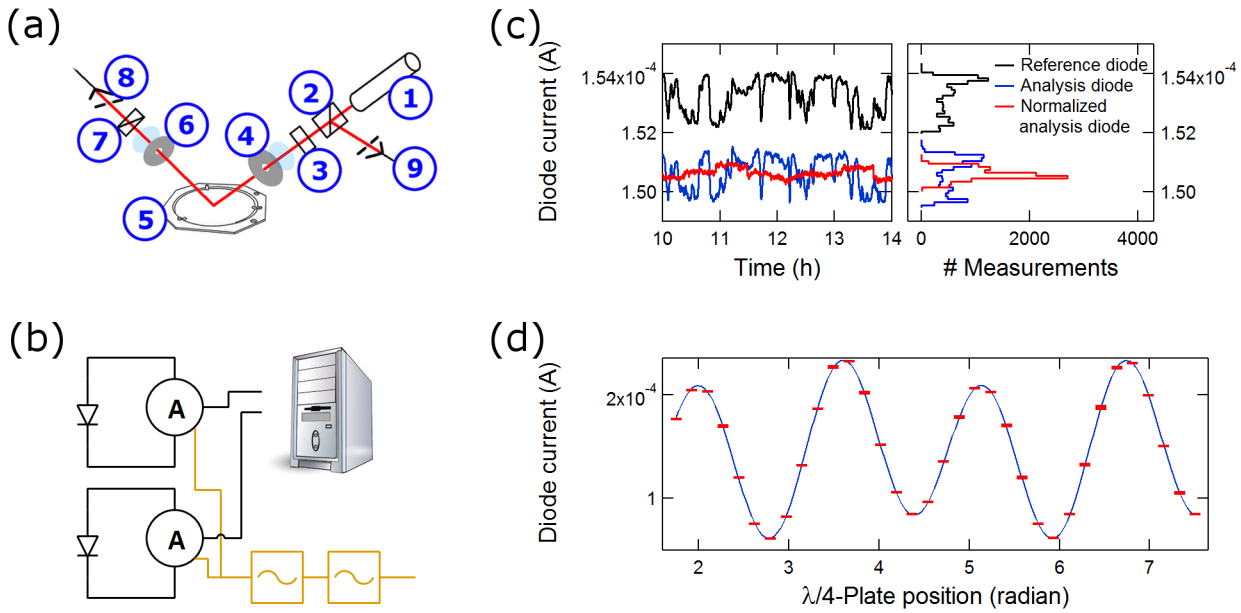

Figure 16: The optical setup and its capabilities. (a) is the schematic overview of the ellipsometry setup: (1) He Ne laser, (2) polarizing beam splitter, (3) $\lambda/4$-plate, (4) & (6) windows and heat shields, (5) wafer sample, (7) thin film polarizer, (8) analysis photodiode, (9) reference photodiode. (b) current recording scheme with two independent measuring circuits for both photodiodes. The amperemeters are triggered by a computer and their power supply line is equipped with two passive phase filters. (c) visualizes a four hours measurement without any sample manipulation and reveals laser light fluctuations in the 0.38 % regime. Normalization of the analysis current with the reference diode suppresses most fluctuations down to 0.12 %. (d) displays the analysis diode photocurrent with a rotating compensator.

Figure 16(c) displays the photodiode current for the analysis and reference electrode in a four hours interval, which corresponds to about the time interval of a standard preparation procedure. The diodes record fluctuations, which are in the 0.36 - 0.38 % range of the signal. These instabilities are laser intensity variations and they are minimized by normalization of the analysis signal with the reference diode reading. The standard deviation of the normalized signal is in the order of 0.12 %. The remaining noise is small enough to reveal sudden signal shifts, which may occur in intervals of 34 mins. They appear for at least 5 times during four hours. The reason for such current shifts was identified to be an artifact of the Keithley 2100 measuring units and they could be reduced by power line filters as schematically drawn in Figure 16(b). Additional information about this issue is given in the appendix section 7.2.

To measure the phase shift Δ and polarization rotation Ψ_{out}, the simplest method is the Null ellipsometer configuration [34]. The analyzing polarizer and the $\lambda/4$-plate are adjusted until the detecting photodiode measures zero, which is a non trivial task, since they depend on each other. This zero signal can only be achieved, when the quater-wave plate compensates the sample induced ellipticity and the analyzing polarizer cancels the sample induced p-polarization decrease. The final orientation of these optical elements reflect the light modulation of the sample. However,

light intensity at such a signal minimum is least sensitive to, e.g., a light polarization rotation. This is visualized in Figure 17(a), where a polarizer rotation meets the Null ellipsometer condition twice. At these positions the angle derivative of the light signal becomes infinitely small, which directly reflects its sensitivity. Therefore, it is not the method of choice for the Δ and Ψ_{out} determination. An improved procedure is the rotating-compensator ellipsometer configuration [35]. The reflected light intensity is recorded during a $\lambda/4$-plate rotation and the signal modulations allow to determine the absolute polarization and phase shift. Rotation of the compensator plate by hand allows to record rotating-compensator data, which are shown in Figure 16(d). The fitted function is the one introduced by Hauge *et al.* [35].

3.2.3 In-situ Ellipsometry of Atomic Single Layer Deposition

The goal of the ellipsometry setup is the in-situ monitoring of a CVD process in the atomic single layer regime. Such an application requires lowest drift or noise for a preparation time of about 4 hours. Therefore, there is no rotating optical element in the light path and the setup is not suitable for a brief and accurate identification of Δ and Ψ.

Prior to a measurement the most sensitive polarizer and $\lambda/4$-plate configuration are identified. The incident light polarization azimuth is fixed at a position of 45°, which eliminates effects of the incident light on the reflected beam polarization and phase shift as shown in equations (6) – (9). Firstly, the Null ellipsometer configuration is achieved with the analyzing polarizer and the $\lambda/4$-plate (see section 3.2.2). Figure 17(a) shows the photocurrent of the detection diode for a

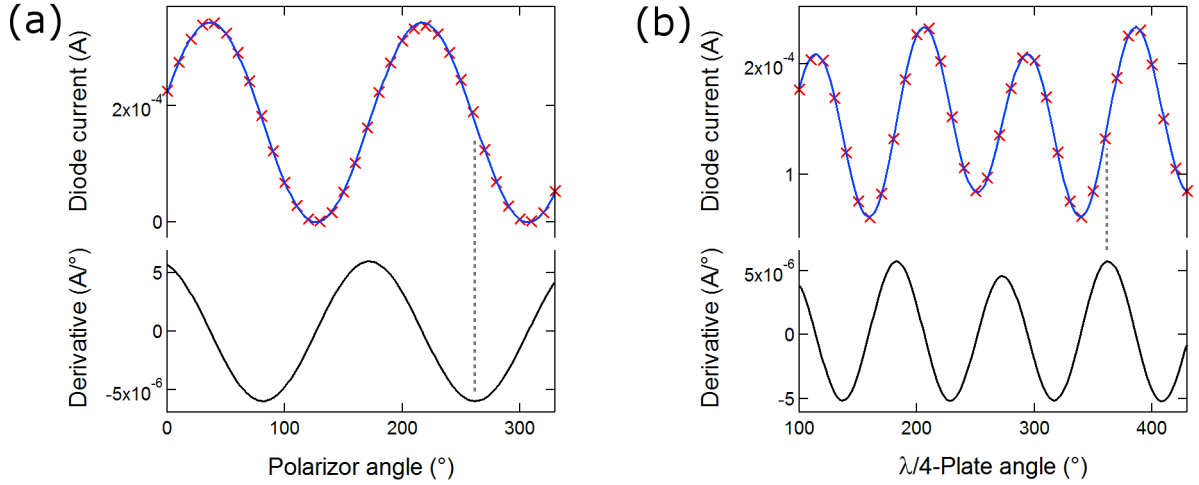

Figure 17: Optimization of the optical element configuration prior to any measurement. The incident light polarization of $\Psi_{in} = 45°$ is fixed, which determines the orientation of the polarizing beam splitter. The initial condition is the Null ellipsometer configuration, where the orientation of the thin film polarizer is optimized as shown in (a). Maximum sensitivity is reached at the orientations with the largest derivative. The $\lambda/4$-plate orientation is optimized subsequently in (b). The dotted lines mark the configurations of the thin film polarizer and the $\lambda/4$, receptively, which were used for the measurements shown in Figure 18.

polarizer rotation in the Null ellipsometer configuration. Its derivative reveals the most sensitive analyzer azimuth angles to record Ψ_{out} shifts. The gray line displays the chosen analyzer azimuth of 262°, which has a sensitivity for Ψ_{out} of $5.96 \cdot 10^{-6}$ A/°. Figure 17(b) displays a $\lambda/4$-plate rotation at optimized polarizer azimuth identified in part (a). The gray line here indicates the configuration for the best Δ sensitivity of $5.72 \cdot 10^{-6}$ A/°, which was used to measure the following in-situ ellipsometric data. Comparing these sensitivities to the noise of a four hours experiment (Figure 16(c)), it leads to a noise level of 0.032(1)° in Ψ as well as in Δ.
The photodiode records an intensity, which can be determined for known Δ and Ψ with equation (10), but cannot be disentangled into a Ψ or Δ component. This means that during a CVD process, phase and polarization shift effects might enhance or even annihilate each other. To identify the Ψ and Δ contributions, one could perform a rotating-compensator experiment before and after the CVD process [35], or repeat the experiment with different analyzer or $\lambda/4$-plate orientation.
Figure 18 visualizes the results of an in-situ ellipsometry experiment. The sample was a Rh(111) thin film. For a single layer boron nitride preparation, oxygen has to be applied above 700 °C [20], followed by a borazine exposure above 750 °C [1]. Because the largest optical signal drifts are induced by temperature changes of the BK7 standard windows, a careful 10 h heating ramp to a preparation temperature of about 800 °C is chosen. Before the application of any reactive gas, the temperature is kept at 800 °C for about 8 h. As displayed in Figure 18(a), the gas dosing starts after about 18 h, where the ellipsometry signal drift appears to be linear and the window temperature is stabilized at 35 °C. To reproduce the findings of a single borazine exposure with the same sample, it was re-exposed to O_2 until the optical signal prior to borazine reappeared. Figure 18(b) displays a borazine exposure and an oxygen event of the oxygen cleaned sample. It reveals that surface changes at the atomic single layer level can optically be measured. However, the method is not suitable for a rigorous growth or quality control, because the recorded signal shifts are about three times the FWHM of the signal itself. Additionally, it requires a very slow (18 hours) heating procedure, which is not practical for sample preparations.

3.2.4 Conclusion and Outlook

As shown in Figure 18(b) it is possible to optically monitor atomic single layer deposition processes. But the procedure does neither allow to easily determine a real optical constant of the sample nor could be used for quality control due to a signal to noise ratio of 3:1. Furthermore, the measurement system suffers from thermal drifts, which limits heating procedures and makes it unsuitable for short in-situ experiments. The electronic recording system also suffers from instabilities, which happen to be in the order of the recorded signal shifts as identified in Figure 18(b), but can be distinguished, due to their sudden appearance.
Although the ellipsometry setup is challenging to be used for in-situ single layer growth monitoring, several aspects have space for improvements. The thermally induced signal drift from the standard BK7 windows could be minimized by stress decoupled fused silica windows, which are already mounted on the Sinergia UHV chamber. The electronic read out part could be better synchronized

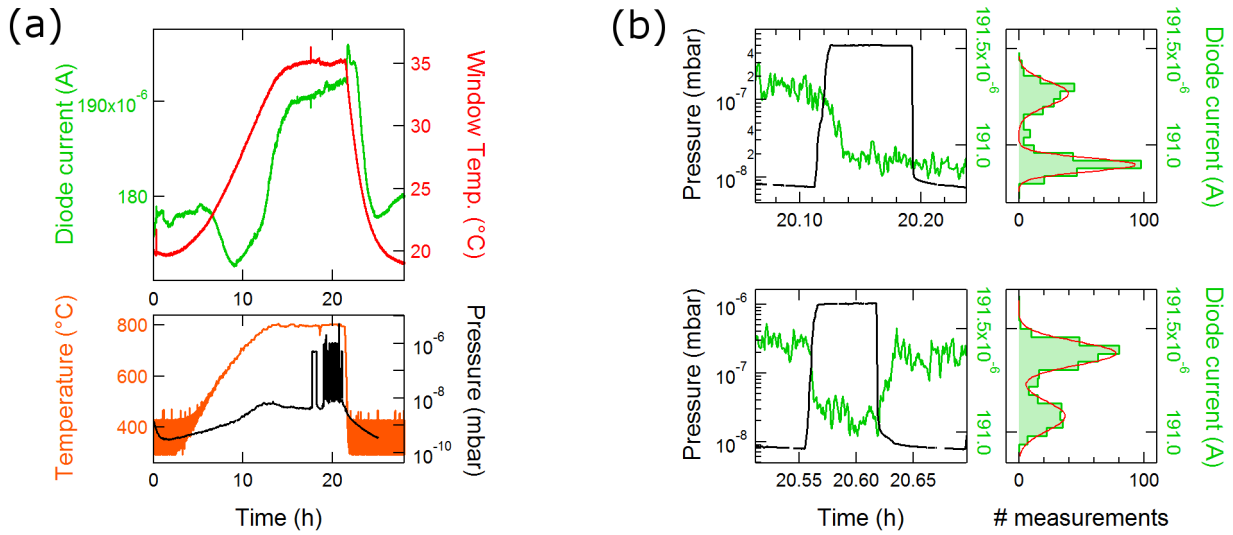

Figure 18: Optical detection of a rhodium surface oxidation and the single boron nitride layer growth. The data in (a) display the experimental conditions for a boron nitride preparation on a rhodium(111) thin film sample. Upper part: The normalized diode signal (**green**) evolution measured at the most sensitive optical configuration as introduced in Figure 17. Lower part: The sample was exposed to a slow heating ramp of 10 h to reach the preparation temperature of about 800 °C (**orange**). It was kept at that temperature for another 8 h to stabilize thermal effects on the optical measurement system. The oxygen cleaning and borazine dosing procedure started after 18 hours, which are visible in the pressure spikes (**black**). The drift of the optical recordings between 15 – 21 h appeared to be linear, which was subtracted as background for a more detailed analysis in (b). (b) displays the details of a borazine dosing event in the upper part after 20.12 h. The resulting boron nitride layer is removed by subsequent oxygen dosing in order to reproduce the signal findings. The lower part shows the details of O_2 dosing after 20.55 h. The oxygen exposure induces a reversible signal change, while the borazine dosing does not. Statistical evaluation of the diode measurements and the sensitivity determined in Figure 17 indicates an optical signal shift $\Delta_{\Psi\text{and}\Delta} = 6.34(14) \cdot 10^{-2}$ ° for the borazine event and $\Delta_{\Psi\text{and}\Delta} = 5.14(14) \cdot 10^{-2}$ ° for the oxygen event. The Gaussian distributions have an optical width of $\text{FWHM}_{\Psi\text{and}\Delta} = 2.2(6) \cdot 10^{-2}$ °.

with an external TTL rather than a software trigger and the current measurement units might also be exchanged by more powerful equipment. Additionally, The polarizing Glan-Taylor beam splitter can not match the extinction ratio of modern thin film polarizers and induces multiple diffraction spots, which could be avoided with a non-polarizing beam splitter.

3.3 Photoelectron Yield Approach, Ultraviolet Flash Lamp

This approach is based on the photoelectric effect, where incoming photons promote electron emission. The non polarized excitation light and an electron measurement via a current make the system more robust against viewport effects than the optical approach in the previous section. This section shows that the photoelectron yield approach is an order of magnitude more sensitive to a surface reaction than the optical setup. However, electron emission is pressure dependent at pressures, above which the electron mean free path is shorter than the sample-chamber wall distance. An assessment of the pressure limit can be found in the appendix section 7.3.2. The findings presented in this chapter 3.3 are complementary to the ones found in reference [3].

3.3.1 Setup and Photocurrent Yield Principle

The photoelectron yield setup, its light pulse, stability and current signals are displayed in Figure 19. The setup is schematically drawn in Figure 19(a). A broad band pulsed xenon flash lamp, which emits radiation between 220 - 750 nm (PX-2, Ocean Optics, USA), is focused onto a sample in UHV, where it promotes electron emission from the surface. The resulting photocurrent is in the order of μA/pulse and may be directly measured as sample current. Preferably, the sample current is collected by a biased electrode. This lowers signal intensity, but provides a universal system, which is applicable to the Sinergia as well as the ESCA preparation chamber. Furthermore, it avoids the tedious sample current measurement in ESCA, where it requires the thermocouple to be detached from the sample. The photocurrent is recorded with an oscilloscope, which is synchronized with the light pulses by the same trigger.
The ultraviolet (UV) light pulse is shown in Figure 19(c). The supplier Ocean Optics defines a pulse length of 5 μs, which is used for all following calculations. The stability of the light flashes is estimated in Figure 19(d), where the integral of the diode signal has been recorded for different time intervals. For a short preparation event of about 9 mins, the relative FWHM is in the order of 0.85 %.
The oscilloscope, the BNC cables and the sample-collector system form an RC circuit, which determines the shape of the current response. The circuit consists of the oscilloscopes 1 MΩ resistance, its 20 pF capacitance, the capacitance of the BNC cables (in the order of 100 pF) and an unknown sample to antenna capacitance. Figure 19(b) displays the antenna and sample current as measured by the oscilloscope. Here, the exponential decay constant τ is 315 μs. It is advantages to keep the decay constant as short as possible, i.e., using short cables. This increases the signal amplitude and reduces the τ induced error. Equation (15) defines the photocurrent I_{ph} per ultraviolet pulse, which is the time integral of the voltage signal as measured by the oscilloscope.

$$I_{ph} = \frac{1}{R \cdot \tau_{pulse}} \int_0^\infty A \cdot e^{-\frac{t}{\tau}} dt = \frac{A \cdot \tau}{R \cdot \tau_{pulse}} \tag{15}$$

Here, τ_{pulse} is the the UV pulse length, R the oscilloscope resistance, A the signal amplitude and τ

the current decay constant. During a preparation, only the signal amplitude A will change, which is directly proportional to the photocurrent I_{ph} as shown in equation (15). For a maximized signal-to-noise ratio, one might only consider the voltage amplitude A. Although A has less physical meaning than a photocurrent, it is not influenced by the noise of the current decay τ as in the case for I_{ph} in equation (15).

The pulsed nature of the excitation is a necessary requirement for the surface monitoring during a CVD process. On one hand, most CVD experiments need a hot surface, which might promote thermionic emission from the surface. On the other hand, most reactive gases introduced into the chamber induce additional charges. With a pulsed excitation, the surface photocurrent can easily be distinguished from thermionic emission or ion currents, because these appear as continuous background currents. These continuous currents may carry additional information about the

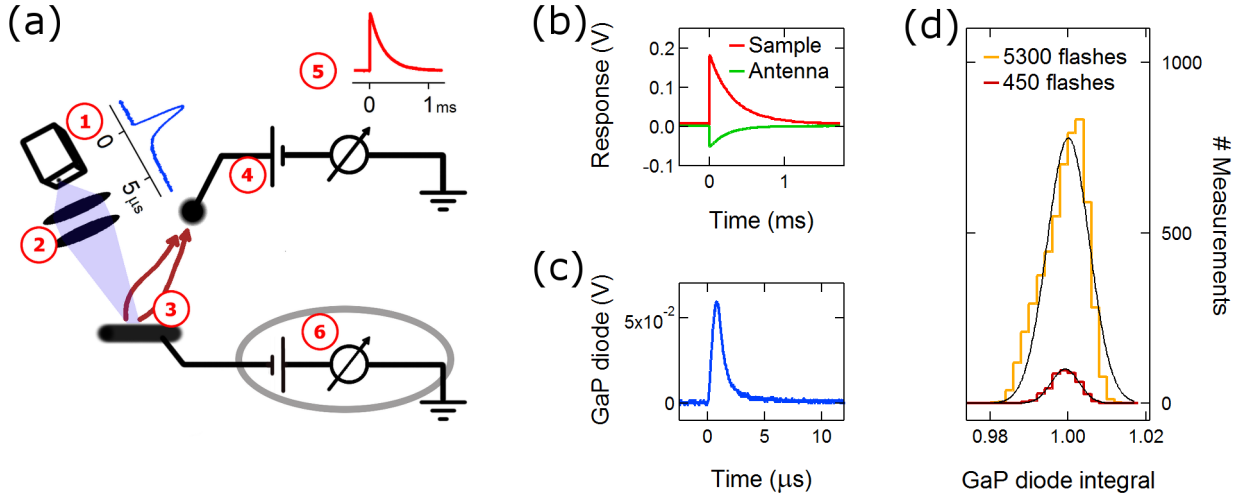

Figure 19: The photoelectron yield setup, its light source stability and current response. (a) displays a schematic overview of the setup. The Xe flash lamp generates UV light pulses (1), which are focused via fused silica lenses (2) and introduced into the UHV chamber through a sapphire view port. On the sample, the light excites photoelectrons (3), which are collected with a biased aluminum electrode (4). The current measurement is achieved over the 1 MΩ resistance of an oscilloscope (5). Alternatively, the sample current may also be recorded (6), which for the ESCA case requires the thermocouple to be detached from the sample. (b) shows the sample and antenna current signals of 16 averaged UV flashes with a sample bias of -8.5 V and +34 V antenna bias, respectively. In this configuration, the Al electrode is capable of collecting about 1/3 of the sample current. (c) displays a single UV flash as recorded by a GaP diode, which had been short circuit via a 50 Ω resistor. In order to assess the stability of the UV flashes, the volume integral of such signals had been evaluated and their histograms are displayed in (d). For a 1.5 h measurement and more than 5300 flashes, the FWHM of the integral histogram is 1.28 %. For such a long measurement, the flash integral drifts towards larger values, which is reflected in the asymmetric distribution. For a 9 min measurement and 450 flashes, the flash integrals follow a Gaussian statistics and the FWHM is only 0.85 %. (a) from Ref. [3].

sample or reaction. It turns out that, e.g., a running mass spectrometer filament does change the reactive gas in the UHV chamber and a more detailed description of this issue is addressed in the appendix in section 7.3.

The rather intuitive relation between work function and photocurrent can be verified by a work function increase (e.g., with oxidation of Rh), which reduces the photocurrent, and vice versa (e.g., with borazine). It is not possible to absolutely measure a work function, but its variation during a process. Nevertheless, close inspection of the UV lamp spectrum and the photoemission process on the surface extend the information of the qualitative photocurrent yield changes and are discussed below.

Figure 20(a) displays an ambient light subtracted flash lamp spectrum and its integral (Ocean Optics spectrometer, USB2000+). The integral reveals a limitation of the setup, 99.6% of all radiation occurs in an energy window below 5.6 eV, which makes the measurement system unfeasible for surfaces with work functions above this energy. For the nanomesh preparation, the work function of rhodium is formally lowered from 4.98 eV of polycrystalline Rh [36] to 4.15 eV of *h*-BN/Rh [5], both of which are within the UV lamp energy window. Normal emission UPS measurements of the clean rhodium(111) surface prior to the preparation revealed an initial work function of 5.66 eV [3], which is the detection limit of the photocurrent yield setup.

To elucidate the photoemission process, we follow a three step model. It includes electron excitation, transport to the surface and emission to vacuum [37]. The first step is an excitation from an initial state to a final state, which is determined by their respective density of states and an excitation cross section. The second step involves the electron transport to the surface, which occurs if the electron has a positive momentum in the direction of the surface normal $\mathrm{k}_\perp$. During this transport, scattering might happen, leading to energy and momentum dissipation, which results in secondary electrons. The third step is the emission of the electron into vacuum, which is restricted to electrons with a large enough momentum perpendicular to the surface $k_\perp$. This momentum has to satisfy the condition (16), where E_{vacuum} is the vacuum energy level and E_0 is the inner crystal potential (the valence band bottom), which is in the order of 10 - 20 eV.

$$\hbar^2 k_\perp^2/(2m) \geq E_{vacuum} - E_0 \tag{16}$$

$$k_\perp = \frac{1}{\hbar}\sqrt{2m(E_m + E_0)}\cos(\theta) \tag{17}$$

$$P_{trans} = \frac{2\pi r^2}{4\pi r^2}(1 - \cos(\theta)) = \frac{1}{2}(1 - \sqrt{\frac{E_0}{E_m + E_0}}) \tag{18}$$

Equation (17) defines the electron momentum component perpendicular to the surface $k_\perp$. It is derived from the free electron dispersion and m is the electron mass, E_m is the measured electron energy in vacuum and θ is the polar angle between surface normal and electron momentum vector in the solid. Equations (16) and (17) define the maximal solid angle θ_{max} at which an isotropic emitter could still transmit electrons into vacuum. The isotropic transmission probability is given in equation (18), which compares the spherical surface at angles smaller than θ_{max} to the surface of an emission sphere.

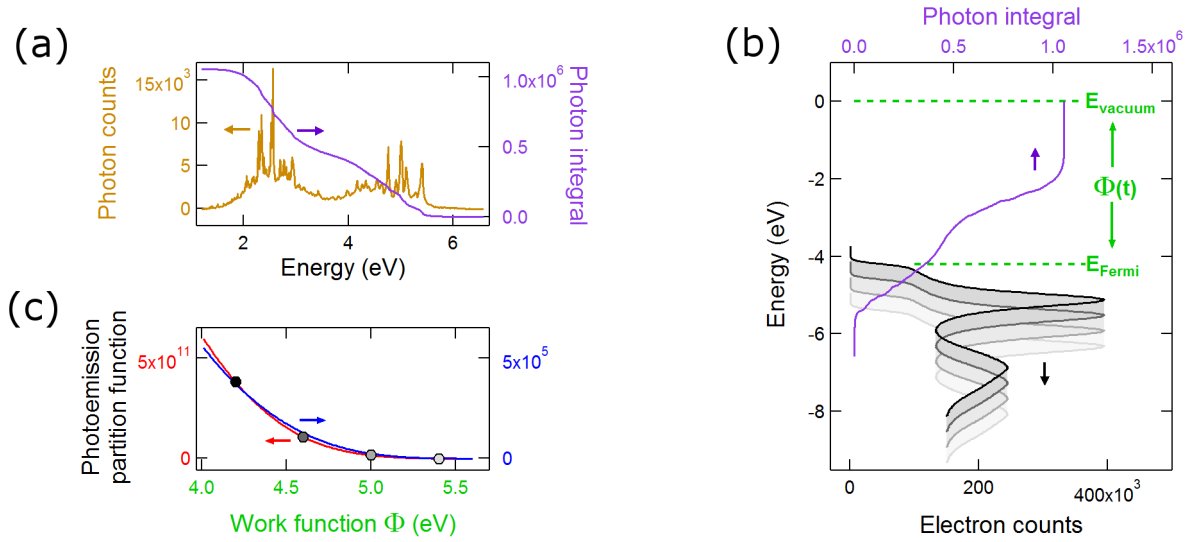

Figure 20: The mechanism of the photocurrent in- and decrease, respectively. (a) displays the broad photon emission spectrum of the Ocean Optics PX-2 Xe flash lamp. The photon counts have been integrated from the largest to the lowest energy and only 0.4 % of all photons appear above 5.6 eV. (b) Visualizes an energy diagram for photoemission during the BN preparation on Rh(111). In this process, the work function of the substrate ($\Phi(t)$) is reduced, which is sketched as elevation of the normal emission UPS bands of Rh towards the vacuum energy level E_{vacuum} (from **grey** to **black**). The photon count integral is drawn in the same energy diagram, but with a reversed energy axis. Such presentation illustrates that only a small part of the UV lamp spectrum is capable of photoemission, namely, where the photon integral and the Rh bands overlap and are non zero. (c) is the sum of all possible photoexcitation events as derived for different work functions. The **blue line** is a calculation with a Heaviside function as electron density of states (DOS), while the **red line** approximates a more realistic electron DOS with the normal emission UPS data shown in (b). The black to gray dots mark the calculations for the four work function situations shown in (b).

With the above consideration from the photoemission process, it is possible to estimate an electron emission change, which is based on a work function change. Figure 20(b) sketches the situation in an energy diagram, with the UV lamp photon integral at a fixed energy and the shifting rhodium states with their time dependent work function $\Phi(t)$. Normal emission He Iα UPS data provide an estimation for the electron density of states (DOS). For the general situation of an unknown electron DOS, the following calculation were also performed with a Heaviside function.

The first step of electron excitation by light is determined by a photoemission cross section σ. The emitter density, photon flux or excitation area are not changing during an experiment and can therefore be neglected. Due to the low light source energy, only photons with the highest energy may excite photoelectrons and the emitting states are restricted to be close to the Fermi energy E_{Fermi}. For the boron nitride preparation on rhodium(111), only photons between 4.2 and 5.6 eV can excite states, which are maximal 1.5 eV below E_{Fermi}. Because of this narrow light and state

window, we assume that the photoemission cross section is constant. The second step of electron transport to the surface is governed by scattering and energy loss, which means only parts of the electrons may reach the surface. This is the reason for the surface sensitivity of photoelectron spectroscopy and the electron yield method described here. In good approximation, this electron transport step is treated as constant attenuation, because an atomic monolayer preparation does not change the emission matrix drastically. The third step of electron transmission through the surface into vacuum is approximated by the emission of an isotropic emitter in equation (18).
The above estimations allow the definition of a photoemission partition function $Q_{emission}$. It is defined in equation (19) and it is the sum of all photoemission capable states at a given work function. This sum does neither include excitation cross sections changes nor final state effects. From a photoemission perspective it corresponds to the sum of all matrix elements with the unity operator as interaction Hamiltonian and as final state wave function. However, the initial state is restricted in momentum and energy. From a statistical thermodynamics point of view, this sum corresponds to the sum of all possible microstates in a microcanonical ensemble. Here, one microstate is a state, in which one electron is excited above E_{vacuum} into a state, which can pass into vacuum in the third step.

$$Q_{emission}(\phi) = \int_{-\infty}^{E_F} DOS(E) \int_{-\infty}^{E} \#photons(\epsilon) \cdot \frac{1}{2} \left(1 - \sqrt{\frac{E_0}{E_m(\epsilon, E, \phi) + E_0}} \right) d\epsilon dE \tag{19}$$

As depicted in Figure 20(b), the energy scale refers to E_{vacuum} as zero level, which is the reason why the integrals in equation (19) start at negative values. The $\#photons$ are the number of photons with an energy ϵ as shown in the spectrum in Figure 20(a). The density of states (DOS) is approximated by the normal emission UPS spectrum of Rh in one and a Heaviside function in the other case. Figure 20(c) displays the photoemission partition functions $Q_{emission}$ for these two DOS and an assumed inner potential E_0 of 20 eV. Despite numerous assumptions, it yields an estimate of a photoemission probability. Its course indicates an increased sensitivity towards surfaces with lower work functions. Such a behavior is expected from the photon count integral in Figure 20(a), where a lower work function allows more photons to probe the surface. To estimate a work function change during a preparations these calculated photoemission probabilities can be fitted as long as the initial and final work functions were determined. For the general case of a Heaviside electron DOS, a third order polynomial is given in equation 20.

$$I_{ph}(\Phi) \propto -1 \cdot \Phi + 1.807 \cdot 10^{-1} \cdot \Phi^2 - 1.088 \cdot 10^{-2} \cdot \Phi^3 \tag{20}$$

In summary, the photoelectron yield setup is introduced and its function discussed. The photoemission three-step model is reviewed in order to derive an expression, which relates a measured photocurrent change to a work function change. This allows to estimate the sensitivity of the system at a given work function or to estimate a photocurrent change in terms of a work function shift.

3.3.2 Performance in the ESCA and Sinergia UHV Chamber

The setup described in the previous section 3.3.1 had been used for numerous experiments in the ESCA preparation chamber. The main differences to the Sinergia UHV chamber are the non-shielded filament power cables to the sample, the vicinity of the reflected UV beam to the collector electrode and the electrical sample connections, which in ESCA allow sample current measurements as depicted in Figure 19(a).

The non-shielded filament power lines to the sample change the magnetic and electrical fields in the chamber upon heating and may distort the photocurrent measurement. Therefore, the sample filament voltage is separated in time from the UV flash events. Figure 21(a) displays an electronic scheme of the trigger box, which induces a trigger delay, and the relay box, which is used to turn the heating filament on and off. The corresponding triggers are visualized in Figure 21(b). Filament heating is active in the red marked area "Out S". The trigger "In" switches the sample filament to ground, while the "Out L" triggers a UV flash at a slightly delayed time.

The sourcing trigger is the "count inhibit" of the demagnetization heating power supply of F. Bourgui (University of Fribourg). It is a 10 Hz trigger with a variable pulse width between 10 – 20 ms. The count inhibit is directly used to power the sample filament switching relay and has a connection to the trigger box. The trigger box delays the incoming pulses by smoothing with a 470 Ω resistor and a 200 nF capacity and feeding it to a Schmitt trigger (74HCT14). To fine tune the delay a variable resistor is implemented. In a common ESCA experiment, a heating duty cycle of 90 % is chosen at the demagnetization power supply, the lamp trigger is delayed by 5 ms, the sample is grounded and only the collector current is measured. For daily usage, it is not recommended to perform sample current measurements due to serious efforts for shielding the sample cables and the fact that it excludes thermocouple measurements at the sample head.

The reflectance of Rhodium at wavelengths between 220 - 300 nm (5.6 - 4.1 eV) is for normal incidence between 57 – 72 %. It can be calculated with equations (3), (4), (10) and the refractive index data from the handbook of optical constants [33]. This shows that the largest part of the light is reflected at the Rh surface and may promote photoemission somewhere else in the UHV chamber, which would falsify the photocurrent yield signal from the surface. In the case of the ESCA geometry, the UV light is reflected onto the head of the hot dosing device (HDD), also known as the atomic hydrogen source. The effects of such reflected light can be assessed by comparison of the collector and sample current during the same CVD process. Figure 21(c) displays such a measurement for the boron nitride preparation on a Rh thin film. The sample and collector bias was 8.4 V each, which results in a collector to sample current ratio of about 1:10. The linear relation between the measured currents prove the equivalence of the collector and sample measuring scheme. The significant collector offset of about $1.5 \cdot 10^{-7}$ A is assigned to a photocurrent from the reflected UV beam. Although the collector current only shows a constant offset due to the reflected UV beam, this may not be true for other preparations, e.g. when operating the HDD or when applying a precursor, which also reacts with the cold HDD.

Figure 22 displays the collector current signals for a boron nitride preparation on Rh(111) in

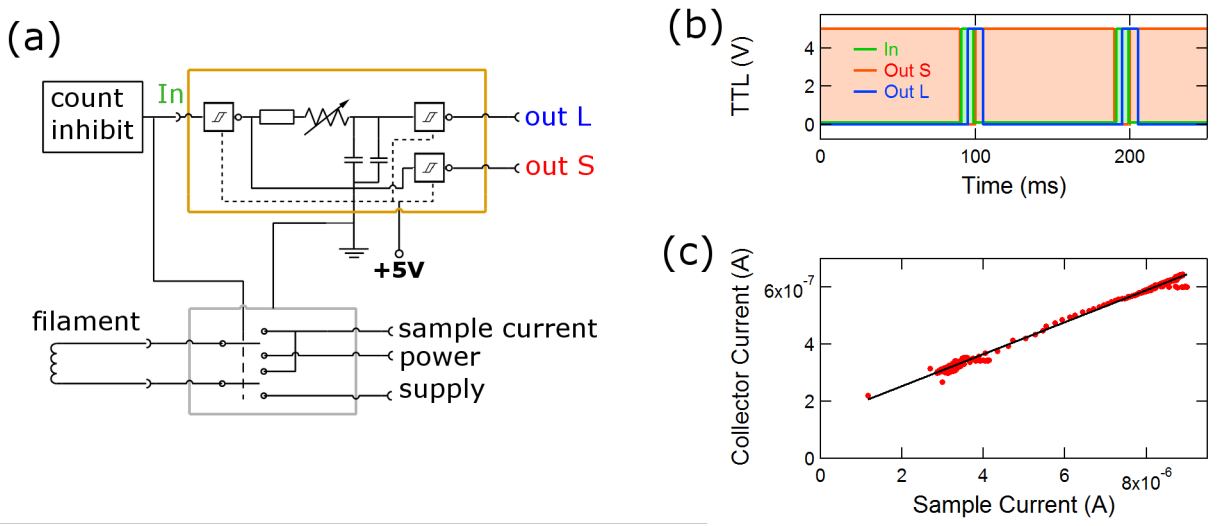

Figure 21: Trigger concept and electronic scheme for simultaneous sample and collector current measurements. (a) displays the electronic scheme of the trigger and relay box. The sourcing trigger is the count inhibit out of the demagnetization power supply, which allows heating duty cycles between 80 – 90 %. The **yellow square** is the interior of the small trigger box, which consists of a hex inverting Schmitt trigger and a RC delaying circuit. The **gray square** is the relay box, which switches the sample between "power supply" and the single ended "sample current" line. The three different TTL triggers are displayed in (b), the **In** trigger is a 10 Hz trigger with a variable width between 10 - 20 ms. **Out L** is the delayed trigger for the UV flash lamp and the Oscilloscope. **Out S** is the inverted **In**, which formerly had been used to switch the relay. (c) is the photocurrent as measured by the collector versus the sample photocurrent during the same BN preparation on Rh(111). The apparent linear relation confirms the equivalence of both measuring circuits. The y-axis current offset is explained by photoelectrons, which were excited by the reflected UV beam somewhere else in the UHV chamber.

ESCA and in Sinergia. The preparation in ESCA consists of a single annealing cycle with the application of $5 \cdot 10^{-7}$ mbar borazine for about 6.8 minutes. The preparation in Sinergia basis on the procedure for nanomesh growth on epitaxial films without sputtering [20] and its modifications introduced in section 2.4.2. Such a preparation requires the complete oxidation of the rhodium thin film, without which carbon might not be completely removed from the sample. Therefore, the Sinergia preparation is about 4.5 h long and consists of four times oxygen and one time borazine dosing. Furthermore, the ESCA procedure allowed temperature control with a thermocouple, while the Sinergia chamber is only equipped with pyrometers, which cannot read temperatures below 350 °C.

ESCA also allows to measure the sample work function prior and subsequent to the preparation, which is indicated in Figure 22(a). With these two measurement points and the assumption that $\Delta I_{ph} \propto -\Delta\Phi$, the current noise of 0.43 % translates into a work function sensitivity of ±11 meV [3]. This current noise is lower than the noise from the light pulse, because the current

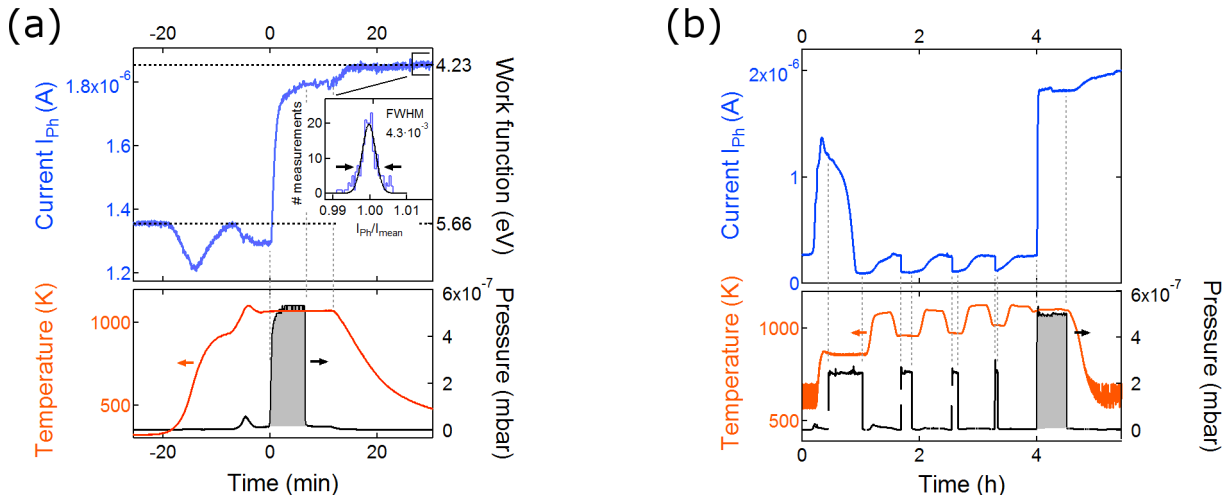

Figure 22: Single layer hexagonal boron nitride preparation on Rh(111) as recorded by the photocurrent yield setup. The measurements of an *h*-BN formation are shown in (a) for an ESCA and in (b) for a Sinergia preparation. The top parts display the photocurrent I_{ph}, while the lower parts show the experimental conditions with pressure and temperature. The gray pressure spikes to $5 \cdot 10^{-7}$ mbar are the borazine dosing events and all the dotted lines are guides for easy reading. The inset in the top part of (a) displays the photocurrent statistics of the last 200 measurement points. (a) from Ref. [3].

is recorded as average of 16 light flashes. The more rigorous treatment introduced in section 3.3.1 reveals a work function dependent sensitivity. Evaluation of equation (20) yields for a work function of 4.23 eV a sensitivity of ±6.8 meV.

The data in Figure 22 demonstrate the surface monitoring capabilities of the pulsed UV light source. Not only the borazine dosing event (gray pressure spike) is successfully recorded with a current increase, but also oxidation events are observed as current decrease. Although, it is not possible to directly access a physical property such as the work function, the setup provides an inexpensive means to in-situ measure changes and differences on a surface well below the atomic monolayer regime. In this sense, it is superior to indirect measurements of the gas composition with a mass spectrometer, because every signal can directly be traced back to the surface. Therefore, it is the most important tool for process monitoring in the Sinergia chamber, because there is little or no characterization instrumentation available prior to wafer cutting and a cut wafer cannot be re-prepared in Sinergia anymore.

3.3.3 Potential Application for Reversible Adsorption Processes

The UV flash lamp setup has been used for monitoring a variety of processes, among which was an investigation of the pentanone sticking on *h*-BN/Rh(111). The goal was to support graphene preparation activities on the *h*-BN nanomesh [22]. Preparation conditions as optimized for the *h*-BN/Cu(111) system [38] were not successful for the *h*-BN/Rh(111) substrate.

The UV lamp setup could not be directly employed to monitor graphene layer growth, because the applied pentanone pressures were in the millibar regime [38]. Such conditions are about four orders of magnitude above a pressure independent photocurrent measurement and may indicate that the graphene growth mechanism requires on a small precursor mean free path in the reaction chamber. In this sense, the choice of substrate should only play a minor role.

Here, we estimate a pentanone desorption energy and calculate coverages at low pressures. Such parameters are crucial to understand and further optimize preparation conditions. The data acquired are displayed in Figure 23. They show the photocurrent amplitude at different temperatures and pressures. The current amplitude has the advantage of being proportional to the photocurrent I_{ph}, but with less noise, as shown in equation (15). As the experiment was one of the earliest UV lamp experiments, it lacks of several later improvements and still relied on an analog pressure reading, which leads to a rather rough pressure value grid. Also, the oscilloscope trigger activated some current measurements out of flash synchronization, which led to current amplitude spikes.

For a thorough analysis, the Langmuir isotherm has to be recalled. Equations (21) and (22) are the first order reaction rates for adsorption and desorption from a surface, respectively. They indicate that the adsorption process is proportional to the pressure and the empty sites $(1-\theta)$ with a proportionality constant k, while the desorption process is proportional to the coverage (θ) with a constant k'.

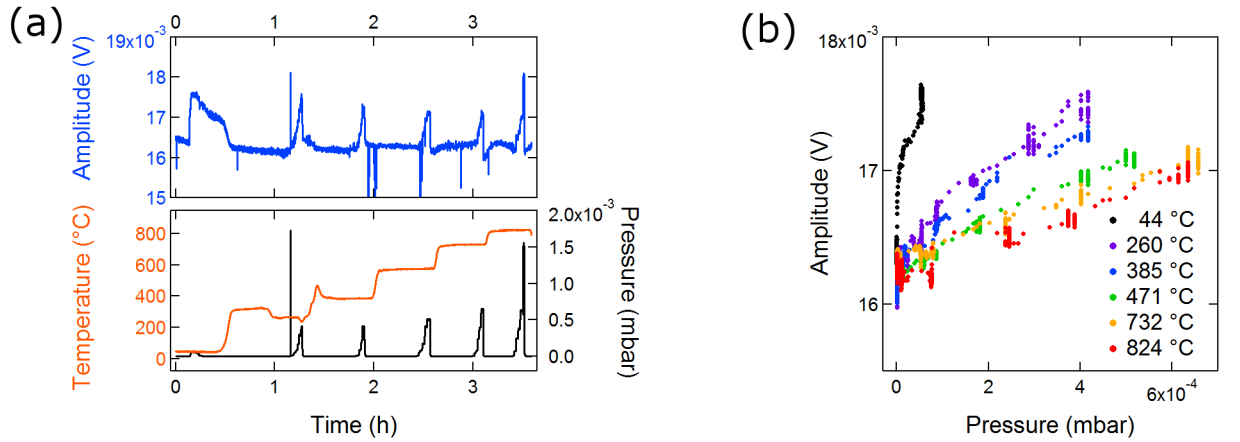

Figure 23: Photoelectron yield data from the adsorption of pentanone on the h-BN nanomesh. (a) the upper part displays the UV flash lamp amplitude for a series of pentanone pressures at different temperatures. The trigger protocol was not properly adjusted, which led to the negative amplitude spikes, which can be ignored for the evaluations here. The temperature and pressure conditions are shown in the lower part. (b) summarizes the data as current amplitudes for different pressures at different temperatures. Data for pressures in the 10^{-3} mbar range are ignored, due pressure induced signal decrease.

$$\frac{\partial\theta}{\partial t} = k \cdot p \cdot (1-\theta) \tag{21}$$

$$-\frac{\partial\theta}{\partial t} = k'\theta \tag{22}$$

In equilibrium the adsorption and the desorption process are equally fast and from equations (21) and (22), one can derive the Langmuir isotherm. It is given in equation (23). Experimentally, neither k nor k' are directly accessible. However, the pressure dependence of the coverage may be detected by pressure dependent experiments. Equation (24) is the pressure derivative of the Langmuir isotherm. At very low pressures, this dependence is linear and expression (24) can be simplified to $\frac{k}{k'}$. Accordingly, equation (25) is only valid for low coverages.

$$\theta = \frac{k \cdot p}{k' + k \cdot p} \tag{23}$$

$$\frac{\partial\theta}{\partial p} = \frac{k \cdot k'}{k^2p^2 + 2kk'p + k'^2} \cong \frac{k}{k'} \tag{24}$$

$$d\theta = \frac{k}{k'}dp \tag{25}$$

In order to determine $\frac{k}{k'}$, equilibrium measurements of θ at a pressure p are sufficient. The fundamental assumption for the following treatment is that the coverage θ is proportional to the photoelectron yield I_{ph} and it is given in equation (26).

$$d\theta \propto dI_{ph} \tag{26}$$

As visible in Figure 23, the photocurrent is enhanced at elevated pentanone pressures. The energy of the UV light cannot promote photoemission from the pentanone molecules [39], which means, the rise in photocurrent is caused by pentanone molecules interacting with the sample surface. The linear assumption in equation (26) is the simplest model, which meets the requirement that the more molecules interact with the surface, the larger the UV photocurrent yield. A linear coverage-photocurrent relationship is restricted to low coverages, where the 3D island growth or the growth of thick layers is excluded. Such 3D layers might completely destroy a simple coverage-photocurrent relationship, as observed for thick BN layers. Equation (26) can be expressed in terms of the photocurrent yield amplitude $A(p,T)$ with the help of equation (15). This relation and its pressure derivative are given with a proportionality constant B in equations (27) and (28). Note that $m(T)$ is the photocurrent yield slope in the pressure direction and independent of the pressure itself.

$$d\theta(p,T) = B \cdot dA(p,T) \tag{27}$$

$$\frac{\partial\theta(p,T)}{\partial p} = \frac{k}{k'} = B \cdot \frac{\partial A(p,T)}{\partial p} = B \cdot m(T) \tag{28}$$

The data in Figure 23(b) provide enough information to determine $m(T)$ in equation (28) at six different temperatures. While B has to be constant for the same system, $m(T)$ clearly decreases with increasing temperature. Considering the adsorption process, it should not be temperature dependent, since the impinging molecules don't know the substrate temperature. On the other hand, the desorption process is temperature dependent and the rate constant k' can be expressed in the Arrhenius equation (29). The k_0 denotes a proportionality constant, E_d the desorption energy, k_B the Boltzmann constant and T the absolute temperature.

$$k' = k_0 \cdot e^{-\frac{E_d}{k_B T}} \tag{29}$$

$$= \frac{k}{B \cdot m(T)} \tag{30}$$

Equation (30) is derived from the linear assumption derivative in equation (28) and helps keeping track of the mathematical route to arrive at the Arrhenius plot expression in equation (31).

$$\ln\left(\frac{1}{m(T)}\right) = \ln\left(\frac{k_0 \cdot B}{k}\right) - \frac{E_d}{k_B} \cdot T^{-1} \tag{31}$$

Evaluation of equation (31) at different temperatures leads to the Arrhenius plot in Figure 24(a) and the desorption energy determination for pentanone on the boron nitride nanomesh. Note that the data at room temperature was omitted for this evaluation, because pentanone does not reversibly stick to the substrate at this temperature, which is visible in a non-reversible photocurrent change in Figure 23(a). This data is therefore obsolete for a desorption parameter determination, because this desorption is so slow that it appears not to occur.
In addition to the desorption energy, the Langmuir equation (23) can be solved with the linear assumption in equation (27) as shown in expression in (32). A further simplification is gained by application of equation (28), which leads to equation (33).

$$\theta(p,T) = \frac{\frac{k}{k'}p}{1 + \frac{k}{k'}p} = B \cdot A(p,t) \tag{32}$$

$$A(p,t) = \frac{\frac{k}{B \cdot k'}p}{1 + \frac{k}{k'}p} = \frac{m(T)p}{1 + \frac{k}{k'}p} \tag{33}$$

The unknown parameter left in equation (33) is $\frac{k}{k'}$ and this ratio can be determined for each input temperature. With the knowledge of this final parameter, one could calculate the proportionality constant B or simply solve the Langmuir equation (23). Figure 24(b) displays the calculated pentanone coverage on the h-BN nanomesh. For this surface system, it would be possible to verify this calculations by XPS measurements of the room temperature deposited layer.
For the application of the procedure introduced in this section, all assumptions are to be checked carefully. Firstly, the Langmuir isotherm might not be the proper model for a surface adsorption reaction, especially not for an island growth mode. Furthermore, the low coverage assumption may be misleading or the UV lamp may not be sensitive enough for a particular adsorption reaction.

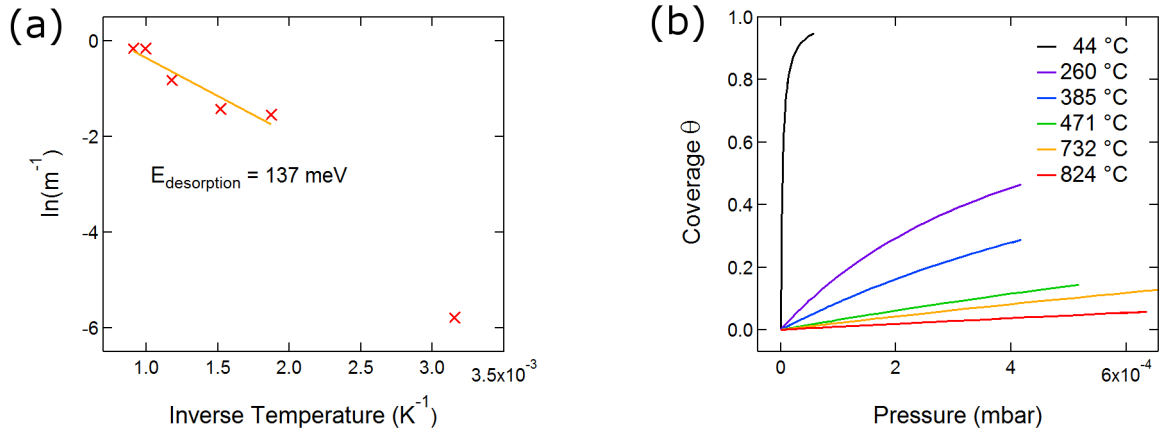

Figure 24: Determination of a desorption energy and coverage for pentanone on the *h*-BN nanomesh. (a) Arrhenius plot of equation (31) for the desorption energy determination of pentanone on the *h*-BN nanomesh. The energy is 137 ± 25 meV and the data point at room temperature had not been considered, because desorption is not observed to occur a that temperature. (b) displays the coverages from the data in Figure 23(c), which were calculated within the Langmuir isotherm frame.

Here, we can state that the graphene growth on the nanomesh with the pentanone precursor is particularly difficult, because pentanone or its fragments do not stick to the *h*-BN/Rh(111) surface. At a preparation temperature of 824 °C the coverage may not succeed 6 % in the 10^{-4} mbar pentanone range. This information reveals the necessity of even higher pressure (mbar range) experiments, where reaction gas pressure compensates the low sticking coefficient or the gas phase-hot sample system meets a chemical reaction condition for a graphene like coating regardless of the precursor sticking to surface.

3.3.4 Conclusion and Outlook

Photoelectron yield measurements are a method for in-situ process monitoring with submonolayer sensitivity. The proposed setup is inexpensive, simple to install and fast to be adapted to any UHV preparation chamber.
Its application to a UHV CVD process is published [3], but it offers much more characterization capabilities. In combination with a mass spectrometer, it may help identify element specific surface reactions, which is shown for a carbon oxygen substitution in section 2.4.2. Or, it could be used to determine desorption energies or surface coverages, which is performed in section 3.3.3.
Because of its simplicity and variety of applications, an additional UV flash lamp had been purchased at the end of 2013. It is intended to be used as a surface preparation monitoring system as originally proposed [3]. A second flash lamp could in principle also be used in the Sinergia chamber, where the two flashes excite two different spots on the wafer at different times. Such an experiment could reveal the evolution of a reaction across a 4 inch wafer, i.e. along a temperature gradient. Triggers, data recording system and electrode are readily installed.

4 Thick Boron Nitride Layers

4.1 Motivation for Thick Boron Nitride Layers

The single layer of *h*-BN on a metal substrate cannot directly be used as basis for electronic devices, because the *h*-BN to substrate interaction strongly influences the properties of the boron nitride layer. Graphene based devices with *h*-BN substrates employ several nanometer thick boron nitride sheets [40] or undefined thick sheets on SiO_2 [41]. Alternative applications, such as a far-ultraviolet fluorescent material requires thick boron nitride crystallites as well [42].
The Sinergia chamber was designed for large substrates with the goal to use these substrates as basis for devices. Thus, the *h*-BN/Rh(111) system has to be further modified or processed in order to be used as device basis. Three different strategies might lead there: Firstly, the invention of a device, which can use the *h*-BN/Rh(111) system as basis. One possible setup is explored in reference [17]. Secondly, the removal of the BN layer and its deposition on an arbitrary substrate, which is addressed in section 5. Thirdly, it may be possible to directly grow thick *h*-BN layers, which is introduced in this chapter.
The feasibility of CVD growth of thick boron nitride layers within the UHV chambers of the Osterwalder group has been demonstrated by S. Roth in late 2012 [22]. The procedure was reproduced in early 2013 and the layer growth has been recorded by the newly established UV lamp photocurrent yield setup (see section 3.3). Here, we review the formation conditions of crystalline *h*-BN, the concepts of its CVD growth and provide experimental evidence for thick BN films.

4.2 Introduction to Thick Hexagonal Boron Nitride CVD

CVD of *h*-BN in UHV chambers is a self-terminating process up to the atomic single layer [25,43–45]. This is in contrast to preparation conditions in vacuum furnaces in the millibar regime, which leads to the deposition of thick films [46–48]. Equivalent observations are also true for graphene and thin graphite layers [49]. These findings imply that it is the pressure, which determines the single or thick layer growth. Indeed, the pressure appears to influence the growth regime as suggested in reference [48], but it is not the only parameter to e.g. determine the ordering of a film.
CVD growth of thick *h*-BN films is known since 40 years with the precursor system BCl_3-NH_3-H_2 [46, 50]. These early films clearly show turbostratic ordering. That is, the *h*-BN layers are not ordered in z-direction, which is similar to the structure found for pyrolytic graphite. The transition temperature to form *h*-BN from such turbostratic BN (*t*-BN) starts at 1450 °C and shows reasonably ordered *h*-BN films at 1800 °C [51]. This process is in full analogy to the transformation of pyrolytic graphite to graphite. The transition temperature from *t*-BN to *h*-BN might be lower (1700 °C) and at low pressures, as indicated in the temperature - pressure diagram of Matsuda *et al.* [50].
A more recent approach with the precursor borazine, where the B:N ratio is 1:1, is discussed

in [52]. Different experimental parameters were tested for best BN layer growth. A substrate temperature of 550 °C and a helium background pressure of 2.6 mbar led to BN films with a B:N ratio of about 6:4. Addition of a radio frequency plasma and exchanging He with 0.13 mbar Ar including traces of hydrogen produced the best films, with suppression of B-H and N-H species and a B:N ratio of 1:1. However, a turbostratic morphology analysis is missing [52].
In the field of thick *h*-BN layers on metal surfaces, the turbostratic nature of those films is generally ignored and little data show its true crystallinity. Nevertheless, the community calls the thick films "*h*-BN", which means they consist of *h*-BN flakes rather than single crystalline *h*-BN. However, from a crystallographic point of view, it is not correct, because *t*-BN is clearly distinguished from an *h*-BN crystal. For instance, electron diffraction patterns placed with the careful implication of a pattern from the single layer cannot prove the single crystallinity of the thick film [48]. A careful XRD analysis for thick films was performed by Kubota *et al.*, where powder spectra of the films and not the film itself were measured [53].

4.2.1 High Borazine Pressure Experiments

In this section, the second high borazine pressure experiment with a Cu(111) single crystal is reviewed. A small part of the data are already shown by Roth [22], but important conclusions were not yet drawn. One relevant finding is that high borazine pressure experiments (above 0.2 mbar) are not an option for the standard ESCA instrumentation, because the pressure detector head (PBR 260, Pfeiffer, Germany) was no longer continuously working or even broke after these borazine exposures.
Figures 25(a) and (b) display Al Kα XPS, He IIα normal emission UPS and LEED data of the pristine Cu(111) crystal, after the single layer and after the thick BN preparation. As shown in the LEED of the single layer, the *h*-BN induces a dominant ring structure, which is not present in a high quality preparation in ESCA as published by Roth *et al.* [38]. This misalignment was caused by the preparation pressure, where one usually employs borazine at about $6 \cdot 10^{-6}$ mbar, while here a pressure of $3.4 \cdot 10^{-4}$ mbar was applied.
Nevertheless, it was possible to grow a thick BN film, even on this misaligned *h*-BN single layer on Cu(111). Figure 25(c) shows the pressure and temperature conditions for the thick layer growth procedure. The goals of the experiment were to employ the UV lamp setup (see section 3.3) and to identify the pressure required for the thick layer growth. The pressure dependent photocurrent at elevated pressure conditions is described in section 7.3.2 and could be handled by the application of a special borazine pressure protocol. As displayed in the lower part of Figure 25(c), the preparation temperature was kept constant, while the borazine pressure was scanned for conditions, which induce a non-reversible photocurrent change upon pressure decrease. All reversible photocurrent shifts upon pressure decrease are identified as effects of the photocurrent pressure dependence, which are marked by yellow bars and which are much more pronounced for the antenna signal. The condition for the thick film growth is marked with the red bar in Figure 25(c) with pressures of at least 0.25 mbar. At such high pressures, the gases in the chamber cool the sample significantly, since heat is more effectively transported from the sample

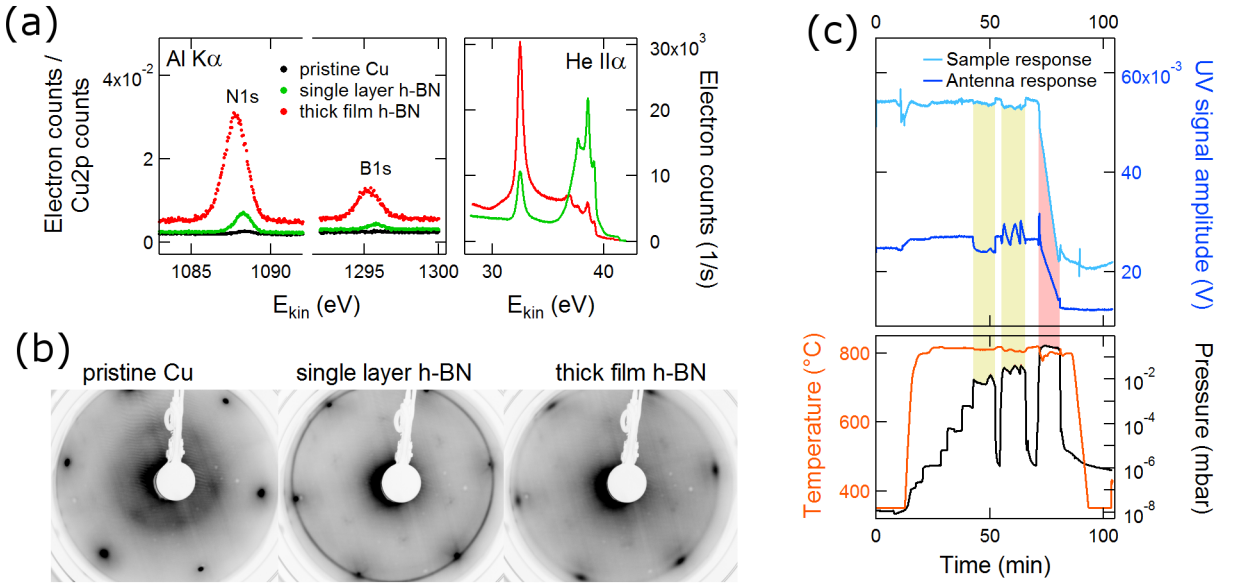

Figure 25: Thick h-BN preparation on Cu(111). (a) Al Kα XPS lines of the N1s and B1s core levels and the He IIα normal emission UPS data for the single and multilayer samples. The XPS core level data are normalized with the electron counts from the copper substrate in order to present the adlayer-substrate ratio evolution for the different BN layers. (b) LEED images at 65 eV for different preparation stages, indicating rotational disorder in the single h-BN layer template. (c) displays the experimental conditions such as pressure and temperature for the thick layer growth. The temperature was monitored with a pyrometer, which has been calibrated to a thermocouple reading prior to the experiment. The process is monitored with the UV flash lamp and both, the "sample" and the "antenna" photoemission yield are measured. The corresponding photoemission signal amplitudes are displayed as **sample response** and **antenna response** (see equation (15)). The **yellow areas** mark the pressure conditions, where the UV photocurrent becomes pressure dependent. The **red area** flags the pressure conditions for the thick layer growth, respectively.

to the chamber wall. The resulting sample-temperature drop has to be compensated by additional heating power, which is here accomplished by manual adjustments and which leads to the rather unstable temperature evolution in the lower part of Figure 25(c).

Concerning the ordering of the thick h-BN film, we have to rely on the LEED data provided in Figure 25(b). In contrast to earlier preparations [38], the single layer h-BN shows no alignment to the substrate. This is well-explained by the application of a precursor pressure, which was two orders of magnitude larger than for the standard procedure. It is known from single layer h-BN preparations on other metal surfaces that the h-BN layer grows by islands [21]. Those islands grow around nucleation sites, the number of which can be increased by preadsorption of borazine below the layer formation temperature [21]. Since borazine and its cracking products preferably stay on the metal surface [21], we can conclude that a high borazine pressure has the same effect than preadsorbed borazine. This is, an increased number of nucleation sites. Such an increased island density may increase the probability of misalignment and might explain the

observed LEED pattern. In the LEED data of the thick h-BN layer, the single layer features are conserved, but attenuated and blurred. This implies that the subsequent thick BN film does not follow the texture of the h-BN/Cu(111) substrate. Furthermore, the thick film has no additional LEED features, which supports the picture of a strongly disordered boron nitride film.
In conclusion, we can grow thick boron nitride films in the ESCA preparation chamber by high pressure borazine exposures. However, such conditions have a high probability of damaging UHV instrumentation. Therefore, alternative preparation procedures are suggested in section 4.3. It was also possible to monitor the thick layer growth with the photocurrent yield setup and the minimum growth pressure is identified to be about 0.25 mbar. The layer thickness for this particular experiment is 22.2±2.4 Å regarding the copper attenuation and 25.8 Å regarding the BN-elemental ratio (see next section 4.2.2).

4.2.2 Boron Nitride Layer Thickness Evaluation

In this section, the BN layer thickness determination is reviewed with respect to data from XPS as well as from photocurrent yield measurements. As exemplary XPS data, we use data recorded for the BN layer on copper from the experiment in the previous section 4.2.1.
For the XPS based thickness analysis, the basis of quantitative XPS is recalled and applied to a thick adlayer system. Ignoring XPD effects, the normal emission signal intensity from an infinitely thin substrate layer dz at a substrate to surface depth of z is given by the differential equation (34). It is proportional to the density of the emitters n, the photoemission cross section σ, the transmission function of the photoelectron detector T, the photon flux ϕ and the area of light exposure A. Because of inelastic scattering, the escape depth of an excited photoelectron is limited by its inelastic mean free path in the solid λ, which depends on the kinetic energy of the electrons. For the bulk substrate, integration of expression (34) from the surface to infinity yields the expected photoemission intensity I_0.

$$dI(z) = n \cdot \sigma \cdot T \cdot \phi \cdot A \cdot e^{-\frac{z}{\lambda}} dz \tag{34}$$

$$I_0 = \int_0^\infty n \cdot \sigma \cdot T \cdot \phi \cdot A \cdot e^{-\frac{z}{\lambda}}\, dz = n \cdot \sigma \cdot T \cdot \phi \cdot A \cdot \lambda \tag{35}$$

The photoemission cross section σ is polarization-, geometry-, element- as well as core-level specific and were calculated by Yeh and Lindau [54]. The transmission function T of analyzer also depends on the kinetic electron energy and needs to be determined, when comparing ratios of different electron core levels [55]. The inelastic electron mean free path λ, which depends on the electron energy and the material matrix, can be calculated [56, 57].
Figure 26(a) displays the photoelectron counts at different z positions along the surface normal of the system BN/Cu according to equation (35). The area integrals of these electron counts are the measured photoelectrons for the core levels of Cu2p$_{1/2}$, N1s and B1s. For the N1s and B1s electron counts it is straight forward to integrate equation (34) for an undetermined thickness d,

which results in equations (36) and (37). To account for the attenuation of the copper electrons in the BN layer, expression (35) has to be modified by the inelastic electron mean free path of these electrons in boron nitride, which is shown in equation (38). Here, the mean free path λ has two indices, the first to account for the kinetic energy of the electron and the second to identify the material, which the electron passes.

$$I_N = n_N \cdot \sigma_N \cdot T \cdot \phi \cdot A \cdot \lambda_{N,BN} \cdot (1 - e^{-\frac{d}{\lambda_{N,BN}}}) \tag{36}$$

$$I_B = n_B \cdot \sigma_B \cdot T \cdot \phi \cdot A \cdot \lambda_{B,BN} \cdot (1 - e^{-\frac{d}{\lambda_{B,BN}}}) \tag{37}$$

$$I_{Cu} = n_{Cu} \cdot \sigma_{Cu} \cdot T \cdot \phi \cdot A \cdot \lambda_{Cu,Cu} \cdot e^{-\frac{d}{\lambda_{Cu,BN}}} \tag{38}$$

Figure 26(b) displays the solution of equations (36), (37), (38) for a BN layer thickness d between 0 Å and 100 Å. While the electrons from the Cu2p$_{1/2}$ core level are rapidly suppressed with increasing BN layer, the electrons from B1s and N1s approach their bulk ratio, which is $\lambda_{N,BN}/\lambda_{B,BN}$ as derived from equation (35). The adlayer thickness can be determined by two methods. The first approach is by determination of the copper electron attenuation through the BN layer. The second method compares elemental ratios, which are unique for any thickness and calculated in the upper part of Figure 26(c).

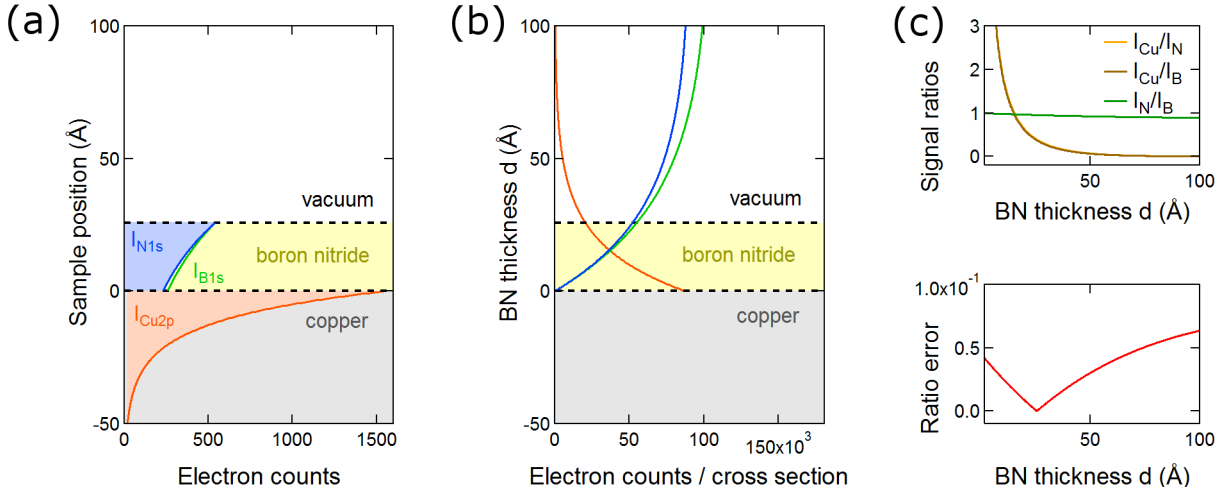

Figure 26: Photoemission intensities from the system BN/Cu. (a) displays the different photoemission intensities at a certain position along the surface normal for the system BN/Cu. The area integrals yield the photoemission electron counts I_{N1s}, I_{B1s} and I_{Cu2p}, which are displayed in (b) for a BN layer between 0 Å and 100 Å. The functions in (a) and (b) are exact calculations from the Al Kα XPS data and give an overview of the XPS core level signal attenuation or increase for a differently thick **boron nitride** layer. The upper part of (c) shows the evolution of the elemental ratios for differently thick BN layers. The lower part in (c) visualizes an error minimization of the measured B:N ratio compared to the calculated ratios at different thickness. The data are from the thick BN layer in Figure 25 and reveal a minimal error at a thickness d of 25.8 Å.

The copper substrate attenuation method is a calculation, which relies on equation (39), but it is susceptible to a large experimental error. The reason is that two measurements at two different times have to be compared. Being aware of this, precautions might be taken such as not turning off the x-ray source between the measurements, usage of the broad light spot of the Mg Kα x-ray source or referencing to the polycrystalline Ag sample. The calculation for the data in section 4.2.1 results in a thickness of 22.2 ± 2.4 Å. Here, the single layer h-BN/Cu(111) integral had been used for $I_{Cu}(0)$, because its value was 13 % larger than for the pristine Cu(111) crystal. It is likely that this deviation is caused by a different measurement geometry and it can be used to estimate the experimental error of this method. Error propagation yields an error of 2.4 Å .

$$I_{Cu}(d) = I_{Cu}(0) \cdot e^{-\frac{d}{\lambda_{Cu,BN}}} \tag{39}$$

The second method relies on a single XPS measurement and takes advantage of the different electron mean free paths at different kinetic energies. In order to predict the XPS intensity ratio for a certain BN thickness d, equations (36) and (37) are used. For a single measurement, the area A and the flux ϕ are constant. The ratio is further simplified by the assumption of a constant analyzer transmission function and a nitrogen:boron ratio of 1:1, which yield equation 40.

$$\frac{I_N \sigma_B}{I_B \sigma_N} = \frac{\lambda_{N,BN}}{\lambda_{B,BN}} (1 - e^{-\frac{d}{\lambda_{N,BN}}})(1 - e^{-\frac{d}{\lambda_{B,BN}}})^{-1} \tag{40}$$

The evolution of the elemental ratios are displayed in the upper part of Figure 26(c). The lower part of Figure 26(c) shows an error calculation to identify the thickness, which corresponds best to the measured value. The data from the preparation in Figure 25 indicate a boron nitride thickness of 25.8 Å. To assign a number of monolayers to the calculated thickness, a homogeneous layered h-BN structure is assumed. With an interlayer distance of 3.33 Å, which is half the unit cell [58], we end up with about 7.25 ± 0.5 monolayers of h-BN.

In principle, it is possible to additionally compare the elemental ratios to the copper substrate. It only requires the additional information of the corresponding emitter density ratios n_{Cu}/n_B and n_{Cu}/n_N. It turns out for this particular data set that the copper attenuation dominates the ratios and the calculated thickness results in the one calculated by equation 39.

A thickness determination with the UV lamp signal is not directly possible. Due to insulating properties of h-BN and its direct band gap of about 5.97 eV [59], the UV flash lamp cannot excite photoelectrons from the BN layer. This means that a thick BN layer attenuates the photoelectron yield in a similar way as the $Cu2p_{1/2}$ electron counts in Figure 26(b). It is therefore possible to apply formula (39). Unfortunately, the mean free path for 4 – 5.5 eV electrons above the Fermi level are difficult to calculate. As a first approximation, one may employ the empirical universal curve for solids, which leads to values between 60 Å and 120 Å [60].

Here, we determine the an average mean free path by comparing the experimental photocurrent attenuation to the XPS determined thickness. Following an exponential attenuation, as can be found in equation 39, the UV lamp photoelectron mean free path is determined to be 27 ± 0.2 Å.

4.3 Advanced High Pressure Exposures

This section starts with the introduction of different experimental parameters for the growth of boron nitride. It summarizes experimental observations and proposed mechanisms from the BN growth community and from our thick BN preparations in ESCA. The findings result in the basic concepts for the advanced high pressure experiments in section 4.3.6 and allow to proceed with investigations in the millibar regime.

4.3.1 The Pressure Effect on the Boron Nitride Layer

As discussed in section 4.2 and previous work [48], low precursor pressures limit the *h*-BN growth to the single layer, while single layer growth at high pressures does not lead to single *h*-BN layers. Here, we propose that this different growth behavior is based on a different growth mechanism. Experiments by Sutter *et al.* revealed that the BN growth rate at 1.3×10^{-8} mbar borazine is only proportional to the clean metal substrate area [25]. The experiment indicated a sticking below 1 % for borazine on *h*-BN compared to one on the metal. The sticking coefficient gives the probability for an impinging molecule to stay on the surface. Accordingly, a higher precursor pressure may compensate the lower sticking coefficient and maintain a similar amount of precursors on the surface, which are needed for the growth. If this is the case, the precursor pressure has to be increased at least 100 times in order to grow a thick layer. This would also mean that the initial growth condition is identical to the single layer situation and therefore the mechanism itself may be similar. This initial condition hypothesis is excluded by two experiments, where the total pressure is kept constant, but the partial pressure of borazine is changed by dilution with argon. A thick layer growth at borazine pressures above 0.25 mbar can be found in Figure 25(c), while the argon substituted experiment is described in section 4.3.6 and shown in Figure 29(a). XPS spectra of the argon dilution preparation do not show any traces of argon and display a B:N ratio corresponding to $\lambda_{B,BN}/\lambda_{N,BN}$. This excludes film composition changes e.g. an Ar doping of the BN layer. Therefore, the substitution of borazine with argon does not prevent the growth of the same thick boron nitride layer. In order to identify the reaction difference of the two experiments, we assume that argon and borazine evenly distribute in the chamber and that the gas and temperature profile is the same for both experiments. In this simple picture, the borazine-surface collision rate mainly depends on its partial pressure (see equation (44)). To account for the gas mixture, the smaller radius of argon leads to a smaller average gas collision cross section and an enlarged mean free path (see equation (42)). Since a larger mean free path does not change the gas-surface interaction, we neglect it. More importantly, argon has half the mass of borazine and momentum exchange during an argon-borazine collision, will result in less momentum direction changes for the borazine molecule. With an argon:borazine ratio of about 10:1, these collisions are favored and result in a probability decrease that a surface desorbed borazine molecule interacts again with the same surface. We therefore suggest that an argon dilution leads to a dilution of borazine molecules in the vicinity of and on the sample surface. Since the thick BN layer still grows with 10 times less borazine molecules on the surface, it is suggested that the 0.25 mbar pressure is not needed to

compensate a low sticking coefficient. It also means that the total pressure plays a more significant role than the partial precursor pressure, which indicates a reaction mechanism, where the sticking coefficient is less important. Apart from this gain of reaction insight, it leaves the dilution gas as free parameter to achieve a high background pressure, where different gases or gas mixtures may be tested for effects on the thick layer.
Concerning the choice of a such a dilution background gas, we know that a light gas such as helium might led to an uneven B:N ratio while the heavier argon does not [52]. For the application of He a total pressure of typically 2.6 mbar was used, while the total pressure for the Ar preparation was 0.13 mbar [52]. About the experimental reasons for these two different pressures can only be speculated, but the larger helium pressure implies that a compensation of the decreased mass and collision cross section is needed. This would also mean that gas phase collisions participate in the thick boron nitride layer growth.
Gas mixtures with H_2 are commonly used for the high pressure experiments [7, 48] and known to reduce the B-H or N-H species [52]. At a single layer preparation pressure of 1×10^{-7} mbar (borazine:H_2 = 1:10), H_2 affects the layer growth and the BN islands start to grow isotropically [25]. Without hydrogen, the islands have a preferential growth direction along the substrate terraces and at a heavy hydrogen pressures of 1×10^{-7} mbar, the BN islands get smaller. Instead of an Ar/H_2 background gas, N_2/H_2 had also been used to form thick BN layers [7].
This work focuses on Ar and Ar/H_2 background gases only. Both of them have been proven to achieve thick BN layers. For the Ar/H_2 mixtures, a ratio of 10:1 was employed. The application of background pressures has the advantage of not damaging the ESCA equipment (see section 4.2.1) and allows control of the precursor partial pressure. The precursor amount has been tried to keep as little as possible, in order to avoid severe film texturing as observed for the single layer *h*-BN on Cu(111) in Figure 25(b).

4.3.2 Temperature Effect for Thick Boron Nitride Layer Growth

Single layer boron nitride on metal substrates is known to grow uniformly across the sample at temperatures above 750 °C [1, 43, 61]. High temperature STM measurements revealed *h*-BN nanomesh formation on Rh(111) via triangular shaped islands [21]. The nucleation density was $3/\mu m^2$ and it was observed that the nanomesh starts appearing at 656 °C, but does not form a uniform layer covering the substrate. Only at temperatures above 777 °C the layer grows uniformly together.
For thick layers, a mechanism was proposed by Shi *et.al.* [48]. It is based on the formation of polyborazylene –small polymers consisting of borazine units– at temperatures above 70 °C [62]. The cross linking of these borazine chains is a polymerization reaction, which happens at temperatures between 125 to 300 °C, and the transition to *h*-BN occurs between 700 and 1100 °C. Interestingly, this low temperature boundary for the ordered *h*-BN formation [62] is close to the one observed by high temperature STM [21].
The phase diagram for crystalline *h*-BN reported by Matsuda *et.al.* reveals that the pressures applied here of about 0.25 mbar are ideal for the *h*-BN crystal growth [50]. The crystallization

temperature at these pressures is 1700 °C. At lower temperatures, *t*-BN describes the phase state of boron nitride. The crystal phase transition from *t*-BN to *h*-BN might start at lower temperatures of 1450 °C [51]. Recent research supports a slightly lower transition temperature for the single crystalline *h*-BN preparation at 1500 °C – 1700 °C [59].
In conclusion, thick *h*-BN crystals are only formed in high temperature furnaces, e.g., above 1500 °C [53]. The reason for such a high temperature is the minimization of *t*-BN formation. However, recent publications of thin *h*-BN films seem to omit considerations of the turbostratic ordering.

4.3.3 Substrate Effects

As discussed in section 4.3.1, the substrate is not expected to play a key role for the thick BN layer growth. So far, it grows on any hot surface, that includes the Rh(111) thin film, Cu(111) single crystals and their corresponding sample holders with steel and molybdenum parts. The desired ordering effect of a single crystalline substrate on a thick BN film formation could not be confirmed within this thesis. On the other hand, it had been reported that magnetron sputtering of BN on Ru(0001) and graphene/Ru(0001) did influence the BN layer alignment [63]. Although magnetron sputtering is not comparable to CVD, it still proves that the substrate is not entirely irrelevant to the growth of an aligned thin film.

4.3.4 Reaction Chamber Effects

The high reaction pressure of 0.225 mbar argon may lead to side reactions apart from the hot sample, e.g., on the chamber wall. We distinguish here a chamber wall reaction from a chamber wall collision or chamber wall induced precursor cracking. While the latter do not change the reaction gas composition, the former does.
Figure 27 displays the analysis of an experiment, which suggests the occurrence of chamber wall reactions. Argon, borazine and hydrogen up to a total pressure of 0.3 mbar were used and deposited about a monolayer of carbon on the sample. Gas contamination are excluded via mass spectrometry and via a second preparation, where the same gases could successfully deposit a thick BN layer on the same sample. The only difference was that prior to the second preparation, the chamber had been cleaned for hours with hydrogen and the hot dosing device (HDD).
Figure 27(b) displays the Gaussian background subtracted C1s XPD pattern of the high pressure borazine preparation. Because of the Mg Kα x-ray source, the C1s signal partially overlaps with a Rh3d satellite as shown in Figure 27(a). Therefore, it is hard to avoid an XPD pattern without a fingerprint of the Rh(111) substrate. For comparison, XPD pattern of graphene on Rh(111) are found in reference [22]. To exclude misinterpretations of the slight graphene fingerprint in this XPD pattern, the absolute signals from the Rh3d and C1s core levels are compared at a polar angle of 80° in Figure 27(c). As the twelve-fold symmetric periodicity only appears in the C1s signal, it has to originate from the carbon layer and indicates a graphene like ordering. As a carbon source, we can exclude the sample, the sample holder and the reaction gases, because

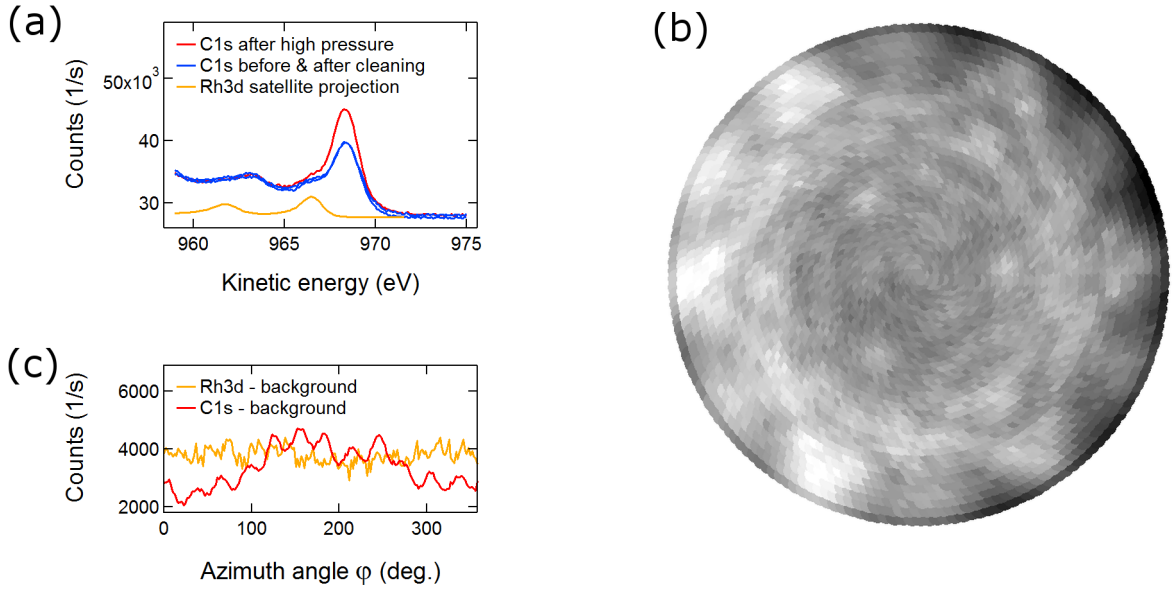

Figure 27: Carbon deposition with argon, borazine and hydrogen on a Rh(111) thin film. (a) displays Mg Kα spectra in the kinetic energy range of the C1s core level. The rhodium satellite of the Rh3d core level is projected into the same graph and helps identifying the features of the rhodium signal. The carbon core level does increase after the high pressure experiment and is reduced before preparation and after cleaning. (b) is a Gaussian background subtracted XPD pattern of the C1s core level after the high pressure argon, borazine and hydrogen exposure. The features of the Rh(111) substrate are still visible and (c) displays an azimuthal cut at a polar angle of 80° through the C1s and Rh3d XPD pattern.

exactly the same were used later for a thick boron nitride deposition, shown in Figure 30. The only difference was that the ESCA preparation chamber had been cleaned by several hours of hydrogen in combination with the hot dosing device. It is concluded that the chamber is the carbon source. Indeed, carbon can be found in macroscopic amounts on the complete deposition chamber wall. Therefore, this experiment signals that the chamber can play a role during the high pressure deposition processes. It indicates mass transport from the chamber wall to the sample and reveals the requirement of a clean chamber wall for the high pressure experiments.

4.3.5 The Growth Mode of Boron Nitride Layers

The growth mechanism of the monolayer BN on metal substrates is well understood. The BN layer starts growing at nucleation sites, where first triangular islands are formed [21]. A nucleation site does not have to be a crystal defect, but can also be preadsorbed molecules [21]. The layer growth speed is only affected by the clean metal substrate area [25]. Therefore, the single layer growth is well-described by a three step process which consists of precursor adsorption on the metal substrate, transport to a nucleation defect or an already existing island and integration into the layer. It is a very effective process, because most precursors arriving at the metal surface,

cannot leave it anymore [21].
In comparison, the growth mode of a thick BN film is less investigated and may follow a different mechanism as discussed in section 4.3.1. A possible reaction mechanism via polyborazylene has been suggested [48], without further details of the process. Nevertheless, it might be a valuable model of a transition state molecule, which features, e.g., an enhanced sticking coefficient on h-BN. Polyborazylene has a formation temperature of 70 °C [62] and because the borazine molecule prefers not to stay on the hot h-BN surface [25] and because of the dilution consideration in section 4.3.1, this polymerization reaction has to occur in gas phase close to the sample. In the following, we try to model the preparation conditions, e.g., an average gas phase temperature, in order to judge the suitability of the proposed transition state polymer.
The preparation conditions include the pressure as well as the sample, chamber and gas temperature. The sample and chamber wall temperature can be measured, which leave the gas pressure and its temperature to be determined. In the simplest picture, we assume that there are no pressure gradients. This assumption neglects chemical potentials and ignores any gas beam direction or leak valve position. As such, equation (41) might only be a reasonable assumption for the high gas pressure situation, e.g. 0.225 mbar.

$$\frac{dp}{dx} = 0 \tag{41}$$

From the kinetic gas theory, we can calculate the properties of a gas molecule or atom such as its mean free path λ, its thermal conductivity κ and the gas surface collision rate Γ [64, 65]. Figure 28(a)(b) display calculated values of those quantities with equations (42), (43) and (44). Atomic parameters had been deduced from argon, since it is the main reaction partner for the high pressure experiments in section 4.3.6.

$$\lambda = \frac{1}{\sqrt{2}\sigma n} = \frac{k_B T}{\sqrt{2} p \pi d^2} \tag{42}$$

$$\kappa = \frac{1}{3} nvcl = \frac{1}{3} p \sqrt{\frac{8}{\pi m k_B T}} cl \tag{43}$$

$$\Gamma = \frac{p}{\sqrt{2\pi d^2 m k_B T}} \tag{44}$$

Here, σ is the collision cross section, n the particle density, d the atom diameter, v the mean velocity and c denotes the heat capacity of that atom. For high pressures p, the distance l in equation (43) is the mean free path λ as defined in expression (42). Because λ depends inversely on the pressure, κ gets independent of the pressure, as illustrated in Figure 28(a). At low pressures λ is larger than the sample-to-wall distance, which limits the distance between two collisions. Therefore, l becomes the sample-to-wall distance and the thermal conductivity κ linearly decreases with decreasing pressure. This kink in the thermal conductivity κ at about $1 \cdot 10^{-3}$ mbar in Figure 28(a) helps distinguishing the “high” from the “low” pressure regime for the following considerations.

So far, any of the gas property calculations for Figures 28(a)(b) were performed at a temperature of 300 K. This is only true for calculations at pressures, below which the mean free path of Ar is longer than the sample-to-wall distance, i.e., on the left of the red dotted line in Figure 28(a). In this regime, it is more probable that an atom, which hits the hot sample, will rather loose the gained energy at the UHV chamber wall than interacting with other gas particles. An atom, which hits the chamber wall on the other hand will rather collide with either the chamber wall or the hot sample instead of another particle. These statements clearly depend on the chamber-sample geometry and gain validity, the lower the pressure. A collision of a particle with a surface may include an energy transfer. On average, the impacting atom will thermalize with the surface and its outgoing temperature will be dominated by the surface temperature. At low pressures the particle-particle interaction is low and the gas consists of particles, which did either hit the sample or the wall. Accordingly their temperatures (T_{cold}, T_{hot}) is either close to the sample T_{sample} or the wall temperature T_{wall}, as shown in equations (45) and (46).

$$T_{cold} \approx T_{wall} \tag{45}$$

$$T_{hot} \approx T_{sample} \tag{46}$$

Generally, something like an average gas temperature does not exist at low pressures, there are only hot or cold atoms. Nevertheless, if one measures the gas temperature with a macroscopic thermocouple, where both the hot and the cold atoms interact with the steel, we will measure an average gas temperature. In equilibrium, the energy loss ΔQ_{hot} of the n_{hot} atoms has to match the energy gain ΔQ_{cold} of the all cold atoms n_{cold} on the thermocouple. Equations (47) and (48) directly lead to the definition of the average gas temperature at low pressures in equation (49).

$$\Delta Q_{hot} = \Delta Q_{cool} \tag{47}$$

$$cn_{hot}(T_{hot} - T_f) = cn_{cold}(T_{cold} - T_f) \tag{48}$$

$$T_f = \frac{n_{cold}T_{cold} - n_{hot}T_{hot}}{n_{cold} - n_{hot}} \tag{49}$$

To solve equation (49), the sum and the ratio of the hot n_{hot} and cold particles n_{cold} are known and given in equations (50) and (51). The sum is defined by the ideal gas law and the ratio corresponds to the probability ratio of either hitting the chamber wall or sample. Ignoring geometries, this probability ratio is the ratio between sample and wall surface area.

$$n_{hot} + n_{cool} = \frac{pV}{kT} \tag{50}$$

$$\frac{n_{hot}}{n_{cool}} = \frac{A_{sample}}{A_{wall}} \tag{51}$$

The average gas temperature T_f has been calculated at low pressures for the case of the ESCA preparation chamber and is shown in a one dimensional scheme in Figure 28(c). Because the

gas particles do not interact with each other, the gas temperature between sample (at position zero) and wall (at position 0.1 m) is constant at any coordinate. The sample-to-wall surface ratio of 1:1000 leads to an average gas temperature of about 1 - 3 °C above room temperature. Essentially, for an UHV experiment, the reaction gas has the chamber wall temperature, no matter the coordinate within the chamber. Gas heating through radiation is omitted, but its contribution is small [66]. Thermal radiation rather effects the chamber wall temperature, which might rise for a long preparation in ESCA up to 30 °C. Accordingly, the reaction gas temperature might be about of 31 to 33 °C.

At high pressures, in the regime above the red dotted line in Figure 28(a), the particle-particle interactions start dominating the reaction gas temperature. To elucidate a temperature profile under such conditions, we still consider the condition (41) to be true and solve the heat diffusion equation in expression (52) [67]. For a constant thermal conductivity κ the differential equation (52) can be simplified to equation (53).

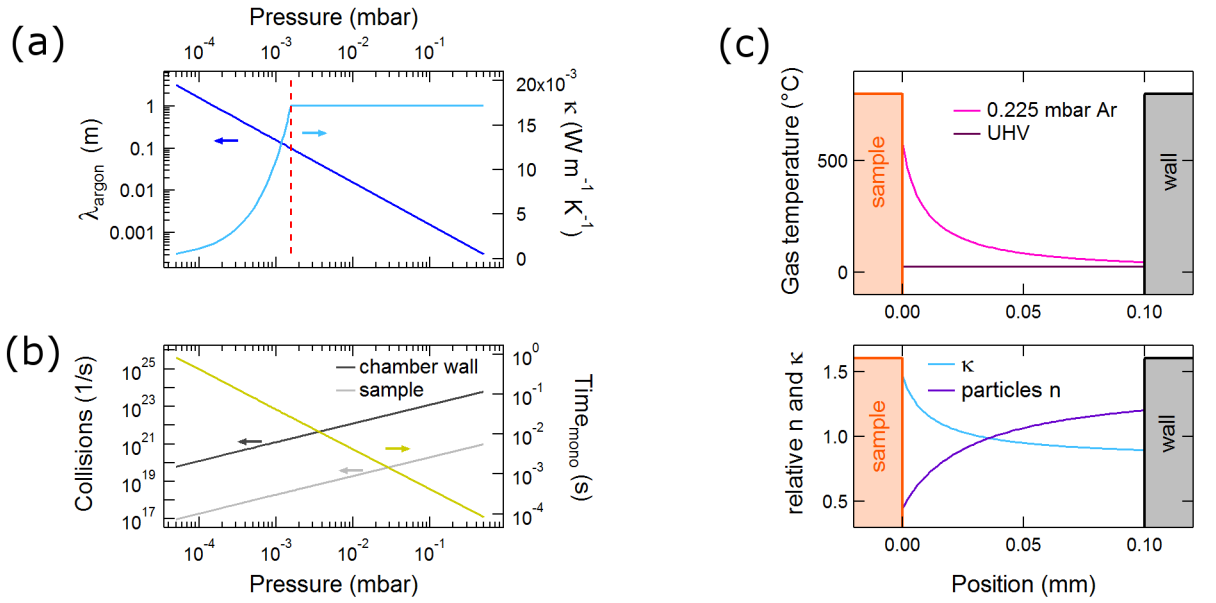

Figure 28: Chamber reaction conditions at different pressures. (a) shows the mean free path λ and thermal conductivity κ of argon in the ESCA preparation chamber. The red dots mark a pressure of $1.5 \cdot 10^{-3}$ mbar, below which the mean free path is longer than the sample-wall distance and above which it is shorter. (b) displays the surface collision rates on the chamber wall and the sample. The collisions on the chamber wall are three orders of magnitude larger, which is the dominating parameter for the average gas temperature at low pressures. The upper part in (c) displays the one-dimensional gas temperature profile for a preparation in ESCA. Such a presentation is adapted from a spherical sample-chamber wall geometry with only a radial temperature gradient. For the UHV preparation, the heat profile is a constant at about the chamber wall temperature, while the high pressure preparation displays a profile, which is a solution of the heat transfer equation. The lower part in (c) indicates the κ deviation from its mean value for the high pressure temperature profile above.

$$\nabla \cdot \kappa \nabla T + \dot{q} = \rho c \frac{\partial T}{\partial t} \tag{52}$$

$$\nabla^2 T + \frac{\dot{q}}{\kappa} = \frac{\rho c}{\kappa} \frac{\partial T}{\partial t} \tag{53}$$

These two equations are valid in three dimensions and $\dot{q}$ is a volumetric heat flow. For an analytical solution in three dimensions, we reduce the problem to a one dimensional heat profile by the application of a spherical sample and chamber wall geometry. In such situation, these differential equations only depend on the distance r from the sample. As boundary conditions, experimental data from a high pressure experiment are used –the experiment is shown in Figure 29(a). In this experiment, a gas pressure of 0.225 mbar was used and a thermocouple registered a gas temperature increase to 50 °C at the chamber wall. Upon increasing the pressure to 0.225 mbar argon, the sample needed 1.3 W more power to keep its temperature. Equation (54) is the steady state solution for a constant κ. The detailed mathematical path is given in the appendix in section 7.4.

$$T(r) = \frac{q r_{sample}^2}{\kappa} \left(\frac{1}{r} - \frac{1}{r_{wall}}\right) + T_{wall} \tag{54}$$

The solution to equation (54) is displayed graphically in Figure 28(c). The gas temperature at the sample surface reaches about 500 °C, which is beyond the temperature for the UHV reaction. Because of the non-constant temperature profile, the thermal conductivity κ, which is defined in equation (43), starts depending on its position within the reaction volume (see lower part of Figure 28(c)). It demonstrates a largest deviation of 20 % from the constant κ assumption, which led to equation (53). Furthermore, as the pressure is kept constant with condition (41), the particle density is decreasing towards the sample position, which results in a chemical gradient, which is not considered in this simple picture. However, a constant pressure ensures that the collision rate and the time for the monolayer coverage in Figure 28(b) is only reduced by the gas temperature in the high pressure regime.

In summary, the growth process of a single layer *h*-BN on a metallic substrate is well known and involves three reaction steps. They are precursor adsorption, transport the nearest defect or BN island and integration into the existing layer. The growth process of thick BN layers on the other hand is less investigated. Here, the reaction gas temperature for a high pressure experiment has been modeled based on experimental data. The resulting profile enables a precursor-precursor gas phase reaction, which might allow the reaction from borazine to polyborazylene. Such an intermediate reaction step was proposed in reference [48] and requires temperatures of about 70 °C [62].

4.3.6 Advanced High Pressure Boron Nitride

The considerations from the previous sections allow to predict and design high pressure experiments, which do not damage the pressure gauge, give further insight into the reaction mechanism or may align the *h*-BN layer.

To slow the growth rate and protect the pressure gauge, borazine is substituted with argon. The discussion in section 4.3.1 implies that borazine may be substituted by a variety of other gases. An argon-borazine mixture and the total pressure of about 0.24 mbar correspond to the conditions reported in reference [52]. Figure 29(a) displays the experimental procedure, where argon is colored in gray and borazine in green. The temperature was kept constant at about 770 °C and an argon pressure of 0.225 mbar had been stabilized for several minutes. The beginning and end of borazine dosing with a total pressure of about 0.25 mbar are marked by gray dotted lines, where the photocurrent yield displays a significant decrease. Such a photocurrent attenuation during the thick BN layer growth is in line with the findings in section 4.2.1 in Figure 25(c).

In addition to the photocurrent decrease, which can be assigned to a current attenuation due to an insulating adlayer, the UV lamp also records a photocurrent increase at the beginning of the borazine application. This increase is always more pronounced on the collector electrode and its nature is shown in Figure 29(b) and (c). The photocurrent integral is split into a signal amplitude and its decay constant τ (see Figure 19(b) and equation (15)). The photocurrent decay constant is defined by the RC circuit with the capacitance of the cables and the resistance of the oscilloscope (see section 3.3.1) and does not change for a UHV deposition (see section 7.3.2). But the decay constant is observed to slightly shift, when going from UHV to 0.25 mbar argon. For this particular experiment, the collector showed a shift of about 8 μs. Because all parameters of the RC circuit are kept constant, except the reaction chamber gas composition, this decay shift

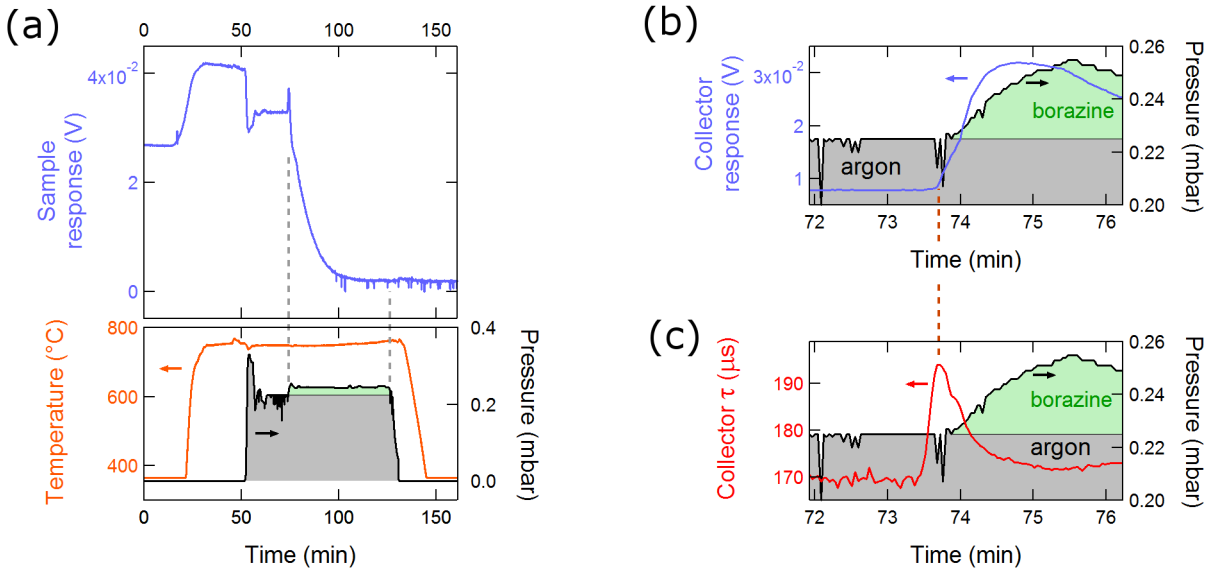

Figure 29: Thick boron nitride growth on Cu(111). (a) Displays a high pressure experiment on Cu(111). The high pressure is argon, where borazine is only added between the preparation time 74 – 126 mins as indicated by the gray dotted lines and the area in green. (b) is a detail of the collector photocurrent response, which increases at the beginning of the borazine dosing event. (c) shows the collector photocurrent decay constant τ, which has a maximum at the beginning of the borazine application.

is assigned to a capacitance change of the collector-sample system. Accordingly, the decay rate spike in Figure 29(c) corresponds to a capacity change of 20 pF and is assumed to be induced by a change of the gas dielectric constant ϵ_r. However, the capacitance spike at the beginning of the borazine application is not in line with a capacitance shift as observed, when changing from UHV to the millibar pressure regime. We suggest that it is caused by a gas composition change, which is terminated at the time, when the thick layer starts growing, e.g., when the photocurrent starts decreasing. As for that it may provide experimental indication for a precursor gas phase reaction prior to the thick layer growth and supports the gas phase reaction model introduced in section 4.3.5.

The experiment in Figure 29 did produce a boron nitride layer, for which the boron nitride ratio yielded a thickness of 113 Å and the $Cu2p_{1/2}$ attenuation 159 Å with the Si Kα x-ray source. The apparent discrepancy is attributed to a thickness, which is beyond the detection limit, i.e. where the B:N ratio or the $Cu2p_{1/2}$ attenuation do not change significantly anymore (see Figure 26(b)). This BN layer was analyzed by surface x-ray diffraction. The measurement was inconclusive and did result in visible beam damage of the *h*-BN thin film. A variety of meta-stable boron nitride films are reported at about the growth conditions applied here [50] and to advance into the direction of a crystalline *h*-BN film, hydrogen was added to the reaction gas according to the reference [52].

Figure 30 displays the analysis of a 12.8 Å thick boron nitride thin film which has been grown on a Rh(111) thin film. For this preparation, an argon-hydrogen mixture of 10:1 had been used as background pressure, the considerations for which are found in section 4.3.1. The preparation consisted of a UHV deposition of the single layer boron nitride and a subsequent thick film deposition within the same experiment. The employment of a Sinergia thin film should support the hypothesis that thick BN layers form on any substrate and is a first step towards the preparation knowledge transfer from the ESCA preparation chamber to the Sinergia chamber.

Neither the XPD nor the LEED patterns in Figure 30(a) and (b) indicate a *h*-BN ordering other than the well-aligned first monolayer. Figure 30(c) displays a Gaussian normalized polar cut through the average of all azimuthal points. XPD effects should appear as the ones displayed by the Rh substrate. At best, we might find a small and broad intensity accumulation at about 40°, which might as well originate from the *h*-BN monolayer. This demands a background subtraction of data from the *h*-BN monolayer in order to identify the features of the thick layer.

The only indication of having *h*-BN on the sample surface is given by Raman measurements in Figure 30(d). A broad signal appears at the position, where the bulk *h*-BN sample forms a sharp feature. Earlier Raman measurements of single and double layer films did not show any Raman signature, which means, the layer detected here has to be better decoupled from the substrate than the earlier attempts. Therefore, we can conclude that the top layer of the thick boron nitride film does seem to be consisting of *h*-BN units. In combination with the results from the LEED and XPD patterns, the BN thin film has to be strongly disordered, but still consists of *h*-BN flakes. From the phase diagram, we would expect a *t*-BN film, which confirms our findings.

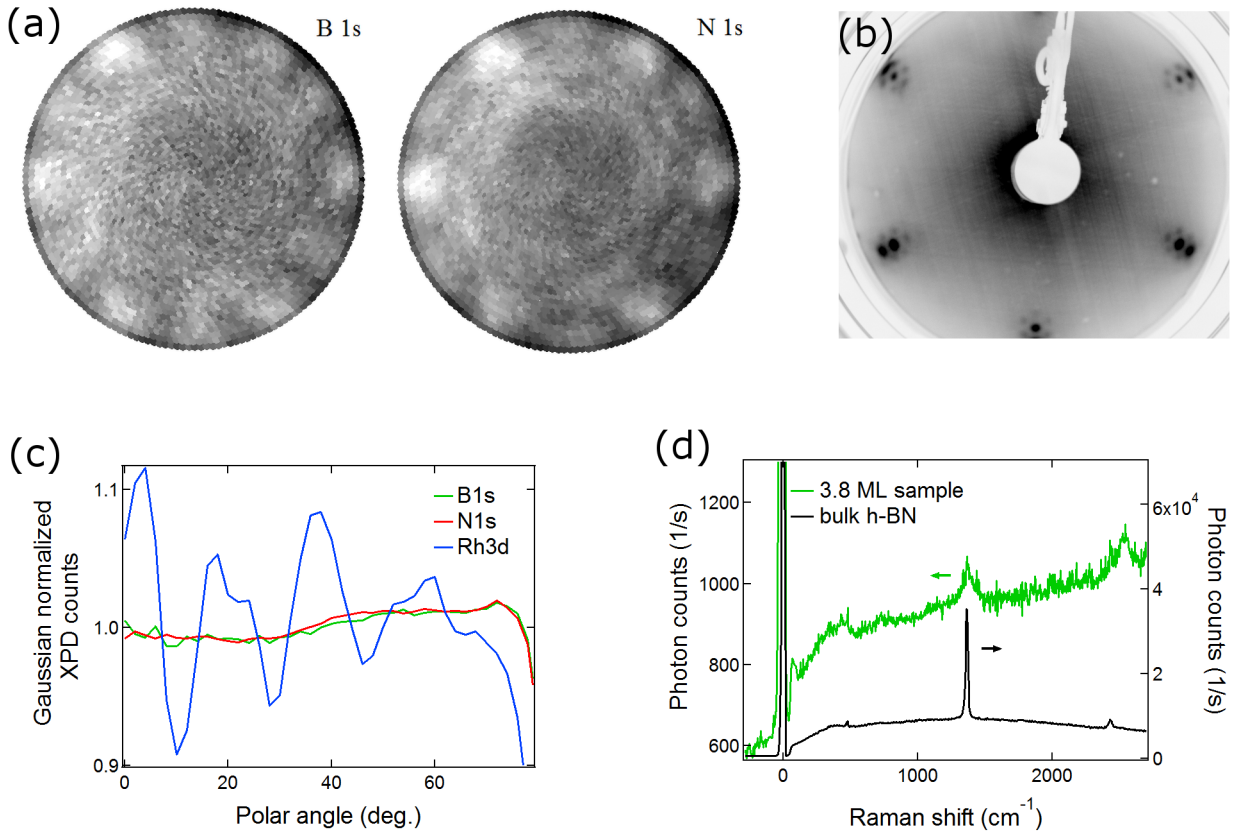

Figure 30: 12.8 Å thick boron nitride film deposition on a Rh(111) thin film. (a) displays the B1s and N1s XPD patterns, which are Gaussian background subtracted. They resemble the patterns found for the *h*-BN monolayer. (c) is a polar cut through a Gaussian background divided azimuthal average of boron, nitrogen and rhodium. (b) is the thick film LEED pattern at 60 eV. Indication for a thick *h*-BN film are only found in Raman measurements in (d). **This sample** displays a broad Raman peak, where the bulk *h*-BN sample forms a sharp feature at 1365.2 cm^{-1}.

4.4 Conclusion and Perspectives

Thick boron nitride films can be grown on all investigated substrates, including the sample holder surface. The growth procedure introduced in section 4.3.6 is not observed to damage instrumentation and helps sustain UHV conditions without subsequent chamber baking.

It is proposed that the mechanism for the thick layer formation differs from the one found for the monolayer of *h*-BN on metal substrates. Experimental indication for a different mechanism can be found in the necessity of high pressures, whereas the precursor partial pressure can be a fraction of the total pressure needed. Additional evidence is given by the UV photocurrent yield setup, which detects a gas composition change prior to the thick layer growth. Modeling of the gas temperature profile at high pressures reveals average temperatures, which could be high enough for a precursor gas phase reaction with polyborazylene as transition state polymer [48]. Apart from the gas phase reaction, the chamber walls were identified to participate in the high pressure experiments, but their exact role has not been investigated in detail. In fact, it is observed that a macroscopically

thick boron nitride layer grows, where the samples are covered with a molybdenum clamp. This clamp provides apart from sample fixation, a high reaction gas temperature between sample and clamp as well as a reaction "collision wall". In this sense, it is easy to design further experiments, which allow to figure the importance of the reaction gas temperature or the reaction "collision wall".

The produced boron nitride films are not observed to align with the substrate and are expected to have a turbostratic disorder. For a better alignment, a higher preparation temperature in the order of 1500 °C is known to produce crystalline h-BN [51, 59]. Such a temperature may not be reached by a standard sample holder in ESCA.

The Sinergia chamber offers a system, which may enter this temperature regime. So far, the highest temperature reached was about 1100 °C and was restricted due to a possible melting of the Silicon wafers. Changing from silicon to Al_2O_3 substrates, which are already purchased, can lift this restriction. Besides, the chamber is equipped with the needed differential pumping bypass, a valve for prevacuum gas dilution and a pressure sensor capable of recording pressures in the millibar regime. In addition, the chamber would allow optical measurements and the chamber wall could be cooled as well as heated during a preparation.

Therefore, it is not a matter of efforts to further pursue the preparation and investigations of thick boron nitride layers, but it is a matter of strategic positioning of these efforts and how to proceed with the produced films.

5 Transfer of Single Layer Hexagonal Boron Nitride

5.1 Introduction

The transfer of atomically ordered two-dimensional (2D) sheets onto arbitrary substrates may enable functionality from an atomically thin layer. For instance, few layer graphene was demonstrated to show field effects on SiO_2 [68] or it could be sandwiched between *h*-BN, where *h*-BN serves as gate dielectric [40]. Functionality may also be found for different materials, such as thin molybdenum disulfide (MoS_2) sheets, where photoluminescence is reported after transfer onto glass or polymers [69]. Therefore, the transfer of well-defined 2D layers is a possible route towards the fabrication of atomically-defined devices.

5.1.1 Motivation and Previous Efforts

The delamination and transfer of the monolayer of *h*-BN from its substrate offers the flexibility of arbitrary stacking and opens the door for a wide range of applications in a functional unit.
The first electrochemical boron nitride transfers at the University of Zurich, started with the activities of H. Cun and R. Rüttimann [70]. In autumn 2013, C. Bernard tried to find experimental proof of a successful transfer of *h*-BN with the setup and procedure introduced in reference [70]. But the project had been abandoned in late 2013, because of the complexity of the transfer process. The approach described here, is based on known electrochemical characteristics of the *h*-BN nanomesh. The experimental setup and procedures such as working electrode, solution, potential control, sample cleaning and the electrochemical potential protocol were revised completely. Only the samples, the transfer polymer and the spin coater used, are the same as reported in [70]. The following sections introduce the basis of the electrochemical experiment and provide evidence for the successful electrochemical transfer of single layer *h*-BN from the system *h*-BN/Rh(111) to amorphous SiO_2.

5.1.2 The *h*-BN Nanomesh in Solution

It is a key feature of the *h*-BN nanomesh that it survives immersion into liquids and keeps its structure in water as well as perchloric acid ($HClO_4$) solutions [4, 6]. A voltammogram of the *h*-BN/Rh(111) surface revealed an electrochemical hydrogen adsorption corresponding to about 0.25 monolayer [6]. Besides the physical adsorption effect, the voltammogram provides a fingerprint for the electrochemical identification of the *h*-BN/Rh(111) surface. Another observations was made by in-liquid STM investigations. Continuous sweeping of the potential could make the nanomesh superstructure disappear, but the BN layer is not removed from the surface and the nanomesh superstructure can be recovered by annealing in UHV. This effect has been interpreted as ion intercalation between the BN layer and the Rh substrate [6].
An ion intercalated transition step for the electrochemical removal of an adlayer is proposed and identified in reference [71]. The intercalation of atoms between the *h*-BN layer and the rhodium substrate has been studied in UHV [14, 72]. In particular, it was found that an exposure of

atomic hydrogen flattens the nanomesh structure, without destruction of the BN layer [72]. In this intercalated state, the normal emission XPS and UPS data strongly indicate an elevation of the BN layer to a position above the substrate, which was formerly occupied by the wire region of the nanomesh. Furthermore, STM data display the coexistence of the nanomesh superstructure with the flat BN layer, which implies that the intercalation process spreads from a BN layer defect and does not occur through the intact *h*-BN layer.
Since the numbers of thermally desorbed deuterium [72] and electrochemically adsorbed hydrogen ions [6] are similar, it has been concluded that the electrochemical hydrogen adsorption also involves a nanomesh superstructure flattening. This motivated a series of experiments as found in reference [17]. Here, we intended to use the proposed electrochemical flattening of the *h*-BN layer as transition state to support the *h*-BN transfer. Moreover, we also tried to reproduce the voltammogram of the nanomesh to enhance the *h*-BN nanomesh detection possibilities of the Sinergia laboratory.

5.2 The Electrochemical Setup

Requirements for the electrochemical setup were electrochemical potential control of the sample, capability to reproduce the voltammogram of R. Widmer *et al.* [6] and a high flexibility to optimize the sample potential protocol. To comply these needs, a three-electrodes setup was realized and is introduced in Figure 31.
Figure 31(a) displays the electronic scheme of the setup, where the upper part is the electronic hardware according to the three-electrodes cell [73], while the lower part in the blue background displays an electronic circuit, which is equivalent to the electronic situation in the solution [74]. This three-electrodes cell corresponds to a setup commonly known as potentiostat. A voltage source (Keithley 2635A, USA) powers a current between sample and working electrode (1), while the potential of the sample (3) is controlled via a reference electrode (2) with a separate voltage measurement unit (Keithley 2100, USA). The powering potential is generally independent of the desired potential between the sample-liquid interface. A software proportional-integral-derivative (PID) controller calculates the needed powering potentials between the sample and the working electrode.
In order to understand the electronic circuit between the three electrodes in solution, the fundamentals of a liquid-metal interface are reviewed as well as the functionality of the reference electrode [75]. A metal-solution interface can be described with two different processes. If charge transfer is not significant, the interface can only be polarized and it is best described by a capacitor. A polarized interface leads to the ordering of charged species in the solution close to the electrode. Such an ordering is called the electrical double layer (or Helmholtz double layer) and is described by the double layer capacity C_d. In the case of a significant charge transfer, the polarization of the electrode may be small and the system is defined by an interface resistance only, which is referred to as faradaic resistance R_f. In a metal-solution interface both processes occur simultaneously, but their contributions differ depending on the electrode potential. An example is the electrolysis of water, where a low potential does not lead to a significant charge transfer

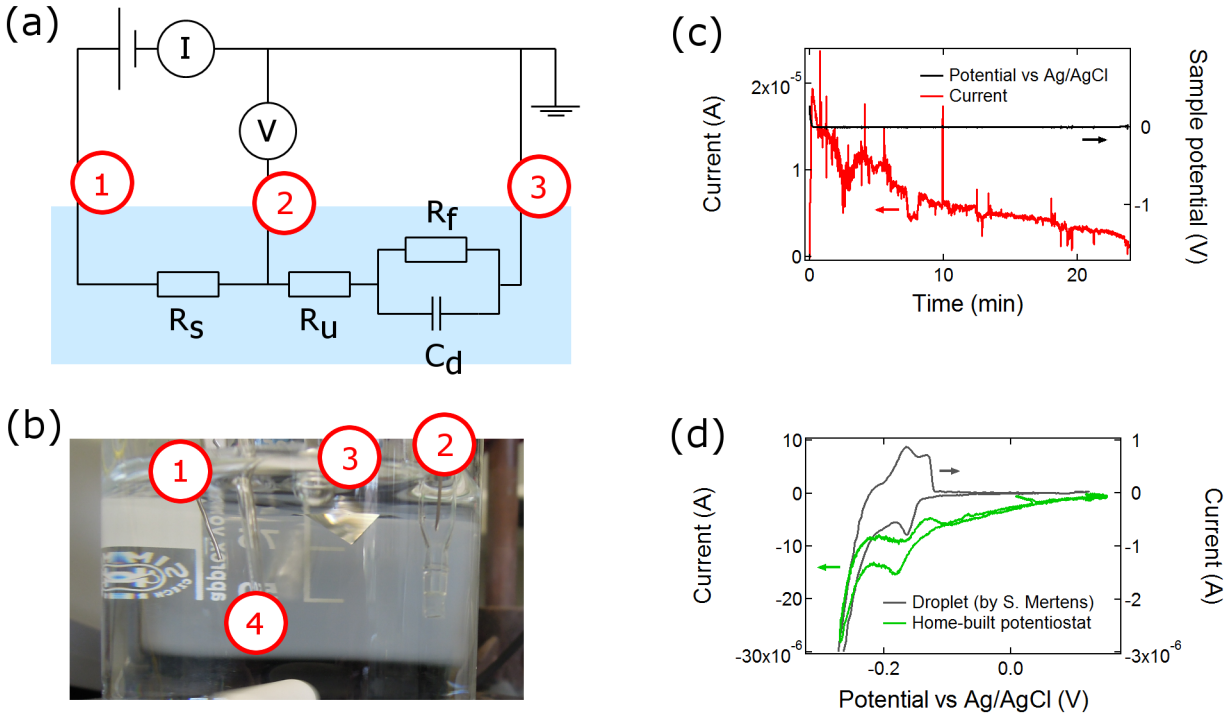

Figure 31: Setup and capabilities of the home-built potentiostat. (a) shows an electronic scheme of the electrochemical cell. The voltage source and the current measurement unit (I) are realized with a Keithley 2635A. The voltage (V) is measured via the 10 GΩ resistance of a Keithley 2100 multimeter. The electric circuit with the blue background is the equivalence of an electronic circuit between the three contacts in solution. The three contacts are; (1) working electrode, (2) reference electrode, (3) sample. (b) is a picture of the setup in (a), where (4) is a nitrogen supply needle. Nitrogen is used to reduce the dissolved oxygen, which appears as background current in voltammetry. (c) displays the current reduction for 25 min of nitrogen purging at zero sample potential vs Ag/AgCl. (d) is the voltammogram of a *h*-BN nanomesh after the nitrogen procedure in (c).

and the electrodes are best described by the double layer capacitance. At higher potentials, water is split into hydrogen and oxygen, which involves charge transfer between solution and electrode. This corresponds to an interface situation, where the faradaic resistance component is dominating.

Both, C_d and R_f are displayed for the sample-electrolyte interaction (3) in the solution part of Figure 31(a). In principle, the working electrode (1) has the same electric solution contact. Because the solution potential at the sample-electrolyte interface is determined by a reference electrode (2), an extended treatment of the solution-working electrode potential can be omitted. Considering the Ag/AgCl reference electrode, its design separates the Ag wire from the electrolyte by an intermittent well-defined KCl solution. A picture can be found at (2) in Figure 31(b), where the brown color of the Ag wire indicates the formation of AgCl. As long as no currents are directed through the reference electrode, this design ensures a constant potential interface between

the Ag wire and the KCl solution. A porous glass membrane contacts the KCl solution with the electrolyte of the electrochemical cell and the electrolyte potential is determined by a liquid-liquid interface. Therefore, the reference electrode can directly sense a solution potential and the Ag/AgCl/KCl interface only induces a constant potential offset. The resistances R_S and R_U are solution resistances, which are related to potential drops in solution. R_U is the uncompensated resistance, which accounts for potential errors due to a non-ideal geometry, where the reference electrode is far from the sample and the solution displays a large resistance.

In order to measure a voltammogram and acquire sample surface information, solution dissolved oxygen has to be minimized. Dissolved oxygen induces background currents, which predominate a liquid-sample response. Figure 31(c) displays the current decrease at constant sample potential while purging the solution with nitrogen. The sample current could be decreased by an order of magnitude within 25 min. The current spikes are from nitrogen bubbles, which either de- or attach to one of the electrodes.

The green voltammogram in Figure 31 is measured with the setup presented here and compared to a voltammogram measured by S. Mertens. While the main features such as the hydrogen adsorption peak are conserved, the home-built system displays a considerable background current as well as a slight potential shift. The background current is most probably induced by remaining oxygen ions or nitrogen, as S. Mertens used argon for the oxygen removal. The slight potential offset can be explained by the reference electrode, which was reaching its lifetime limit.

5.3 Electrochemical Transfer of the *h*-BN Layer

5.3.1 Electrochemical Stability of the *h*-BN Nanomesh

A viable solution for the electrochemical removal of the h-BN nanomesh from rhodium is 0.1 M perchloric acid ($HClO_4$), since it is already demonstrated that the nanomesh is stable in such an environment [6]. Alkaline solutions, such as 1 M NaOH, may destroy the integrity of the h-BN layer [70]. Besides, Widmer *et al.* did observe a surface morphology change in perchloric acid solutions, which has been proposed to originate from ion intercalation between the BN layer and the Rh substrate [6]. Such an intercalation could weaken the h-BN interaction to the substrate and help removing the adlayer.

Figure 32 illustrates that the BN layer is stable upon electrolysis. A bare BN/Rh(111) thin film sample has been exposed to potentials at which hydrogen electrolysis happens on the Rh thin film. Figure 32(a) shows the hydrogen bubbles forming on the sample during such a procedure. For several such experiments, the remaining boron on the sample is larger than 80 %. This means that the formation of hydrogen gas does not promote the removal of the BN layer and the BN layer is stable in such conditions. The potential procedure applied follows the method introduced by Koren *et al.* [71] and is based on hydrogen intercalation prior to electrolysis. This approach will be explained in detail in section 5.3.2.

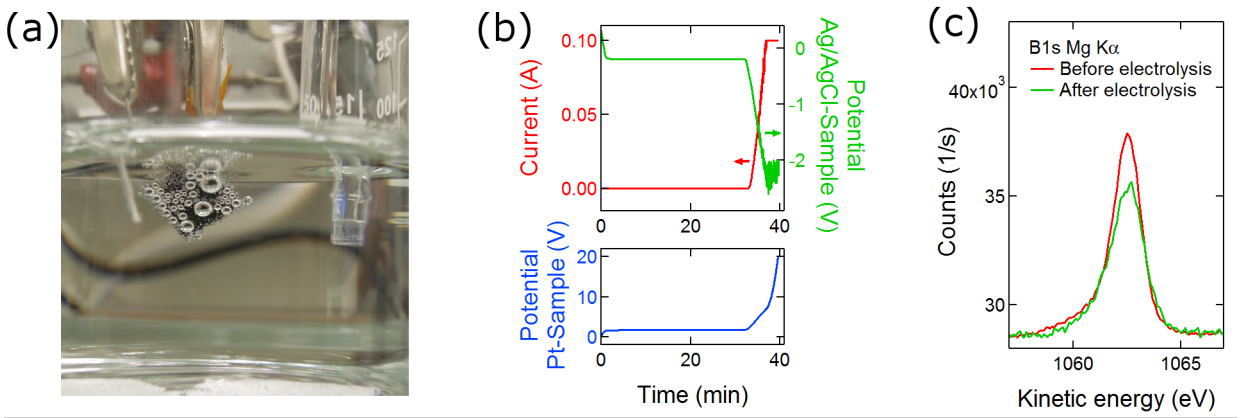

Figure 32: Stability of the *h*-BN nanomesh as electrolysis electrode. (a) illustrates the electrochemical stability setup. (b) sample current and potentials for the same sample. In the first 30 min, the sample potential vs Ag/AgCl has been kept constant at -0.2 V, which is below the hydrogen adsorption of the system. If intercalation occurs, it should weaken the interaction for the consecutive voltage ramp down to -2 V sample vs Ag/AgCl. For the procedure here, an overall charge of 25 C has been deposited on the sample, which is about 25 times more than for the most successful transfer procedure. (c) displays XPS measurements before and after the electrolysis procedure displayed in (b). The remaining boron is 83.4 % of the initial amount.

5.3.2 The Concept of Electrochemical Delamination

The delamination of an adlayer by an electrochemical reaction, which occurs between the adlayer and the substrate, was demonstrated for graphene on several metal substrates such as Cu or Pt foils [76, 77]. The graphene/metal foil is coated with a transfer polymer such as polymethylmethacrylate (PMMA), immersed into an electrolyte, where the application of a potential leads to electrolysis and the formation of hydrogen bubbles between PMMA/graphene and the metal substrate. These hydrogen bubbles are the driving force for the graphene-substrate separation and exemplary illustrations can be found in [76].

Figure 33(a) illustrates the *h*-BN delamination via hydrogen bubble formation on the Rh substrate. The mechanism is adapted from the graphene-substrate separation [76,77]. For the system BN/Rh(111) STM studies in UHV indicated that hydrogen can not penetrate the BN layer, but has to react from defect sites [72]. Therefore, the hydrogen bubble formation is expected to start at defect sites and the BN layer is continuously removed from such defects. The experiments in section 5.3.1 exclude such a mechanism and reveal that hydrogen bubbles are preferably formed on top of the BN layer, which is illustrated in Figure 33(b).

A modified procedure and reaction pathway was proposed by Koren *et al.* for graphene on Ru(0001) thin films [71]. Prior to the electrolysis and generation of gaseous hydrogen, the gr/Ru thin film samples are conditioned by hydrogen underpotential deposition as illustrated in Figure 34. The underpotential deposition corresponds to a process, which happens below the potential for electrolysis and in the case of BN/Rh(111) this is the potential for the hydrogen adsorption at

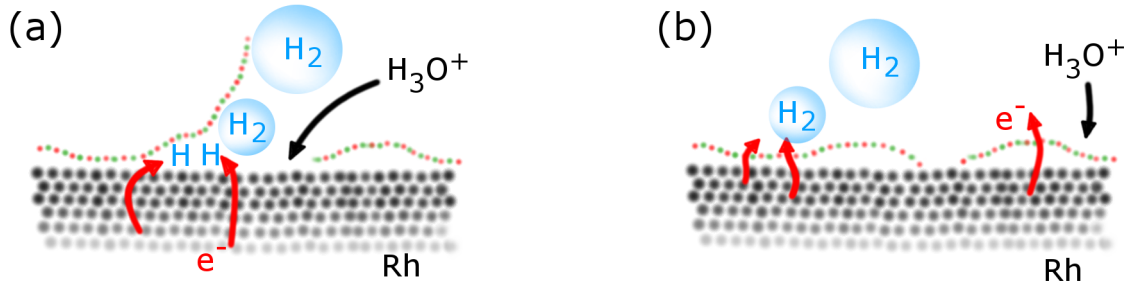

Figure 33: Mechanisms for the electrochemical reaction of the BN/Rh(111) electrode. The **green** and **red** dots illustrate the BN layer, while the **black** dots are the Rh substrate. (a) displays the separation mechanism proposed for graphene. The reaction of dissolved hydrogen ions to gaseous hydrogen occurs between the adlayer and the substrate and therefore promotes the removal of the adlayer. (b) is the main reaction mechanism as measured in section 5.3.1.

about -0.18 V vs Ag/AgCl (see Figure 31(d)). Figure 34(a) illustrates the expected situation for an underpotential deposition of hydrogen on a *h*-BN/Rh(111) system. The BN layer is expected to be flat and slightly elevated, as shown for the intercalation of atomic hydrogen in UHV [72] and discussed in section 5.1.2. The subsequent electrolysis of a hydrogen intercalated sample could then take place between the Rh substrate and the BN layer, which should promote the BN removal. This situation is visualized in Figure 34(b). Nevertheless, such a mechanism can as well be excluded, since the procedure applied for the sample in Figure 32 included a 30 min long underpotential hydrogen deposition. For graphene, the hydrogen underpotential deposition on the metal substrate was accompanied by a water accumulation between graphene and the metal [71]. Such a potential derived water diffusion underneath the BN layer is so far not observed for the *h*-BN/Rh(111) system. Electrochemical STM studies rather indicated that intercalation only occurs for a surface under continuous potential sweeps [6].

In summary, the electrochemical separation of the BN layer from the Rh substrate does not occur via the proposed mechanisms for the separation of graphene from its substrate [71, 76]. Here, we

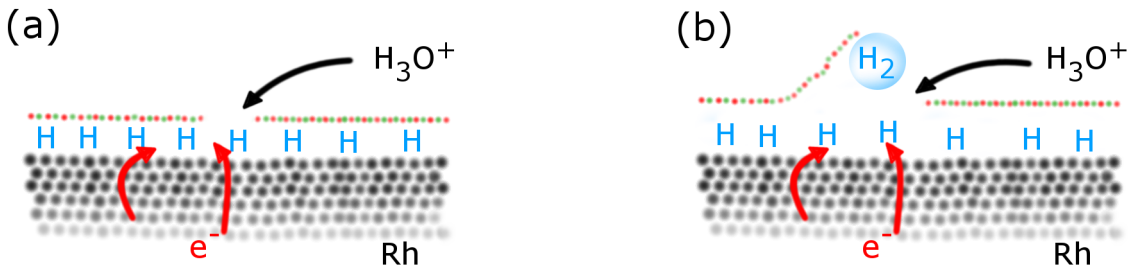

Figure 34: Proposed separation mechanism for the electrochemical reactions with underpotential hydrogen deposition. Hydrogen is adsorbed on the Rh metal in (a), prior to electrolysis in (b). The **green** and **red** dots illustrate the BN layer, while the **black** dots are the Rh substrate. **H** is hydrogen, which is adsorbed to the Rh metal.

observed that the covering PMMA layer, which acts as a transfer support, does also play a major role in the separation of the BN layer from the substrate. As XPS data showed, a PMMA coating of a previously cleaned *h*-BN/Rh(111) thin film sample allows the removal of 50 – 80 % of the BN layer at 25 times reduced deposited charge than shown in section 5.3.1.

5.3.3 The Frame Assisted PMMA Transfer

A reliable routine for the transfer of the 200 - 400 nm thick PMMA layer with the electrochemically removed *h*-BN can be found in reference [78]. A plastic frame of polyethylenterephthalate (PET) is glued on top of the coated PMMA film, which keeps the shape of the PMMA film, helps handling the transfer and allows identification of the PMMA orientation.
The procedure applied here uses a double Kapton tape frame, which offers the same semi-rigid mechanical property, chemical inertness and the advantage of already including a sticky side. Figure 35 illustrates the four transfer steps, which guarantee a high PMMA transfer success. It starts with the fixation of a double Kapton frame on the PMMA/*h*-BN/Rh(111). The sample is immersed into the solution and exposed to the potential procedure for the BN transfer. During this step, the Kapton covered parts of the sample do not react with the solution and will not detach from the sample unlike in reference [78]. In contrast to graphene, where it appeared to be important for the transfer that the sample edges are exposed to the solution [71], our experiments are inconclusive concerning this aspect. The Kapton frame/PMMA is removed in deionized water and transferred to a SiO_2 substrate. The remaining frame can be detached from the sample, after annealing for a few minutes to about 100 °C.

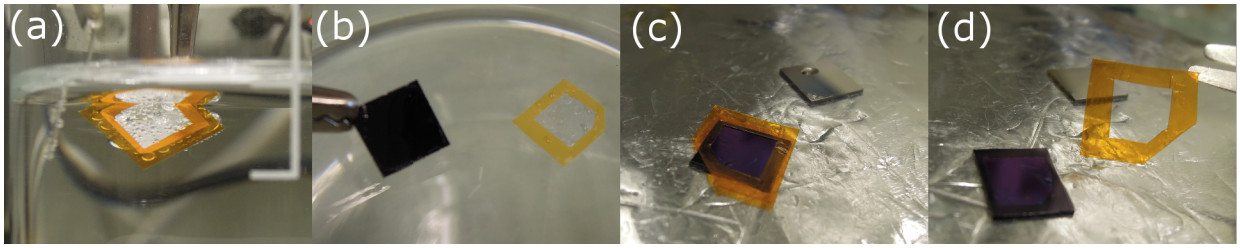

Figure 35: Illustrations of the PMMA transfer procedure steps. (a) electrochemical treatment of the PMMA coated sample with a double Kapton frame. (b) removal of the double Kapton frame with the attached PMMA film in deionized water. (c) Transfer of the double Kapton PMMA film on 90 nm SiO_2 and 5 min heating to about 100 °C. (d) removal of the double Kapton frame.

5.3.4 The Delamination Potential Procedure

The potential protocol to separate the *h*-BN layer from the substrate is a parameter, which has been neglected [76] or used to, e.g., precondition the sample [71]. Two tested potential protocols are shown in Figure 36.
Figure 36(a) displays a potential procedure, which starts by preconditioning of the sample for 85 mins at -0.2 V vs Ag/AgCl. This protocol is adapted from reference [71], where hydrogen

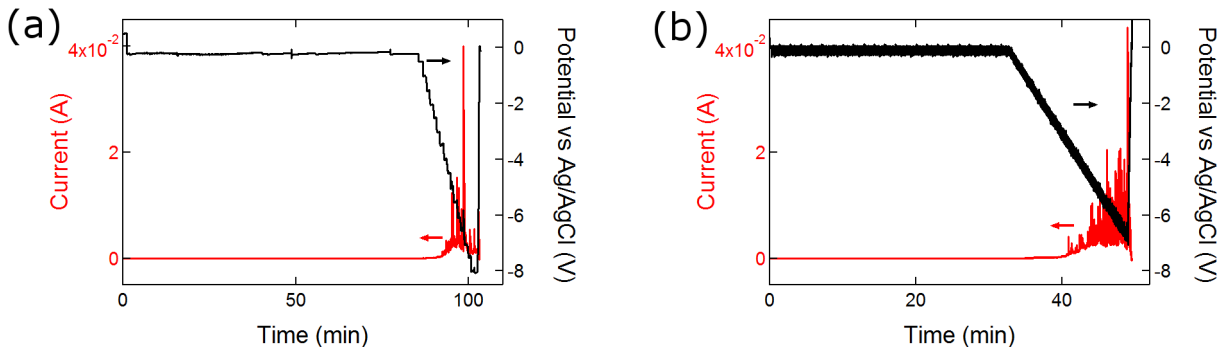

Figure 36: The potential procedure for the *h*-BN transfer. (a) is a procedure with an initial -0.2 V vs Ag/AgCl sample conditioning for 85 mins. This conditioning is intended to promote hydrogen intercalation to weaken the *h*-BN to substrate interaction. The subsequent voltage ramp reaches -8 V in 15 mins and the total deposited charge was 1.56 C. (b) is an alternative procedure, where 0.2 Hz potential oscillations with an amplitude of 0.3 V are applied during the complete process. The total deposited charge was 2.2 C. This approach is intended to imitate the intercalation conditions observed in reference [6].

was intercalated between the graphene adlayer and ruthenium substrate with potentials below electrolysis. The -0.2 V applied were intended to provide potentials below the hydrogen adsorption peak in the voltammograms in Figure 31(d). This intercalation protocol follows the mechanism proposed in Figure 34. Although up to 56 % boron nitride had been transferred with such a procedure, a reproduction appears to be challenging.

The procedure in Figure 36(a) applies potential oscillations with 0.2 Hz and 0.3 V amplitude. This is based on the observation in reference [6] that potential scanning leads to intercalation between the adlayer and the rhodium substrate. The protocol also takes into account a large uncompensated solution resistance R_U between reference electrode and sample (see Figure 31(a)). Such resistance may occur due to the PMMA coating, which restricts solution diffusion to the sample surface. After 32 mins the potential is scanned to -7 V in 15 min, while the 0.2 Hz oscillations were maintained. It was intended to scan through the intercalation conditions of R. Widmer [6]. So far, transfer rates up to 18 % are achieved with this protocol.

Despite of the apparent lower maximal transfer rate of the oscillating potential protocol, it offers several advantages. First, it may allow to further reduce the maximum voltage applied for the PMMA separation. This reduces the hydrogen bubble formation, which is suspected to dissolve separated *h*-BN from the PMMA polymer. A reduction of 1 V is shown in Figure 36, but it may be further reduced. Second, the oscillation protocol suppresses charging effects of the PMMA layer, which is observed on an irregular basis with the protocol in Figure 36(a). It is suspected that a charged PMMA may reduce the transfer rate as well, since it indicates the presence of uncompensated charges in the PMMA layer or a polymer composition change.

5.3.5 Structure of the Transferred Boron Nitride

The identification and characterization of the transferred BN layer had originally been intended to be accomplished optically with a Raman microscope. But the instrumentation available in house, such as XPS and XPD, are less responsive to an incomplete PMMA removal than the optical method and therefore more suitable for the first identification of the nature of the transferred BN layer. XPS chemical shifts of the B1s and N1s core levels are sensitive to their neighboring atoms. Such measurements indicated a chemical transformation of the BN layer for the electrochemical procedure introduced by R. Rüttimann and used by C. Bernard [70].

Figure 37 shows XPD patterns of a transferred BN layer on SiO_2 and compares XPS chemical shifts of *h*-BN on rhodium with the ones from the transferred layer. The XPD patterns of the B1s and N1s core levels in Figure 37(a) are Gaussian background subtracted, no azimuthal averaging procedure is applied. This excludes azimuthal symmetry artifacts from a normalization procedure in the data presented. Therefore, the apparent 12-fold symmetric B1s pattern has to be originated from the ordering of the BN layer, while the N1s symmetry even implies a 6 fold symmetric BN alignment. These symmetries indicate the conservation of the *h*-BN layer throughout the electrochemical transfer.

The B1s and N1s XPS spectra before and after the transfer are displayed in Figure 37(b). Because the transfer substrate SiO_2 is insulating, charging of this layer is expected, which induces an additional XPS energy shift. To correct this shift, the binding energy of the carbon surface contamination has been used and compared to the values in [79]. In addition to this correction, the original data from the *h*-BN/Rh(111) is corrected according to the shift of the Rh3d peak

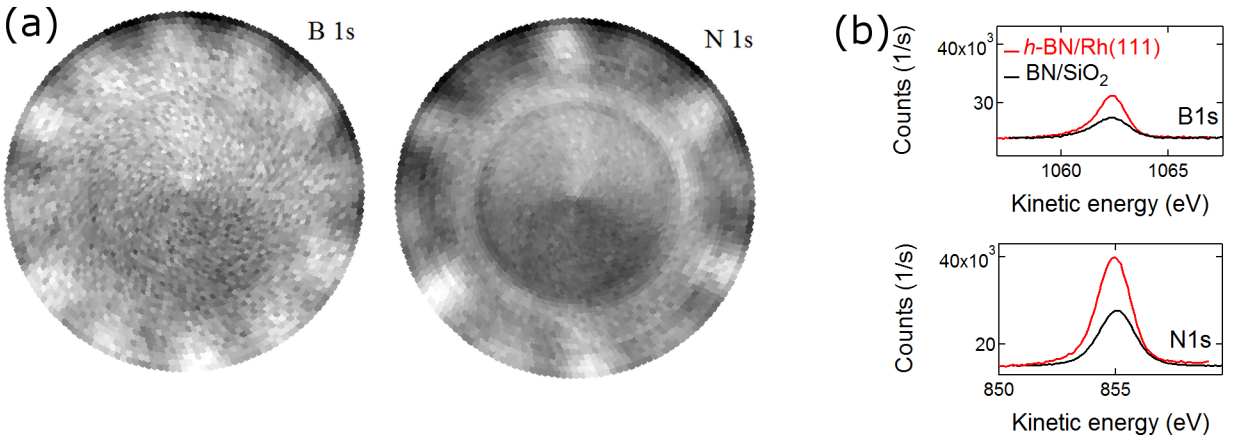

Figure 37: XPS and XPD analysis of the transferred BN layer. (a) Gaussian background subtracted B1s and N1s XPD pattern of a BN layer transferred to amorphous SiO_2. (b) displays XPS Mg Kα spectra of *h*-BN/Rh(111) and BN/SiO_2. A linear background had been subtracted to align the two peaks. A chemical shift correction was performed with the Rh3d reference shift for the *h*-BN/Rh(111) sample and with the C1s surface contamination reference shift for the BN/SiO_2 sample. The resulting spectra reveal no chemical shift between the original and transferred boron nitride.

with the tabled values in [79].
With normal emission XPS data, it is possible to derive the ratio between transferred and initial boron and nitrogen amount. In the best case about it is about 56 %, which corresponds a partial *h*-BN layer transfer. So far, investigation of the XPS chemical shift as well as XPD measurements support the hypothesis that the partially transferred layer consists of intact *h*-BN flakes.

5.4 Conclusion and Outlook

The concept of an electrochemically promoted adlayer separation is inspired by graphene transfer [76,77]. Here, an electrochemical setup is introduced, which is capable of acquiring voltammograms and able to electrochemically identify the *h*-BN/Rh(111) surface. The setup is also used to investigate the electrolysis driven *h*-BN separation from the Rh substrates.
It was shown that an electrochemical separation of the *h*-BN layer from rhodium cannot be driven by electrolysis only. Electrolysis in combination with a underpotential hydrogen deposition could only remove up to about 20 % of the boron nitride layer. This excludes several proposed transfer mechanisms for the *h*-BN/Rh(111) system [71, 76]. Instead, it is observed that the PMMA polymer, which is used as a transfer support, influences the electrochemical delamination significantly. Experimental evidence is shown that the partially transferred *h*-BN layer keeps its integrity and is not changed chemically. Other aspects of the *h*-BN transfer process, such as the PMMA removal after deposition onto an arbitrary substrate or the optical identification of the transferred layer are ongoing and not part of this thesis.
The limited transfer rate of the single layer is an issue for possible applications as a protection or separation layer in any device. The combination of the methods introduced here with the thick boron nitride films samples investigated in chapter 4 may yield a separated *h*-BN layer, which overcomes the flaws of a low transfer rate. Samples as well as transfer setup could readily be used.

6 Summary and Outlook

This thesis presents the facilities to grow atomically-defined surfaces on four-inch wafers by means of chemical vapor deposition. It includes investigations of in-situ monitoring of an atomic single layer growth process and concludes with explorations to further functionalize the produced surfaces.

In a first step, the CVD growth of *h*-BN on Rh(111) is upscaled to four-inch wafer substrates. The employed substrates were single crystalline thin metal film wafers from M. Schreck, Universität Augsburg, Germany [9]. The adaptation of the *h*-BN deposition onto these substrates includes the installation and development of annealing and reactive ion sputtering systems at the four-inch scale. Annealing was accomplished by a boralectric heater and ion sputtering provided by a large-area plasma source. The produced *h*-BN layers were found to have excellent quality, concerning surface sensitive analysis with LEED, XPS and STM.

To ensure the high quality of the produced samples, in-situ growth monitoring systems have been evaluated. The optical approach, where the reflection of polarized light is examined, turns out to be challenging. Our ellipsometric setup can monitor surface oxidation and the growth of *h*-BN on Rh(111), but requires a thermal drift compensation procedure, such as preheating of the UHV chamber for 18 hours. The photocurrent yield setup exploits the photoelectric effect, where an ultraviolet xenon flash lamp provides the excitation source for photoelectrons. The total current yield is shown to be sensitive to work function changes in the ± 11 meV range. This sensitivity is an order of magnitude lower than the total work function shift for the *h*-BN preparation on Rh(111). It is therefore a simple and reliable method to monitor surface processes. Apart from monitoring the growth of an atomic single layer, the setup also offers the opportunity to experimentally determine desorption energies of molecules on surfaces. This feature allows to better design CVD conditions or predict a layer coverage.

Furthermore, two possible routes have been investigated to further functionalize the produced *h*-BN samples. The first approach is to investigate the growth of thick *h*-BN films. The growth conditions and possible reaction mechanisms are identified and discussed. It is concluded that thick BN films may be grown on an arbitrary substrate. The produced BN films have a turbostratic ordering, i.e., they are disordered in the crystallographic z-direction. The second functionalization pathway involves the separation and transfer of the *h*-BN monolayer onto arbitrary substrates. With an electrochemical method it is possible to transfer up to 56 % of a monolayer and subsequent XPD measurements indicate the integrity of the transferred *h*-BN.

The four-inch *h*-BN monolayer on Rh(111) provides a basis to design a variety of devices, where functionality can be provided by the atomically thin *h*-BN layer. An example of such a device was realized in the Laboratory for Functional Polymers of Prof. Dr. F. Nüesch and is shown in Figure 38. It is an organic light emitting diode (OLED), which was directly evaporated on a *h*-BN/Rh(111) substrate. In this device, the boron nitride layer forms an ultimately thin protection layer against degradation or oxidation of the Rh electrode. Next generation devices may be combined with the *h*-BN monolayer transfer, not only to protect a bottom electrode, but also for

separation of all interfaces including the top surface to air.
Because of the low transfer rate of a *h*-BN monolayer, the thick film approach may bridge this gap. In combination with the electrochemical transfer setup, it may provide a source of transferable few layer *t*-BN. Such few layer boron nitride may be used in the devices proposed above or provide the basis for the first large area single crystalline *h*-BN thin films. It is known that *t*-BN experiences a phase transition to *h*-BN at temperatures around 1500 °C [51]. A transfer of *t*-BN films on Al_2O_3 substrates with subsequent annealing may trick the Volmer-Weber growth mode of crystalline *h*-BN on sapphire [53]. Al_2O_2 substrates are readily available and the Sinergia annealing system is estimated to reach and sustain such high temperatures. The single crystalline *h*-BN thin films would offer a variety of applications, among which one could investigate its application in an ultraviolet light emitting device [42].

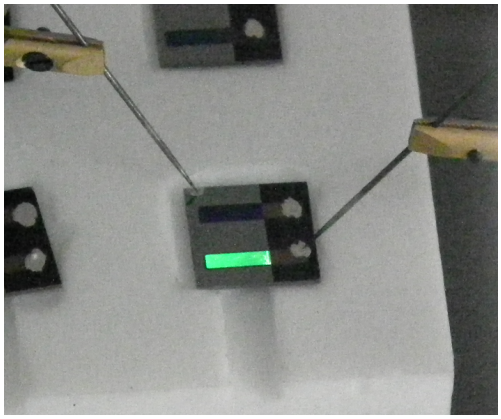

Figure 38: An organic light emitting diode based on the *h*-BN/Rh(111) substrate. The diode consists of a 8 nm semitransparent Ag top electrode, 100 nm tris(8-hydroxyquinolinato)aluminium (Alq_3) and the *h*-BN/Rh(111) as bottom electrode. The green light is characteristic for Alq_3. The diode was assembled with J.-N. Tisserant in the laboratory of Dr. R. Hany and Prof. Dr. F. Nüesch, EMPA Dübendorf.

7 Appendix

7.1 Thin Film Wafer Samples

The following considerations of the Rh thin film wafers used in the Sinergia chamber is adapted from reference [2], but provides an extended overview of their characteristics. Additional data are provided about the surface morphology, the temperature stability and about a gold contamination.

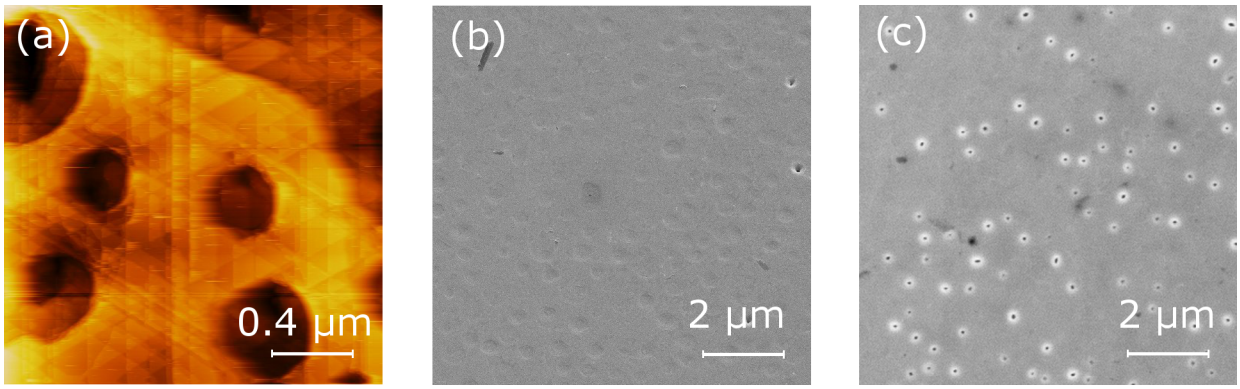

Figure 39: Morphology of the Rh thin film samples in the μm-regime as seen by different analysis instrumentation. The samples are all from the same wafer. (a) 2 μm field of view STM image, where the z piezo range is 9.4 nm. (b) 10 μm field of view He ion microscope image and (c) scanning electron microscope image.

The single crystalline Rh(111) thin films are grown on Si(111) wafers with an yttria-stabilized zirconia (YSZ) buffer layer [9]. The silicon wafer provides an inexpensive starting material, which is available with high quality and fits industrial standards. The mosaic spread of the oxide buffer layer is typically higher than 1°. Nevertheless, hetero-epitaxial metal films with excellent alignment, i.e., an angular spread of 0.1°-0.3°, can be obtained by applying a two-step growth process as described in detail by Gsell *et al.* [9]. Under these conditions, a certain minimum thickness is required before the initially isolated metal islands growing in Volmer-Weber mode coalesce and form a closed film. A thickness of 150 nm has been found as a good compromise to achieve a closed flat film. STM measurements reveal hole like surface features with a diameter of 0.25 μm as shown in Figure 39(a). Their depth is characteristic for each wafer and ranges from 1 to 5 nm and they also appear in the He ion image in Figure 39(b). We attribute these features to artifacts from the coalescence of islands. The scanning electron microscope (SEM) image in Figure 39(c) does not display these features, but detects "holes", which is in contradiction with the He ion microscope and STM measurements. We attribute this discrepancy to the lower surface sensitivity of the SEM and attribute the "holes" to very thin Rh film regions. Besides these holes, the epitaxial metal films show a large number of straight lines due to monoatomic steps. Their alignment is along three symmetry equivalent directions, which are visible in the STM image in Figure 39(a). They are attributed to slip lines caused by the plastic relaxation of strain that is induced by every temperature change due to differences in the coefficients of

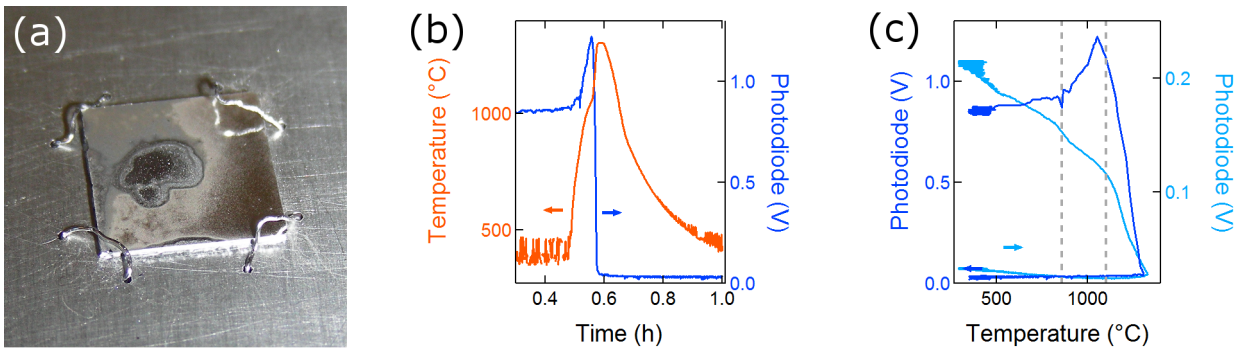

Figure 40: Mixing of rhodium with the silicon wafer. (a) thin film sample after exposures to temperature of about 1100 °C. (b) high temperature thin film stability experiment with temperature and photodiode signal from a sample reflected He Ne laser beam. (c) reflected laser beam intensity versus temperature for two different samples and different optical element configuration. The dotted lines are at temperatures, around which the reflected beam intensity experiences a kink, which is 860 °C and 1100 °C.

thermal expansion (CTEs) between the metal film and the substrate. Despite these slide lines, x-ray photoelectron diffraction (XPD) investigations on previously annealed and prepared samples indicate the conservation of the fcc lattice and the (111) orientation of the surface.

Rhodium, like many other transition metals, can react with silicon to form eutectic mixtures with strongly reduced melting points. In the case of copper thin films, this process is not suppressed by a YSZ buffer layer [80]. The assessment of the Rh(111)/YSZ/Si(111) stability had been accomplished by laser reflection experiments at high temperature and is shown in Figure 40. It was found that samples from different wafers behave differently. While some samples show a clear reflection reduction signal at a distinct temperatures, others may display a rather linear reflection decrease as displayed in Figure 40(c). This can be explained by an inhomogeneous sample destruction, which is visible in the surface domains of the destroyed sample in Figure 40(a). Nevertheless, reflection intensity kinks seem to appear at temperatures of 860 °C and 1100 °C. To enhance the temperature stability of the Rh thin films, a procedure for thicker YSZ layers had been developed by the Schreck group, Universität Augsburg. Recently, it was reported for Ir/YSZ/Si(111) that an increase of the YSZ film thickness to 100 nm guaranteed a stability of the whole layer system above 1000 °C [81].

An additional problem appeared, when the Rh target for the Rh thin film deposition was changed. The new targets were identified to be gold contaminated, which led to Rh thin films, where the XPS revealed an Au:Rh ratio of 5 %. SEM images revealed a dot like Au distribution as shown in Figure 41(a), but a thin layer may not be excluded, due to the detection limit. The first strategy to remove the Au contamination was thermal desorption, which is shown in Figures 41(b) and (c). A clean 9 mm x 9 mm sample had been installed above the gold contaminated wafer, which was kept at 900 °C for 1 h. XPS measurements on this small sample revealed a new Au contamination after the experiment, which meant that thermal Au desorption is a valuable option for the Au removal. It also meant that the Au contamination has to be located at the sample surface or transported

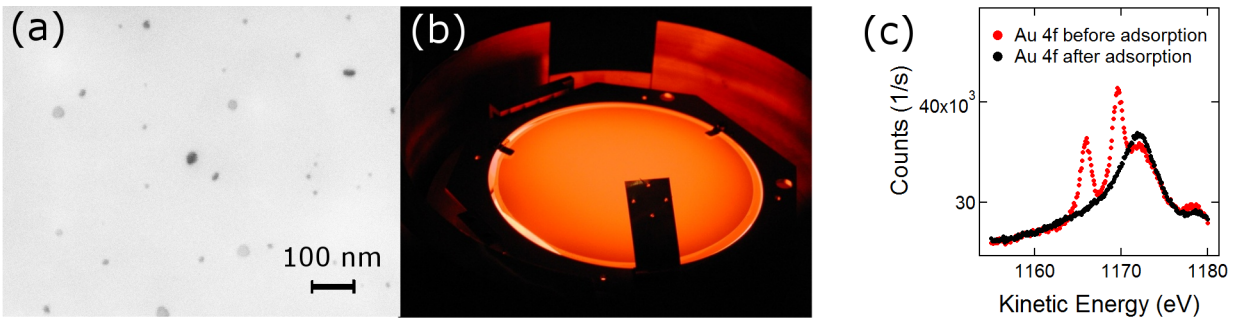

Figure 41: Gold contamination in the Rh thin film wafers. (a) displays a false color SEM image of an Au contaminated Rh thin film sample. The image had been recorded while the energy-dispersive x-ray analyzer (EDX) was close to the sample, which reduces surface contrast contrast, but identifies the black dots as as Au contamination. (b) displays a thermal Au desorption experiment with a small and clean Rh thin film sample mounted above as detection platform. (c) XPS analysis of this small sample before and after Au adsorption. The broad peak is a feature of Rh.

to the surface at high temperatures. Therefore, it is possible to remove the Au contamination with the four inch sputter option in the Sinergia entry lock (see section 2.1).
In 2013, the Au contamination could be reduced to an Au:Rh ratio of 0.38 % by the application of a new Rh target for the thin film deposition and the introduction of the Sinergia sputtering system. Additional annealing and sputtering cycles of such samples could even further reduce the Au contamination below the XPS detection limit. Importantly, an Au contamination of 0.38 % was low enough to grow the *h*-BN nanomesh on the Rh thin films with neither influencing LEED patterns nor UPS features.

7.2 Ellipsometry

Ellipsometry to monitor the atomic single layer growth suffers from instabilities on long (in the hour range) as well on short terms (in the minute range). The long term instability makes it impossible to perform a simple and short in-situ experiment and it is mainly caused by a temperature increase of the viewports. The short term instabilities are caused by the current reading units (Keithley 2100), which appear to be sensitive to power net fluctuations at their lowest current recording range.

Figure 42 gives an overview of the activities to reduce the window effects on the laser light. From a physical point of view, it is stress induced birefringence, which can explain the findings. As displayed in Figure 42(a), the preparation introduced in section 3.2.3 heats up the windows to 35 °C and the diode signal shift about 10 %. Simple heating of only one of the BK7 standard windows could already explain a 5 % signal shift. These shifts are more than an order of magnitude larger than the identified signals from the single atomic layer in the 0.1 – 0.2 % range. The birefringence effects are more pronounced with the Al_2O_3 window. Although the effects seem to be more linear than for the BK7 window, they are an order of magnitude larger and displayed in Figure 42(b). Instead of trying to correct the temperature effects with a window temperature recording (Figure 42(c)), heat shields (Figure 42(d)) are implemented as well as stress free and flange decoupled fused silica windows.

The short term instabilities of the system are sudden current shifts, which are recorded by either

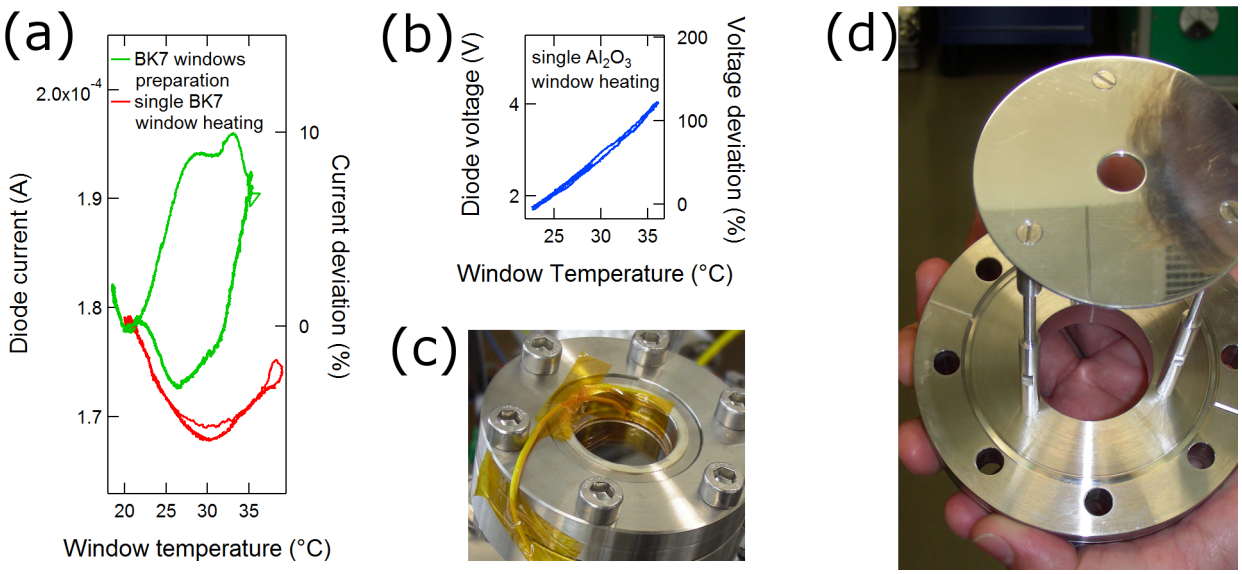

Figure 42: Thermally induced optical effects of the viewports. (a) displays the normalized diode signal for the boron nitride preparation in Figure 18 and the same signal, if only one window is annealed. (b) shows light reflection for the case of annealing a single Al_2O_3 window. Here, the diode recording was accomplished with the voltage amplifier of G. Landolt [30]. (c) displays the Kapton fixed thermocouple for the temperature readings and (d) is the implemented heat shield, which reduced window heating from direct heater radiation.

both or only one of the photodiodes and occur in a time interval of about 34 min. These shifts are in the order of 0.1 – 0.2 % which corresponds to the measured amplitudes of a surface signal as shown in section 3.2.3. Figure 43 gives an overview of the identification attempts of these signal current shifts. From Figure 43(a) it cannot be excluded that laser mode hopping is the reason for the signal shifts. The short circuit multimeters in Figure 43(c) clearly identify themselves to be the source of the current hopping, because it is possible to induce a phase shift between the two multimeter hops, if they are powered by different power line phases. This indicates that a fluctuating power line might be the reason for the multimeter to measure those current shifts. Attempts to reduce them by passive power line filters were not successful.
A simple solution to this problem is the employment of more powerful measuring units. But the removal of those artificial signal shifts might not be the solution to all problems, because exactly the same shifts might also be induced by a laser mode hopping as recorded in Figure 43(a).

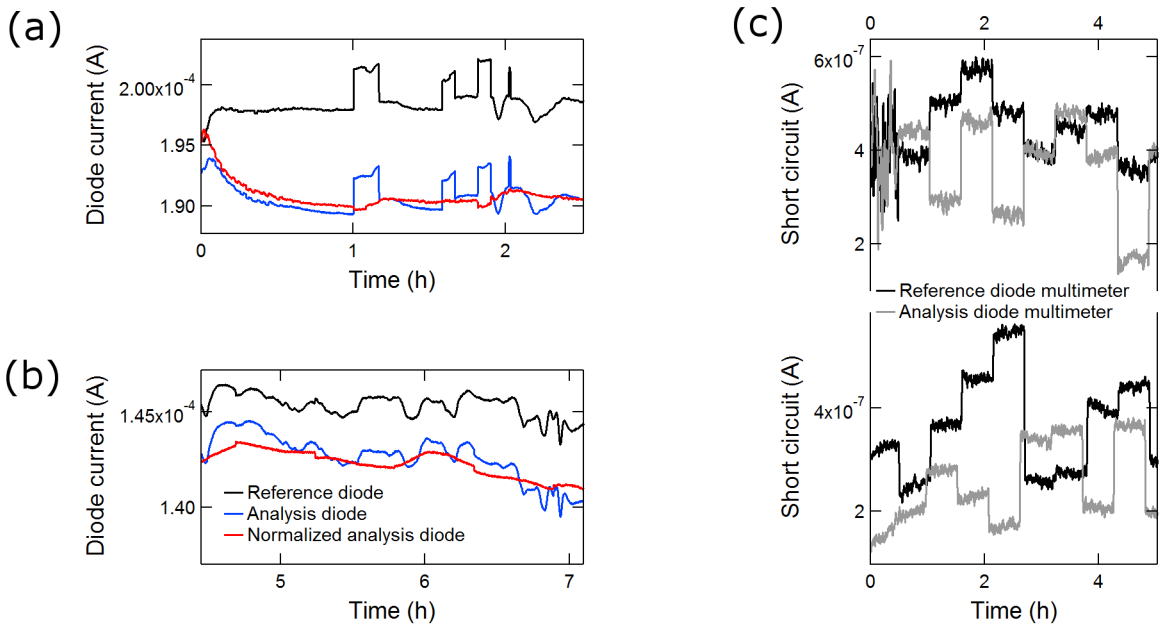

Figure 43: Overview of the sudden signal current shifts. (a) displays four different laser mode hopping events, which were excited by a magnet on the laser tube. Only the third event could create a sudden current shift in the normalized analysis diode current, which means that laser mode hopping could be one origin of these shifts. (b) is a photo diode measurement, where the laser beam passed a Faraday isolator, which blocks laser light reflection back into the laser tube. This setup excludes laser back reflection to be the source of the sudden shifts, because they still occur. (c) displays current measurements of the short circuit digital multimeters, which were used to measure the diode current. The sudden signal shifts appear even without laser light and they are clearly an artifact of the powering network, because they occur exactly synchronized in case of both multimeter connected to the same phase power line (upper part). But they are phase shifted by 4.74(8) min, if the multimeter are on different power line phases (lower part).

7.3 Pulsed Ultraviolet Light Source

7.3.1 In-situ Electron Current Measurements

In order to probe a surface reaction with an in-situ measurement, an excitation of the system is always required. These excitations may change the reaction condition and influence the measurement itself. The UV lamp setup measures photoelectrons, which may interact with a CVD reaction.

Figure 44(a) displays a current measurement with an electrode during a boron nitride preparation in the Sinergia chamber. The electrode was biased with a 9 V battery and it was intended to detect a possible thermionic emission change during borazine dosing. It turns out that oxygen as well as borazine produce such a large amount of charges that the electrode detects a constant current instead of a current evolution during the dosing events.

The origin of charges in the reaction chamber during the application of borazine is assessed in Figure 44(b). An electrode current at variable bias is measured during the application of $5 \cdot 10^{-7}$ mbar borazine, while a molybdenum wafer was either hot (about 850 °C) or at room temperature (RT) and the mass spectrometer running or turned off. The measurements at zero bias reveal that no significant currents can be measured, independent of the sample temperature. This means no excess charge is generated by borazine in the reaction chamber, which is in contrast to measurements with a running mass spectrometer. In this case, currents in the order of 40 pA are measured through the electrode on the chamber wall potential, which may explain the current polarization change in Figure 44(a).

It is concluded that the mass spectrometer ionization unit, does influence the gas charge in the reaction chamber during borazine application. In addition, the interaction of borazine with a hot

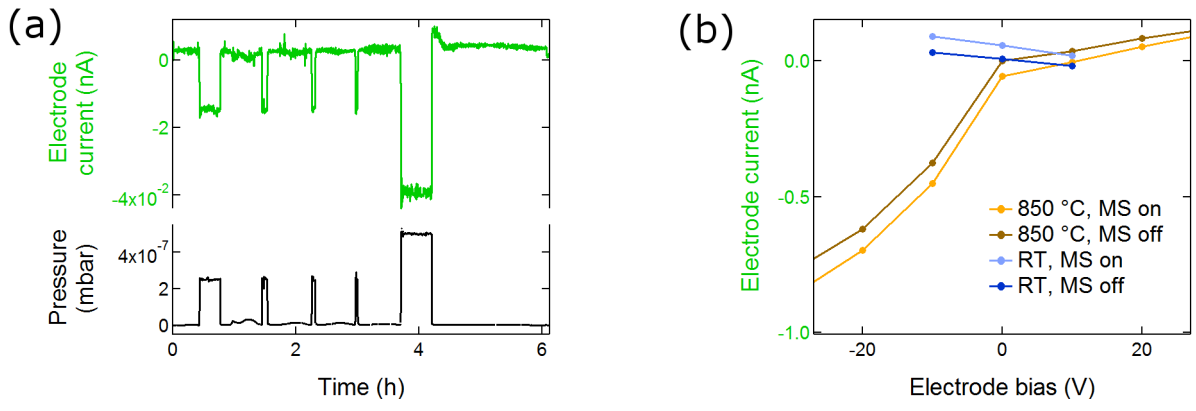

Figure 44: Gas, sample temperature, mass spectrometer and electrode bias effects for in-situ electron yield measurements. (a) displays the electrode current during a *h*-BN preparation on a rhodium four inch wafer. The electrode bias was +9 V and it records a significant current with polarization change during the five dosing events. (b) compares electrode currents at $5 \cdot 10^{-7}$ mbar borazine for a room temperature (RT) and a hot (850 °C) molybdenum wafer. During these measurements, the mass spectrometer had been turned on and off.

sample also shows a similar effect on the reaction gas. So far, these effects are not observed to influence a CVD reaction, but they might distort current measurements with the UV flash lamp. Section 7.3.2 assesses this effects.

7.3.2 Current Response of the Photoelectron Yield Setup

From the considerations in the previous section, it is expected to be difficult to monitor a surface process in-situ via charged particles. A running mass spectrometer, thermionic emission from the hot sample or the reaction gas itself may provide charges, which distort a photoelectron measurement.
The application of a pulsed excitation source allows to distinguish a surface current from the current effects identified in section 7.3.1. Figure 45 displays a disentanglement from different effects, such as the current attenuation by an inert gas or a background current during a reaction. The background current is here, the electrode current, which proceeds the the UV pulse current.

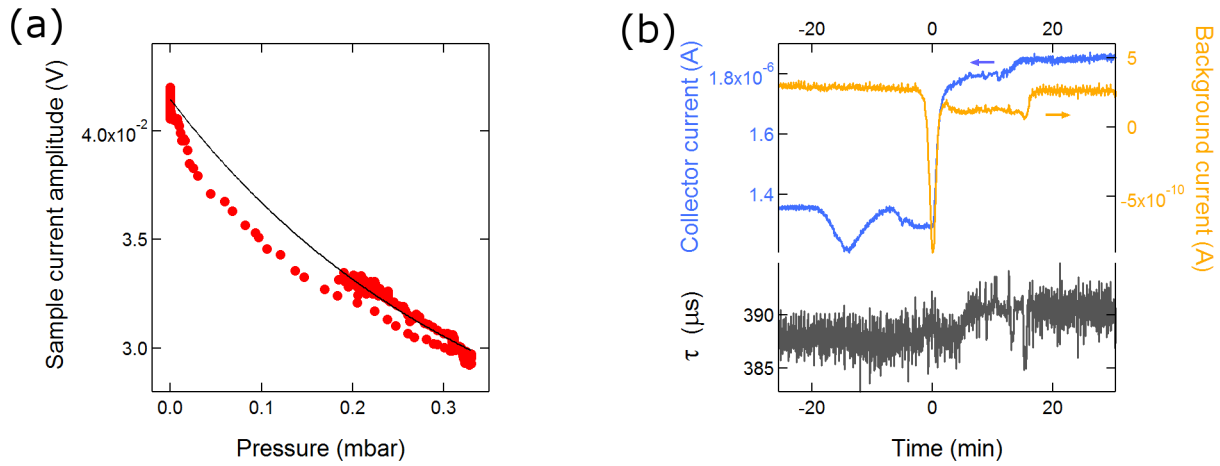

Figure 45: Electron yield signal response at high pressures and with reactive gases. (a) displays the photocurrent signal attenuation of the sample current with argon pressures up to 0.32 mbar. The fitted exponential function ($I_{Ph} \propto e^{-p/p_0}$) reveals an attenuation of $p_0 = 0.34$ mbar. (b) shows the electron current signal for the *h*-BN preparation in ESCA, which is found in section 3.3.2 in Figure 22(a). The (**collector current**) is a measure for the UV pulse response, while the (**background current**) is the antenna current prior to the UV pulses. The exponential decay (τ) of the current signal is constant within the microsecond regime.

The beginning of the borazine dosing event in Figure 45(a) is given by the collector current increase at time zero. At this time, a background current spike is recorded, which is in line with the findings in Figure 44(b), where borazine and a hot sample induces an electrode current. Note that time-dependent current response with the mass spectrometer turned off is not measured in section 7.3.1. The current spike might be related to different phenomena such as thermionic emission or surface reaction charge excess, but it is clearly separable and orders of magnitudes smaller than the UV photocurrent.

7.4 Mathematical Considerations for the Gas Temperature Profiles

In this section, the mathematical procedure is elucidated, which leads to temperature profiles as described in section 4.3.5. In the high pressure regime, the general thermal diffusion equation (52) has to be solved. This differential equation is given in expression (55) for a constant κ and in the steady state situation. It is still the general three dimensional form of the differential equation, where $\dot{q}$ is a volumetric heat source in units of $\mathrm{W/m^3}$ [67].

$$\nabla^2 T + \frac{\dot{q}}{\kappa} = 0 \tag{55}$$

To reduce dimensions, we introduce spherical coordinates in equation (55). The corresponding Laplacian operator is applied here in equation (56).

$$\frac{1}{r^2}\frac{\partial}{\partial r}(r^2\frac{\partial T}{\partial r}) + \frac{1}{r^2 sin(\theta)}\frac{\partial}{\partial \theta}(sin(\theta)\frac{\partial T}{\partial \theta}) + \frac{1}{r^2 sin^2(\theta)}\frac{\partial^2 T}{\partial \Phi^2} + \frac{q(r_1)}{\kappa} = 0 \tag{56}$$

We assume a complete spherical evolution of the heat profile, which approximates the real preparation chamber situation. With this assumption, the temperature profile does no longer depend on the angles, but only on the radius r. With this trick, the dimensionality is reduced to a single dimension and the homogeneous differential equation is given in equation (57).

$$\frac{d}{dr}(r^2\frac{dT}{dr}) = 0 \tag{57}$$

Integrating this expression in the dimension r yields a general function with the two undetermined constants C_1 and C_2.

$$T(r) = \frac{C_1}{r} + C_2 \tag{58}$$

With two boundary conditions the constants C_1 and C_2 can be determined. Although both, the sample and the chamber wall temperature are known, the gas temperature above them might be considerably different. The temperature of the chamber wall is measured by a thermocouple, which is had no direct physical contact to the wall. In thermal equilibrium, this thermocouple measures a temperature close to the chamber wall, which yields an estimate of the gas temperature. After 46 min of at high preparation pressures, the measurement did well level at 50 °C, which is used as one of the boundary conditions for equation (58). As second boundary condition, the temperature of the sample is carefully avoided, because of its unknown energy transfer efficiency to argon. Instead, the additional power to keep the sample at the same temperature can experimentally be determined. This additional power heats the reaction gas and leads to a non constant temperature profile. Equations (59) and (60) express the two boundary conditions for the general solution in equation (58).

$$q(r_1) = q_1 = -\kappa\frac{dT}{dr} = \kappa\frac{C_1}{r_1^2} \tag{59}$$

$$T(r_2) = \frac{C_1}{r_2} + C_2 = \frac{q_1 r_1^2}{\kappa r_2} + C_2 \tag{60}$$

Here, the constant C_1 can be determined only with equation (59) and its solution is already used in equation (60). It is straight forward to determine the second constant C_2, which leads to the solution in equation (54).

7.5 Technical Drawings

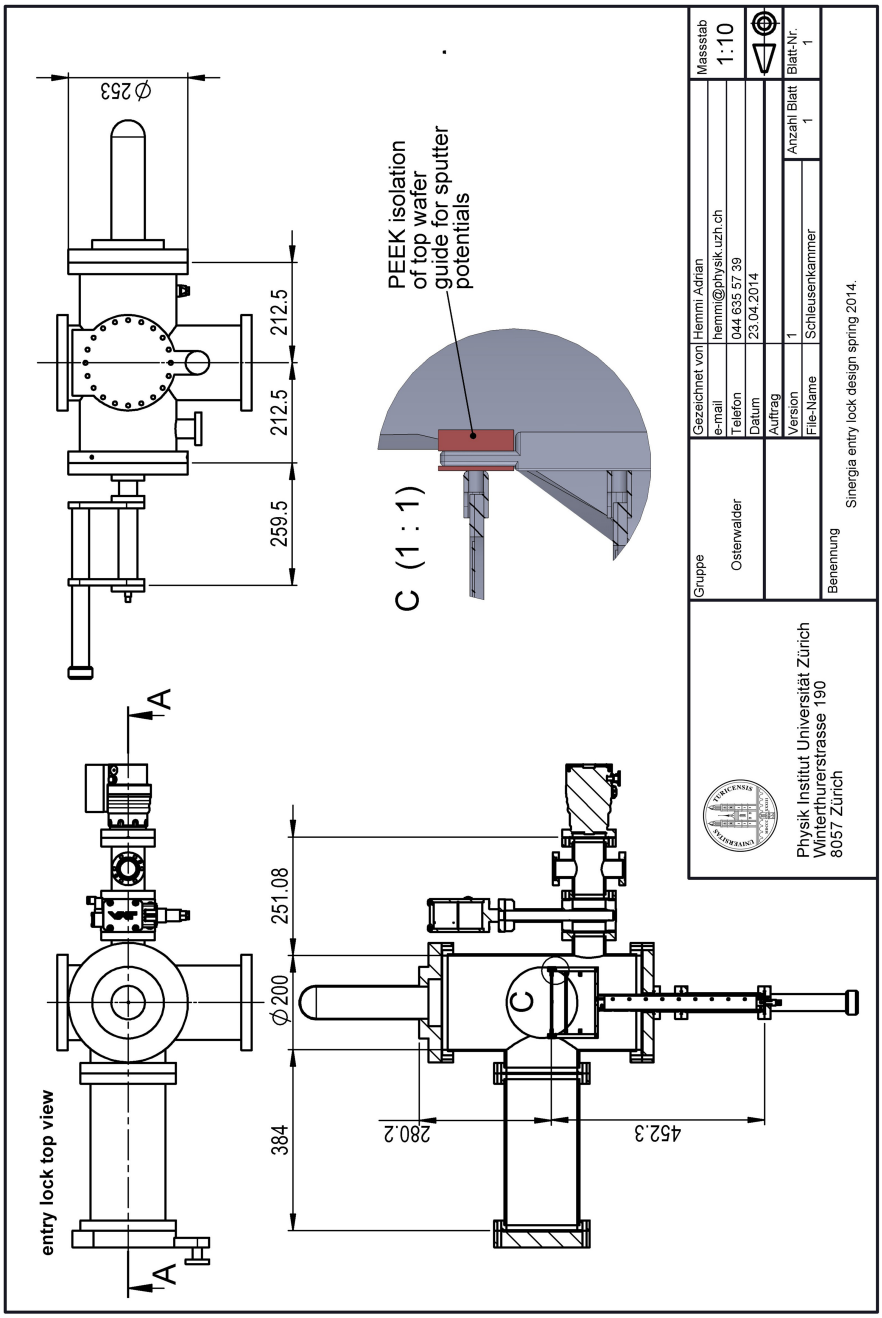

Figure 46: Detailed plan of the Sinergia entry lock.

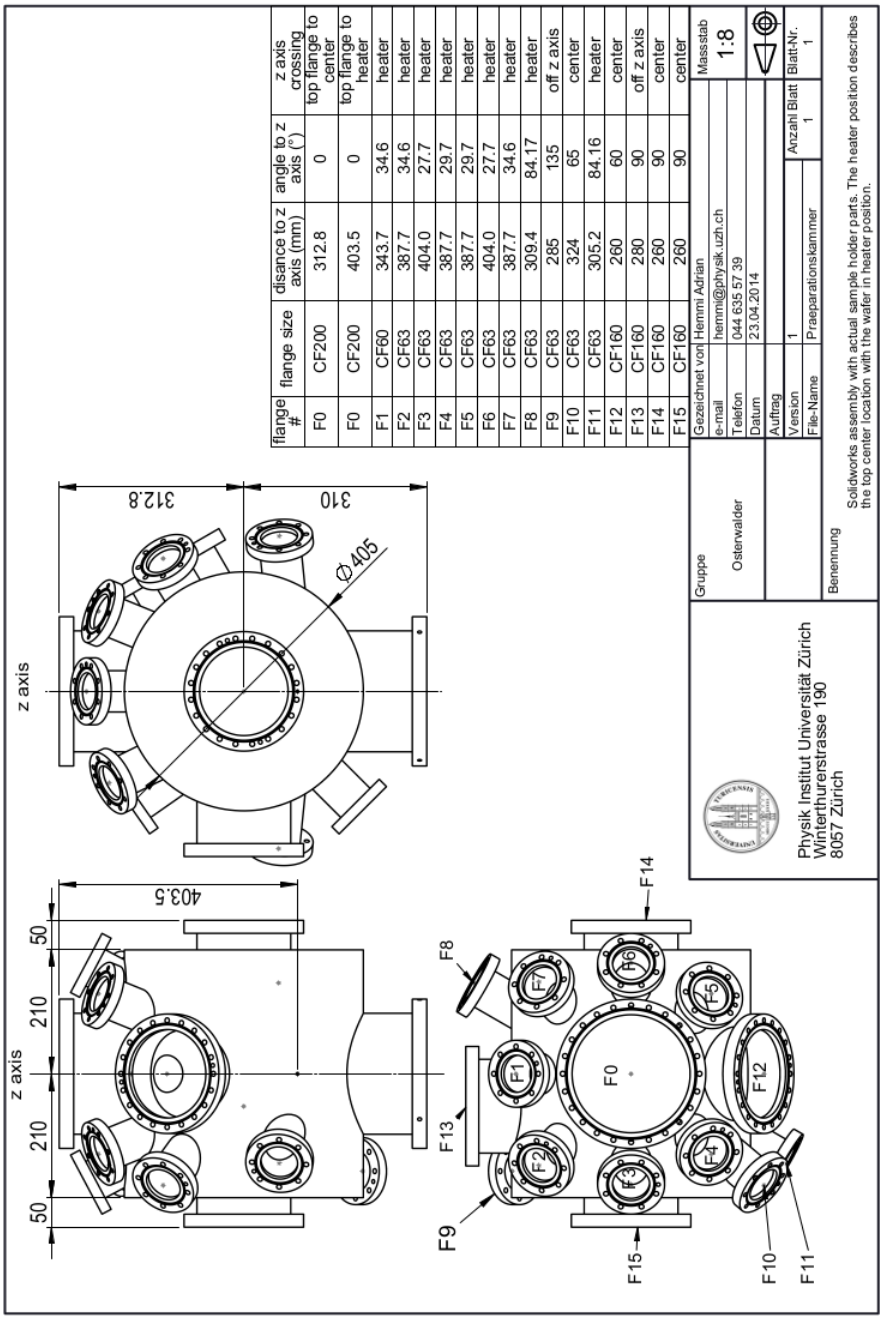

flange #	flange size	disance to z axis (mm)	angle to z axis (°)	z axis crossing
F0	CF200	312.8	0	top flange to center
F0	CF200	403.5	0	top flange to heater
F1	CF60	343.7	34.6	heater
F2	CF63	387.7	34.6	heater
F3	CF63	404.0	27.7	heater
F4	CF63	387.7	29.7	heater
F5	CF63	387.7	29.7	heater
F6	CF63	404.0	27.7	heater
F7	CF63	387.7	34.6	heater
F8	CF63	309.4	84.17	heater
F9	CF63	285	135	off z axis
F10	CF63	324	65	center
F11	CF63	305.2	84.16	heater
F12	CF160	280	60	center
F13	CF160	280	90	off z axis
F14	CF160	260	90	center
F15	CF160	260	90	center

Figure 47: Detailed plan of the Sinergia preparation and analysis chamber, which are identical. The flange distances were measured from the center of the top plane o each flange (small gray dots).

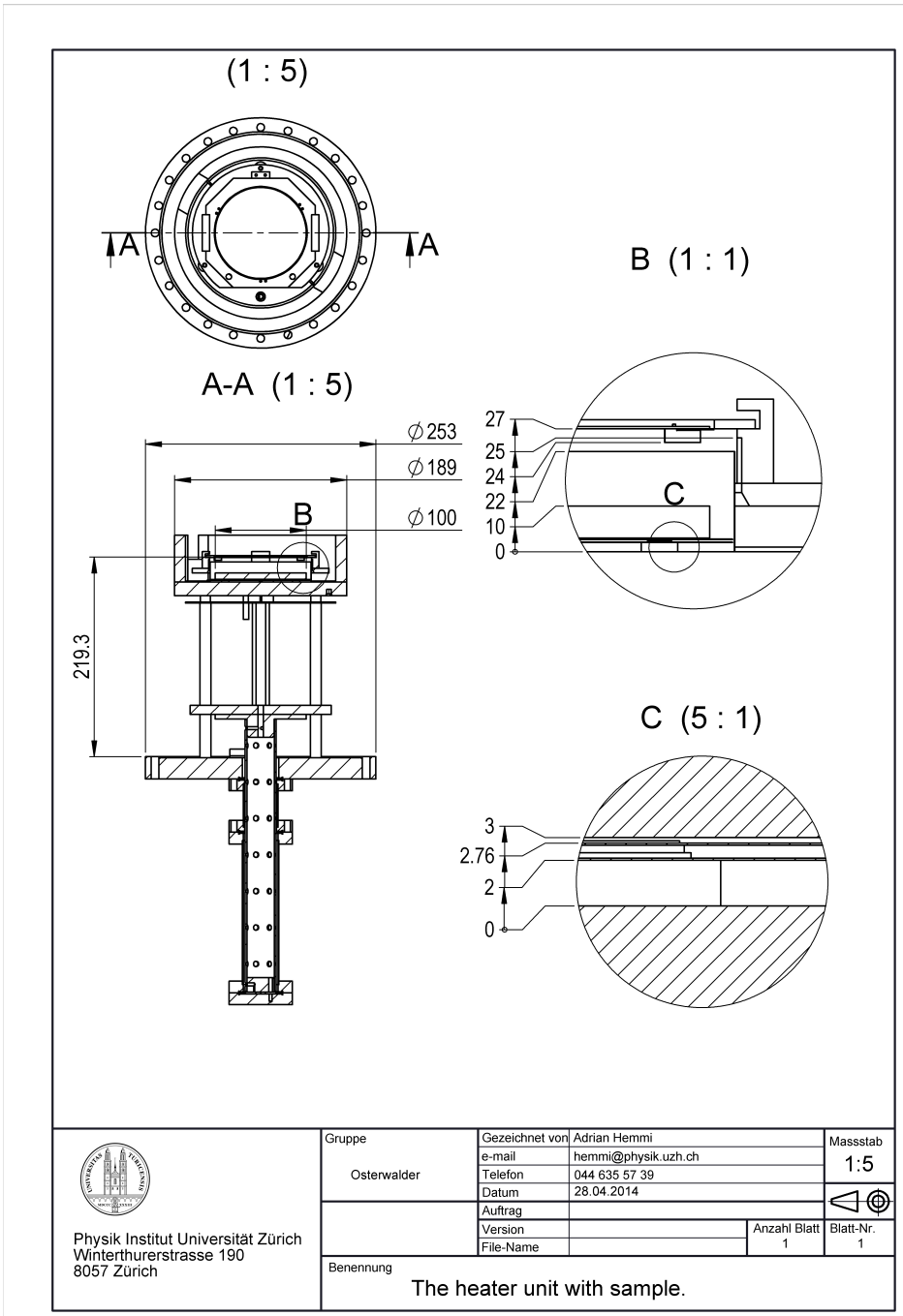

Figure 48: Detailed plan of the Sinergia heater. The details B and C reveal the very tight space design for its lower shields.

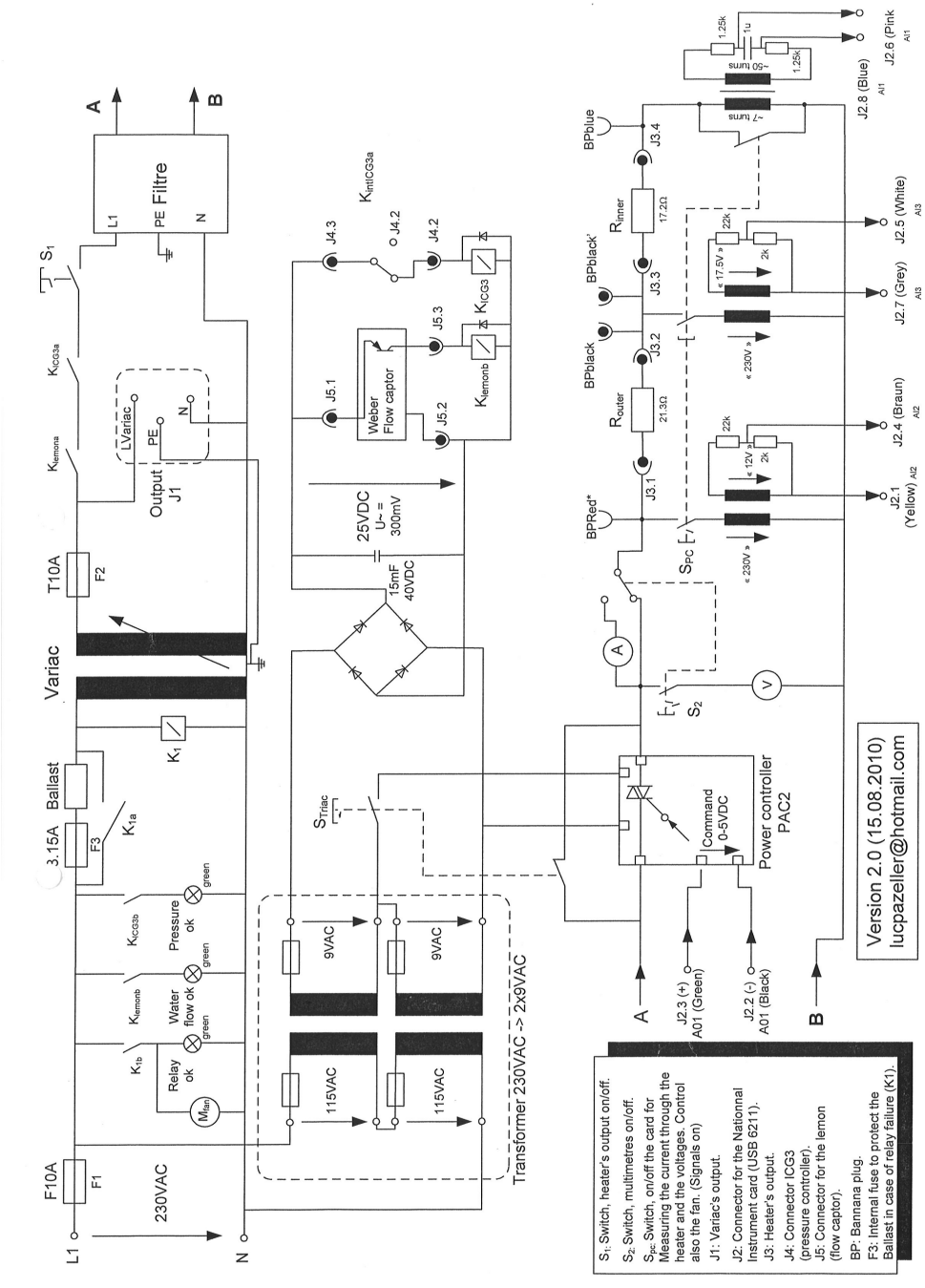

Figure 49: Electronic plan of the heater assembly from Luc Pazeller.

References

[1] M. Corso, W. Auwärter, M. Muntwiler, A. Tamai, T. Greber, and J. Osterwalder, *Boron Nitride Nanomesh*, Science **303**, 217 (2004).

[2] A. Hemmi, C. Bernard, H. Y. Cun, S. Roth, M. Klöckner, T. Kälin, M. Weinl, S. Gsell, M. Schreck, J. Osterwalder, and T. Greber, *High Quality Single Atomic Layer Deposition of Hexagonal Boron Nitride on Single Crystalline Rh(111) Four-Inch Wafers*, Rev. Sci. Instrum. **85**, 035101 (2014).

[3] A. Hemmi, H. Cun, S. Roth, J. Osterwalder, and T. Greber, *Low Cost Photoelectron Yield Setup for Surface Process Monitoring*, J. Vac. Sci. Technol. A **32(2)**, 023202 (2014).

[4] S. Berner, M. Corso, R. Widmer, O. Groening, R. Laskowski, P. Blaha, K. Schwarz, A. Goriachko, H. Over, S. Gsell, M. Schreck, H. Sachdev, T. Greber, and J. Osterwalder, *Boron Nitride Nanomesh: Functionality from a Corrugated Monolayer*, Angew. Chem. Int. Ed. **46**, 5115 (2007).

[5] H. Dil, J. Lobo-Checa, R. Laskowski, P. Blaha, S. Berner, J. Osterwalder, and T. Greber, *Surface Trapping of Atoms and Molecules with Dipole Rings*, Science **319**, 1824 (2008).

[6] R. Widmer, S. Berner, O. Groening, T. Brugger, J. Osterwalder, and T. Greber, *Electrolytic in situ STM Investigation of h-BN-Nanomesh*, Electrochem. Commun. **9**, 2484 (2007).

[7] L. Song, L. Ci, H. Lu, P. B. Sorokin, C. Jin, J. Ni, A. G. Kvashnin, D. G. Kvashnin, J. Lou, B. I. Yakobson, and P. M. Ajayan, *Large Scale Growth and Characterization of Atomic Hexagonal Boron Nitride Layers*, Nano Lett. **10**, 3209 (2010).

[8] X. Li, W. Cai, J. An, S. Kim, J. Nah, D. Yang, R. Piner, A. Velamakanni, I. Jung, E. Tutuc, S. K. Banerjee, L. Colombo, and R. S. Ruoff, *Large-Area Synthesis of High-Quality and Uniform Graphene Films on Copper Foils*, Science **324**, 1312 (2009).

[9] S. Gsell, M. Fischer, M. Schreck, and B. Stritzker, *Epitaxial Films of Metals from the Platinum Group (Ir, Rh, Pt and Ru) on YSZ-buffered Si(111)*, J. Cryst. Growth **311**, 3731 (2009).

[10] O. Bunk, M. Corso, D. Martoccia, R. Herger, P. R. Willmott, B. D. Patterson, J. Osterwalder, J. F. van der Veen, and T. Greber, *Surface X-ray Diffraction Study of Boron-Nitride Nanomesh in Air*, Surf. Sci. **601**, L7 (2007).

[11] R. Laskowski, P. Blaha, T. Gallauner, and K. Schwarz, *Single-Layer Model of the Hexagonal Boron Nitride Nanomesh on the Rh(111) Surface*, Phys. Rev. Lett. **98**, 106802 (2007).

[12] T. Dienel, J. Gómez-Díaz, A. P. Seitsonen, R. Widmer, M. Iannuzzi, K. Radican, H. Sachdev, K. Müllen, J. Hutter, and O. Gröning, *Dehalogenation and Coupling of a Polycyclic Hydrocarbon on an Atomically Thin Insulator*, ACS Nano **8**, 6571 (2014).

[13] M. Iannuzzi, F. Tran, R. Widmer, T. Dienel, K. Radican, Y. Ding, J. Hutter, and O. Gröning, *Site-selective Adsorption of Phthalocyanine on h-BN/Rh(111) Nanomesh*, Phys. Chem. Chem. Phys. **16**, 12374 (2014).

[14] H. Cun, M. Iannuzzi, A. Hemmi, S. Roth, J. Osterwalder, and T. Greber, *Immobalizing Individual Atoms beneath a Corrugated Single Layer of Boron Nitride*, Nano Lett. **13**, 2098 (2013).

[15] H. Cun, M. Iannuzzi, A. Hemmi, J. Osterwalder, and T. Greber, *Implantation Length and Thermal Stability of Interstitial Ar Atoms in Boron Nitride Nanotents*, ACS Nano **8**, 1014 (2014).

[16] H. Cun, M. Iannuzzi, A. Hemmi, J. Osterwalder, and T. Greber, *Two-Nanometer Voids in Single-Layer Hexagonal Boron Nitride: Formation via the "Can-Opener" Effect and Annihilation by Self-Healing*, ACS Nano **8**, 7423 (2014).

[17] S. Muff, *Kontaktwinkelmessung und Elektrochemie mit 0.1 M $HClO_4$ auf h-BN/Rh(111) Nanomesh*, Bachelor thesis at University of Zurich (2011).

[18] M. Graf, *Towards Controlled Surface Functionalisation of Hexagonal Boron Nitride on the Four-Inch Scale*, Bachelor thesis at University of Zurich (2014).

[19] S. A. Komolov and L. T. Chadderton, *Total Current Spectroscopy*, Surf. Sci. **90**, 359 (1979).

[20] T. Brugger, *Graphene and Hexagonal Boron Nitride on Transition Metals and Their Application*, PhD thesis at University of Zurich (2010).

[21] G. Dong, E. B. Fourre, F. C. Tabak, and J. W. M. Frenken, *How Boron Nitride Forms a Regular Nanomesh on Rh(111)*, Phys. Rev. Lett. **104**, 096102 (2010).

[22] S. Roth, *Graphene on Metal Surfaces and Hexagonal Boron Nitride*, PhD thesis at University of Zurich (2013).

[23] Y. Gong et al., *Direct Chemical Conversion of Graphene to Boron- and Nitrogen- and Carbon-Containing Atomic Layers*, Nat. Commun. **5**, 3193 (2014).

[24] W. Auwärter, *One Monolayer of Hexagonal Boron Nitride on Ni(111): an Atomically Sharp Interface*, PhD thesis at University of Zurich (2003).

[25] P. Sutter, J. Lahiri, P. Albrecht, and E. Sutter, *Chemical Vapor Deposition and Etching of High-Quality Monolayer Hexagonal Boron Nitride Films*, ACS Nano **5**, 7303 (2011).

[26] T. Greber, O. Raetzo, T. J. Kreutz, P. Schwaller, W. Deichmann, E. Wetli, and J. Osterwalder, *A Photoelectron Spectrometer for k-Space Mapping above the Fermi Level*, Rev. Sci. Instrum. **68**, 4549 (1997).

[27] E. Bauer, *LEEM Basics*, Surf. Rev. Lett. **5**, 1275 (1998).

[28] J. J. Harris and B. A. Joyce, *Oszillations in the Surface Structure of Sn-Doped GaAs during Growth by MBE*, Surf. Sci. **103**, 90 (1981).

[29] H. H. Rotermund, W. Engel, S. Jakubith, A. von Oertzen, and G. Ertl, *Methods and Application of UV Photoelectron Microscopy in Heterogeneous Catalysis*, Ultramicroscopy **36**, 164 (1991).

[30] G. Landolt, *In-situ Surface Magneto-Optic Kerr Effect Setup for the Spin - and Angle Resolved Photoemission Experiment COPHEE*, Master thesis (2010).

[31] D. P., *Lehrbuch der Optik*, Leipzig Verlag von S. Hirzel (1900).

[32] H. J. Eichler, H. Gobrecht, M. Krystek, H. Niedrig, M. Richter, H. Schoenebeck, H. Weber, and K. Weber, *Lehrbuch der Experimentalphysik, Band III, Optik, 8. Auflage*, Leipzig Verlag von S. Hirzel (1978).

[33] E. D. Palik, *Handbook of Optical Constant of Solids*, Academic Press, Boston (1985).

[34] H. G. Tompkins, *Handbook of Ellipsometry*, Springer (2005).

[35] P. S. Hauge and F. H. Dill, *A Rotating-Compensator Fourier Ellipsometer*, Opt. Commun. **14**, 431 (1975).

[36] H. B. Michaelson, *The Work Function of the Elements and Its Periodicity*, J. Appl. Phys. **48**, 4729 (1977).

[37] S. Hüfner, *Photoelectron Spectroscopy*, Springer Series in Solid-State Sciences 82 (1995).

[38] S. Roth, F. Matsui, T. Greber, and J. Osterwalder, *Chemical Vapor Deposition and Characterization of Aligned and Incommensurate Graphene/Hexagonal Boron Nitride Heterostack on Cu(111)*, Nano Lett. **13**, 2668 (2013).

[39] S. G. Lias, *Ionization Energy Evaluation*, page 20899, NIST Chemistry WebBook.

[40] A. S. Goossens, D. S. C. M., T. A. Baart, K. Watanabe, T. Taniguchi, and M. K. Vandersypen, *Gate-Defined Confinement in Bilayer Graphene-Hexagonal Boron Nitride Hybrid Devices*, Nano Lett. **12**, 4656 (2012).

[41] W. Gannett, W. Regan, K. Watanabe, T. Taniguchi, M. F. Crommie, and A. Zettl, *Boron Nitride Substrates for High Mobility Chemical Vapor Deposited Graphene*, Appl. Phys. Lett. **98**, 242105 (2011).

[42] K. Watanabe, T. Taniguchi, T. Niiyama, K. Miya, and M. Taniguchi, *Far-Ultraviolet Plane-Emission Handheld Device Based on Hexagonal Boron Nitride*, Nature Photon. **3**, 591 (2009).

[43] A. Nagashima, N. Tejima, Y. Gamou, T. Kawai, and C. Oshima, *Electronic Dispersion Relations of Monolayer Hexagonal Boron Nitride Formed on the Ni(111) Surface*, Phys. Rev. B **51**, 4606 (1995).

[44] A. Nagashima, N. Tejima, Y. Gamou, T. Kawai, and C. Oshima, *Electronic Structure of Monolayer Hexagonal Boron Nitride Physisorbed on Metal Surfaces*, Phys. Rev. Lett. **75**, 3918 (1995).

[45] A. Preobrajenski, M. Nesterov, M. L. Ng, A. Vinogradov, and N. Martensson, *Monolayer h-BN on Lattice-Mismatched Metal Surfaces: On the Formation of the Nanomesh*, Chem. Phys. Lett. **446**, 119 (2007).

[46] T. Takahashi, H. Itoh, and A. Takeuchi, *Chemical vapor deposition of hexagonal boron nitride thick film on iron*, J. Cryst. Growth **47**, 245 (1979).

[47] M. Sano and M. Aoki, *Chemical Vapour Deposition of Thin Films of {BN} onto Fused Silica and Sapphire*, Thin Solid Films **83**, 247 (1981).

[48] Y. Shi, C. Hamsen, X. Jia, K. K. Kim, A. Reina, M. Hofmann, A. L. Hsu, K. Zhang, H. Li, Z. Y. Juand, M. S. Dresselhaus, L. J. Li, and J. Kong, *Synthesis of Few-Layer Hexagonal Boron Nitride Thin Film by Chemical Vapor Deposition*, Nano Lett. **10**, 4134 (2010).

[49] C. Oshima and A. Nagashima, *Ultra-thin Epitaxial Films of Graphite and Hexagonal Boron Nitride on Solid Surfaces*, J. Phys.: Condens. Mater **9**, 64931 (1997).

[50] T. Matsuda, N. Uno, and H. Nakae, *Synthesis and Structure of Chemically Vapour-Deposited Boron Nitride*, J. Mater. Sci. **21**, 648 (1986).

[51] J. J. Thomas, N. E. Weston, and T. E. O'Connor, *Turbostratic Boron Nitride, Thermal Transformation to Ordered-layer-lattice Boron Nitride*, Am. Chem. Soc. **84**, 4619 (1963).

[52] J. Kouvetakis, V. V. Patel, C. W. Miller, and D. B. Beach, *Composition and Strucutre of Boron Nitride Films Deposited by Chemical Vapor Deposition from Broazine*, J. Vac. Sci. Tech. A **8**, 3929 (1990).

[53] Y. Kubota, K. Watanabe, O. Tsuda, and T. Taniguchi, *Deep Ultraviolet Light-Emitting Hexagonal Boron Nitride Synthesized at Atmospheric Pressure*, Science **317**, 932 (2007).

[54] J. J. Yeh and I. Lindau, *Atomic Subshell Photoionization Cross Sections and Asymmetry Parameters: $1 \leq Z \leq 103$*, At. Data Nucl. Data Tables **32**, 1 (1985).

[55] L. T. Weng, G. Vereecke, M. J. Genet, P. Bertrand, and W. E. E. Stone, *Quantitative XPS. Part I: Experimental Determination of the Relative Analyser Transmission Function of two Different Spectrometers – a Critical Assessment of Various Methods, Parameters Involved and Errors Introduced*, Surf. Interface Anal. **20**, 179 (1993).

[56] S. Tanuma, C. J. Powell, and D. R. Penn, *Calculations of Electron Inelastic Mean Free Paths for 31 Materials*, Surf. Interface Anal. **11**, 577 (1988).

[57] S. Tanuma, C. J. Powell, and D. R. Penn, *Calculations of Electron Inelasic Mean Free Paths*, Surf. Interface Anal. **17**, 911 (1991).

[58] R. W. Lynch and H. G. Drickamer, *Effect of High Pressure on the Lattice Parameters of Diamond, Graphite, and Hexagonal Boron Nitride*, J. Chem. Phys. **44**, 2 (1966).

[59] K. Watanabe, T. Taniguchi, and H. Kanda, *Direct-Bandgap Properties and Evidence for Ultraviolet Lasing of Hexagonal Boron Nitride Single Crystal*, Nat. Mat. **3**, 404 (2004).

[60] M. P. Seah and W. A. Dench, *Quantitative Electron Spectroscopy of Surfaces: A Standard Data Base for Electron Inelastic Mean Free Paths in Solids*, Surf. Interface Anal. **1**, 181 (1979).

[61] A. B. Preobrajenski, A. S. Vinogradov, and N. Martensson, *Monolayer of h-BN Chemisorbed on Cu(111) and Ni(111): The Role of the Transition Metal 3d States*, Surf. Sci. **582**, 21 (2005).

[62] P. J. Fazen, E. E. Remsen, J. S. Beck, P. J. Carroll, A. R. McGhie, and L. G. Sneddon, *Synthesis, Properties, and Ceramic Conversion Reactions of Polyborazylene. A High-Yield Polymeric Precursor to Boron Nitride*, Chem. Mater. **7**, 1942 (1995).

[63] P. Sutter, J. Lahiri, P. Zahl, B. Wang, and E. Sutter, *Scalable Synthesis of Uniform Few-Layer Hexagonal Boron Nitride Dielectric Films*, Nano Lett. **13**, 276 (2013).

[64] M. Henzler and W. Göpel, *Teilchentransport im Ultrahochvakuum (UHV)*, B. G. Teubner Stuttgart, 1994.

[65] P. W. Atkins, *Transporteigenschaften eines idealen Gases*, chapter 24.1.4, Oxford University Press, 1996.

[66] J. H. Lienhard IV and J. H. Lienhard V, *Thermal Radiation Heat Transfer*, chapter IV, Phlogisten Press Cambridge Massachusetts, 2002.

[67] J. H. Lienhard IV and J. H. Lienhard V, *The General Problem of Heat Exchange*, chapter I, Phlogisten Press Cambridge Massachusetts, 2002.

[68] K. S. Novoselov, A. K. Geim, S. V. Morozov, D. Jiang, Y. Zhang, S. V. Dubonos, I. V. Grigorieva, and A. A. Firsov, *Electric Field Effect in Atomically Thin Carbon Films*, Science **306**, 666 (2004).

[69] G. Eda, H. Yamaguchi, D. Voiry, T. Fujita, M. Chen, and M. Chhowalla, *Photoluminescence from Chemically Exfoliated MoS_2*, Nano Lett. **11**, 5111 (2011).

[70] R. Rüttimann, *Towards Freestanding Hexagonal Boron Nitride: Delamination by Etching and Bubbling*, Bachelor thesis at University of Zurich (2014).

[71] E. Koren, E. Sutter, S. Bliznakov, F. Ivars-Barcelo, and P. Sutter, *Isolation of High Quality Graphene from Ru by Solution Phase Intercalation*, Appl. Phys. Lett. **103**, 121602 (2013).

[72] T. Brugger, H. Ma, M. Iannuzzi, S. Berner, A. Winkler, J. Hutter, J. Osterwalder, and T. Greber, *Nanotexture Switching of Single-Layer Hexagonal Boron Nitride on Rhodium by Intercalation of Hydrogen Atoms*, Angew. Chem. Int. Ed. **49**, 6120 (2010).

[73] A. J. Bard and L. R. Faulkner, *Electrochemical Cells and Cell Resistance*, chapter 1.3.4, John Wiley & Sons, Inc., 2001.

[74] A. J. Bard and L. R. Faulkner, *Effects of Solution Resistance*, chapter 15.6.1, John Wiley & Sons, Inc., 2001.

[75] A. J. Bard and L. R. Faulkner, *Effects of Solution Resistance*, chapter 1.2, John Wiley & Sons, Inc., 2001.

[76] Y. Wang, Y. Zheng, X. Xu, E. Dubuisson, Q. Bao, J. Lu, and K. P. Loh, *Electrochemical Delamination of CVD-Grown Graphene Film: Toward the Recyclable Use of Copper Catalyst*, ACS Nano **5**, 9927 (2011).

[77] L. Gao, W. Ren, H. Xu, Z. Wand, T. Ma, L. P. Ma, Z. Zhan, Q. Fu, L. M. Peng, X. Bao, and H. M. Cheng, *Repeated Growth and Bubbling Transfer of Graphene with Millimetre-Size Single-Crystal Grains Using Platinum*, Nat. Commun. **3**, 699 (2012).

[78] C. J. L. de la Rosa, J. Sun, N. Lindvall, M. T. Cole, Y. Nam, M. Löffler, E. Olsson, K. B. K. Teo, and A. Yurgens, *Frame Assisted H2O Electrolysis Induced H2 Bubbling Transfer of Large Area Graphene Grown by Chemical Vapor Deposition on Cu*, Appl. Phys. Lett. **102**, 022101 (2013).

[79] J. F. Moulder, W. F. Stickle, P. E. Sobol, and K. D. Bomben, *Teilchentransport im Ultrahochvakuum (UHV)*, Perkin-Elmer Corporation, Physical Electronics Division, 1992.

[80] C. A. Howsare, X. Weng, V. Bojan, D. Snyder, and J. A. Robinson, *Substrate Considerations for Graphene Synthesis on Thin Copper Films*, Nanotechnology **23**, 135601 (2012).

[81] P. Zeller, S. Dänhardt, S. Gsell, M. Schreck, and J. Wintterlin, *Scalable Synthesis of Graphene on Single Crystal Ir(111) Films*, Surf. Sci. **606**, 1475 (2012).

Acknowledgments

This work would not have been possible without the many people helping me along the way with inputs, assistance and support.
First of all I would like to thank Thomas Greber and Jürg Osterwalder, who gave me the opportunity to accomplish this thesis and who trusted in me to bring the Sinergia laboratory into an operational status. I could not only learn to solve technical problems, organizational issues or physics, but also gain insight into science and the academic life.
I also want to thank Frank Nüesch for his efforts to supervise this thesis and to judge it as an external expert. I also appreciated the opportunity to assemble an organic light emitting diode on our *h*-BN nanomesh substrate at EMPA.
I would like to thank Huanyao Cun for her important contributions to all of my publications and this thesis. Among these, I would like to mention STM images for the Sinergia publication and UV tape tests and wafer cutting and typesetting. Furthermore, thank you for letting me finalizing the UV flash lamp setup, which is an important part within this thesis.
A special thank goes to all those people, who were willing to answer and help satisfying my curiosity especially at the beginning of the thesis, as I was new in the UHV business. It was Martin Klöckner, who suddenly had to remember or look up technical details, which he learned a decade ago. Thank you very much, you formed the basis of my knowledge. A special thank also goes to Martin Morscher, who knew how to solve any problem and where to find or order anything. Within the same line, I have to acknowledge the contributions of Dominik Leuenberger, who patiently listened to my problems and confirmed their importance, but also helped identifying the LabView bugs of the Sinergia heater controller. I also highly value the many inputs and hardware contributions of Matthias Hengsberger, who had been a constant point of inspiration at the coffee breaks.
A special thank goes to Manuel Graf, who did the ion source implementation into the Sinergia chamber. His curiosity vividly showed me each day, that there are still young people who are interested in what they are doing and in doing it right.
I want to thank Stijn Mertens for his efforts in continuing of electrochemical investigations and in sharing beamtime at the Swiss Light Source.
I would also like to thank Carlo Bernard, who did program the movement of the x-y stage for the Sinergia publication. I very much admire your way of keeping focused upon a single project and never loosing your goal out of sight.
I also thank Roland Hany and Jean-Nicolas Tisserant from the Laboratory for Functional Polymers at EMPA Dübendorf, who realized the first functional organic light diode with an *h*-BN nanomesh bottom electrode.
I would also like to thank the cophee-team with Hugo Dil, who substantially contributed in the pyrometer acquisition process, and his co-workers Stefan Muff, Bartosz Slomski and Gabriel Landolt.
I would also like to thank all the coffee break people for listening and making fun out of my

constant complaints, mainly Silvan Roth, Gerson Mette and Luca Castiglioni.
I am also grateful to the present colleagues of the surface physics group for discussions and the good time, which are Rasmus Westerstöm, Michael Greif, Adrian Schuler, Elisa Miniussi, Aram Kostanyan, Roland Stania and Rubina Arulanantham.
Furthermore, I would like to thank many people within the physics institute. Many thanks to the work shop team, especially Kurt Bösiger, Reto Maier, Bruno Lussi, Marcel Schaffner and Silvio Scherr. Without their efforts and inputs, the Sinergia chamber would not be working and be much more expensive. I also thank the secretariat Carmelina Genovese, Monika Röllin and Ruth Halter for their administrative support and the refreshing chats. I also appreciate the constant and competent support from the electronics work shop, especially Achim Vollhardt and Daniel Florin. Last but not least, I need to thank Roland Bernet for the IT support.

Publications

1. H.Y. Cun, M. Iannuzzi, **A. Hemmi**, J. Osterwalder, and T. Greber, *"Two-Nanometer Voids in Single-Layer Hexagonal Boron Nitride: Formation via the "Can-Opener" Effect and Annihilation by Self-Healing"*, ACS Nano 8 (7), 7423 (2014)

2. **A. Hemmi**, C. Bernard, H.Y. Cun, S. Roth, M. Klöckner, T. Kälin, M. Weinl, S. Gsell, M. Schreck, J. Osterwalder, and T. Greber, *"High Quality Single Atomic Layer Deposition of Hexagonal Boron Nitride on Single Crystalline Rh(111) Four-Inch Wafers"*, Rev. Sci. Instr. 85, 035101 (2014)

3. **A. Hemmi**, H. Cun, S. Roth, J. Osterwalder, and T. Greber, *"Low Cost Photoelectron Yield Setup for Surface Process Monitoring"*, J. Vac. Sci. Technol. A 32, 02302, (2014)

4. H.Y. Cun, M. Iannuzzi, **A. Hemmi**, J. Osterwalder, and T. Greber, *"Implantation Length and Thermal Stability of Interstitial Ar Atoms in Boron Nitride Nanotents"*, ACS Nano, 8, 1014 (2014)

5. L.H. de Lima, H.Y. Cun, **A. Hemmi**, T. Kälin, and T. Greber, *"An Ion Source for Alkali Metal Implantation beneath Graphene and Hexagonal Boron Nitride Monolayers on Transition Metals"'*, Rev. Sci. Instr. 84, 126104 (2013)

6. H.Y. Cun, M. Iannuzzi, **A. Hemmi**, S. Roth, J. Osterwalder, and T. Greber, *" Immobilizing Individual Atoms beneath a Corrugated Single Layer of Boron Nitride"*, Nano Letters 13, 2098 (2013)

7. J. van Beek, **A. Hemmi**, M. Ernst, B.H. Meier, *"Second-Order Dipolar Order in Magic-Angle Spinning Nuclear Magnetic Resonance"*, J. Chem. Phys. 135, 154507 (2011)